

LIBRARY
Michigan State
University

This is to certify that the
dissertation entitled

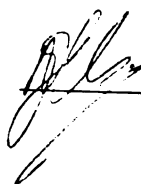
SELF-POWERED SENSING IN STRUCTURAL HEALTH AND
USAGE MONITORING

presented by


NIZAR LAJNEF

has been accepted towards fulfillment
of the requirements for the

Ph.D. degree in Civil Engineering

 (NIELL ELVIN)

Major Professor's Signature

 (Shantam
Chakraborty)

08/11/08

Date

PLACE IN RETURN BOX to remove this checkout from your record.
TO AVOID FINES return on or before date due.
MAY BE RECALLED with earlier due date if requested.

DATE DUE	DATE DUE	DATE DUE
"AUG 1 31 2014"		

SELF-POWERED SENSING IN STRUCTURAL HEALTH AND USAGE
MONITORING

By

Nizar Lajnef

A DISSERTATION

Submitted to
Michigan State University
in partial fulfillment of the requirements
for the degree of

DOCTOR OF PHILOSOPHY

Department of Civil and Environmental Engineering

2008

ABSTRACT

SELF-POWERED SENSING IN STRUCTURAL HEALTH AND USAGE MONITORING

By

Nizar Lajnef

Fatigue and overload of mechanical, civil and aerospace structures remains a major problem that can lead to costly repair and catastrophic failure. Long term monitoring of mechanical loading for these structures could reduce maintenance cost, improve longevity and enhance safety. However, the powering of these sensors throughout the lifetime of the monitored structure remains a major problem.

The ability to convert ambient energy into electric power would eliminate the problem of drained electrical supply, and would allow indefinite monitoring. This work first answers the key question: can sufficient electrical energy be produced from typical structural motions? Realistic earthquake, wind and traffic loads are used to calculate the theoretical maximum energy levels that can be extracted from these dynamic events. The same dynamic loads are used to calculate and experimentally measure the electrical energy produced by a realistic piezoelectric generator.

The collected energy levels are compared to the energy requirements of various electronic subsystems in a wireless sensor. For a 5 cm^3 sensor node (the volume of a typical concrete stone), it is found that only extreme events such as earthquakes can provide sufficient energy to power currently available wireless sensors. For most typical dynamic events, it would be impossible to harvest enough energy to power a 5 cm^3

wireless sensor. The results show that achieving continuous, self-powered, monitoring will require the development of a sensor node that can operate within a power budget of $1\mu\text{W}$.

The implementation of a novel self-powered fatigue monitoring sensor is presented. The sensor is based on the integration of piezoelectric transduction with floating gate avalanche injection. The miniaturized sensor enables self-powered, continuous monitoring and time-to-failure predictions of mechanical and civil structures. The sensor exploits a log-linear response of a current starved hot-electron injection process on a floating-gate transistor biased in the weak-inversion region. The measured response is shown to be minimally invariant to device mismatch and temperature fluctuations. By configuring an array of floating-gate transistors to respond to different amplitude levels of the input signal, the proposed circuit implements a level counting algorithm which is widely used in many usage monitoring techniques. Measured results from a fabricated integrated circuit in a $0.5\text{-}\mu\text{m}$ CMOS process demonstrate that the prototype can sense, store and compute over 10^7 loading cycles. The power dissipation of the prototype is measured to be 800nW which makes it ideal for autonomous long-term operation. The prototype is interfaced with different piezoelectric transducers and is tested in the laboratory to demonstrate its applicability for real-time usage monitoring.

Copyright by
NIZAR LAJNEF
2008

DEDICATION

To my parents, without whom this work could not have been completed

ACKNOWLEDGEMENTS

I would like to express my gratitude to Drs Niell Elvin and Shantanu Chakrabartty for their support, ideas and guidance throughout my stay at Michigan State University. Their vision and expertise guided me in the development of this research. I also would like to extend my appreciations to Dr. Ronald Harichandran and Dr Rigoberto burgeneo for reading this dissertation and offering constructive comments.

Thanks to Dr Karim Chatti for his friendship and valuable advices. He always gave me back my confidence whenever I lost it. Thanks to my parents, my wife and my family for their continuous emotional support.

I am indebted to Amit Gore for the innumerable discussions that we had together, and for his support in the testing of the analog floating gates. Finally, many thanks to my fellow graduate students at the AIM lab and the Civil Engineering Department.

The research in this dissertation has been supported by the NSF grant CMMI 0700632.

TABLE OF CONTENTS

LIST OF TABLES	ix
LIST OF FIGURES	x
CHAPTER 1	
INTRODUCTION	1
1.1 Motivation.....	1
1.2 Background.....	3
1.2.1 Fatigue And Fatigue Prediction	3
1.2.2 Smart Sensors For Structural Monitoring	8
1.3 Objectives And Overview.....	11
CHAPTER 2	
PIEZOELECTRIC ENERGY HARVESTING	14
2.1 Introduction.....	14
2.2 Piezoelectric Basics	14
2.3 Piezoelectric Modeling	17
2.3.1 Strain Energy Harvesting.....	17
2.3.2 Vibration Energy Harvesting.....	20
2.3.2.1 Background.....	20
2.3.2.2 Simplified Mechanical And Equivalent Electrical Models	23
2.3.2.3 Experimental Validation Of Models.....	24
2.4 Conclusion	34
CHAPTER 3	
FEASIBILITY OF STRUCTURAL MONITORING WITH VIBRATION POWERED SENSORS.....	35
3.1 Introduction.....	35
3.2 Electronics And Subsystem Power Consumption.....	38
3.3 Practical Considerations.....	39
3.4 Vibration Energy Harvesting In Typical Civil Environments	40
3.4.1 Harvestable Power	43
3.4.2 Maximum Theoretical Harvestable Power	46
3.4.3 Piezoelectric Energy Conversion Efficiency	48
3.5 Energy Harvesting In High Vibration Civil Environments	52
3.5.1 Optimal Energy Harvesting	54
3.5.2 Example	55
3.5.3 Optimal Energy Harvesting Results.....	56
3.6 Discussion.....	59
3.7 Conclusion	64

CHAPTER 4	
SUB-MICROWATT PIEZO-POWERED ANALOG CIRCUITS: MODELING AND ANALYSIS	66
4.1 Introduction.....	66
4.2 Floating Gate Transistors	67
4.3 Floating-Gate Injector And Its Mathematical Model.....	72
4.4 Cmos Current References	76
4.5 Design Of A Complete Floating-Gate Sensor Array	80
4.6 Conclusion	84
CHAPTER 5	
RESULTS AND DISCUSSION	85
5.1 Introduction.....	85
5.2 System Robustness.....	87
5.3 Experimental Measurements	89
5.3.1 Initialization Of The Injectors Array	89
5.3.2 Threshold Adjustment And Levels Detection.....	91
5.3.3 Level-Crossing Counter	95
5.3.4 Counting Resolution	102
5.3.5 Power Dissipation	102
5.4 Design Examples For Systems Monitoring – Sensor And Transducer Interfacing.....	104
5.5 Discussion.....	110
5.6 Conclusion	111
CHAPTER 6	
CONCLUSIONS AND RECOMMENDATIONS	113
APPENDIX	
MICROGRAPHS AND LAYOUT DETAILS	118
BIBLIOGRAPHY	126

LIST OF TABLES

Table 1.1 Cycle counting methods [19, 20, 21, 22]	7
Table 2.1 Comparison of material properties of two commonly used piezoelectric materials	17
Table 2.2 Generator parameters assuming an Euler-Bernouli cantilever bimorph. The displacement shape function is assumed to be, $w = u(t)[1 - \cos(\pi x / (2L))]$ where x is the horizontal distance from the support. The electrical potential shape function is given by $\psi = zv / h$, where z is the vertical distance from the beam center, i.e. the beam's displaced shape. E is the modulus of elasticity of the beam, e_{31} is the piezoelectric coupling coefficient, ϵ is the electric permittivity, $I = bh^3 / 12$ is the second moment of area and \bar{m} is the mass per unit length.	23
Table 2.3 Piezoelectric sensor properties.....	30
Table 3.1 Comparison of energy scavenging sources [52]	37
Table 3.2 Approximate energy consumption in a wireless sensor node (references in brackets). Volatile memory (VM) is assumed to be replaced by low-power non-volatile memory (NVM) [56].....	39
Table 3.3 Piezoelectric and circuit sensor properties.....	58
Table 4.1 Component sizes used in circuit in Figure 4.10.....	81
Table 5.1 Summary of measured specifications	86

LIST OF FIGURES

Figure 1.1 Example of an S-N curve (redrawn with parameters adapted from [18])	5
Figure 2.1 Schematic depiction of a piezoelectric material pulled by a force F . The material undergoes an axial strain S	17
Figure 2.2 (a) Schematic of a piezoelectric scavenger of length L , width b and height h ; (b) Equivalent circuit diagram (the dashed block) for a piezoelectric material under slow dynamic loading	19
Figure 2.3 Theoretical energy harvester with an equivalent electric damper	21
Figure 2.4 Schematic of a piezoelectric vibration scavenger of mass (M), length (L), width (b) and height (h). The equivalent mechanical single degree of freedom system is also shown	21
Figure 2.5 The equivalent circuit for a single degree of freedom piezo-generator. The mechanical force input is simulated as a voltage generator element with magnitude $M\ddot{u}_g$	24
Figure 2.6 Method of experimentally measuring piezoelectric generator parameters. The vibrator is driven over a range of frequencies to obtain the open-circuit voltages. The accelerometer is used to measure the base excitation \ddot{u}_g directly	25
Figure 2.7 Open-circuit piezoelectric voltage transfer function (the least square fitted model is shown as a solid line, and the experimental results are shown as dots). The non-linear least square fitted parameters are $K=985\text{N/m}$, $\Theta=6\times 10^{-4}\text{C/m}$, and $\zeta=1.3\%$. The measured parameters are $M_{tip}=9.4\text{g}$ and $C=25.2\text{nF}$. The coefficient of correlation is $r=0.98$	26
Figure 2.8 A full diode bridge piezoelectric circuit for storing electrical charge on a capacitor (C_s), the circuit leakage is represented by the resistor (R_d)	27
Figure 2.9 (a) Measured and calculated voltages for the piezoelectric unimorph with properties calculated from Figure 2.7. The input accelerations are compared at 5 seconds after the linear stroke motor is switched on. The circuits elements properties are: storage capacitor $C_s = 3.3\mu\text{F}$; drain resistance $R_d = 10\text{M}\Omega$, and diodes 1N4148. The line represents equal measured and calculated voltages, the coefficient of correlation, assuming the simulated voltage is equal to the measured voltage is $r=0.97$; (b) a simulated (solid) and experimental (dashed) voltage time history on the storage capacitor	28
Figure 2.10 Schematic representation of a PVDF vibration energy scavenger	31

Figure 2.11 Experimental setup to test the piezoelectric bimorph generator	31
Figure 2.12 Experimental (dots) and theoretical (line) acceleration–voltage transfer function for piezoelectric energy harvester.....	32
Figure 2.13 Theoretical and experimental results for the piezoelectric energy generator subjected to the El Centro earthquake (only 6 s is shown for clarity)	33
Figure 3.1 Schematic of a piezoelectric vibration scavenger	39
Figure 3.2 (a) Time-history and (b) frequency spectrum for the acceleration measurements from the deck of a concrete bridge under traffic loading [67]	41
Figure 3.3 (a) Ground acceleration time-history and (b) frequency spectrum from the El Centro earthquake (North–South direction).....	42
Figure 3.4 Theoretical average power output for various electric damping ratios. The mechanical damping is assumed to be 5%.....	44
Figure 3.5 (a) Maximum power and (b) bandwidth for various electrical and damping ratios.....	45
Figure 3.6 Maximum theoretical vibration energy for various structures and loading conditions.....	48
Figure 3.7 Electric energy output from a piezoelectric bimorph for various dynamic excitations	51
Figure 3.8 Approximate serviceability structural vibration limits (based on [74], [75] and [76]). The shaded region represents the limits based on various exposure times. The lower boundary represents longer duration vibrations; the upper boundary represents shorter duration vibrations. The solid line at 1.5m/s^2 represents extreme vibration conditions.....	53
Figure 3.9 Investigated structure consisting of a steel I-beam with an overhead moving crane. Position of accelerometer node is as shown.....	55
Figure 3.10 A typical input acceleration time history and the associated frequency spectrum for a lightweight crane moving at 0.8m/s , measured at mid-span on the supporting beam.....	57
Figure 3.11 Maximum extractable electrical energy for a resistive circuit (solid lines) and diode-bridge circuit (circles), for the crane moving from left to right at 0.8m/s . The three solid lines represent acceleration histories from three different crane runs.....	58

Figure 3.12 Generated electrical energy from the El Centro earthquake for a bimorph PZT with various resonant frequencies.....	61
Figure 3.13 Generated electrical energy for various traffic loadings on a concrete bridge, assuming perfect electro-mechanical conversion	62
Figure 4.1 Principle of the piezo-powered floating-gate sensor	67
Figure 4.2 (a) Top and cross-sectional view of a floating-gate transistor and (b) the measured drain current when injection pulses of different amplitude are repeatedly applied across the drain-source terminal.....	69
Figure 4.3 Capacitive model of a pMOS floating-gate transistor.....	71
Figure 4.4 Simplified circuit model for piezo-driven floating-gate sensor [83].....	73
Figure 4.5 Response of a floating-gate injector based on the mathematical model in Equation 4.10	75
Figure 4.6 Response of the floating-gate injector for different values of (a) parameter K2 and (b) parameter K1	77
Figure 4.7 Schematic of a CMOS current reference.....	78
Figure 4.8 Floating-gate reference array.....	82
Figure 4.9 Simulation result using the circuit in Figure 4.8, showing the current through the floating gate cells for different peak excitation input voltage	83
Figure 5.1 Micrograph of the prototype floating-gate sensor.....	86
Figure 5.2 Voltage responses measured at various source currents.....	88
Figure 5.3 Voltage responses measured for various chips in the same run	88
Figure 5.4 Voltage responses measured for various temperatures	89
Figure 5.5 Flow-chart describing the sensor initialization algorithm.....	90
Figure 5.6 Measured output voltages (O1–O4) response vs. input voltage.....	93
Figure 5.7 Measured source-to-drain voltage response across floating-gate elements at $V_{dd}=5.3V$	93
Figure 5.8 Measured source-to-drain voltage response across floating-gate elements at $V_{dd}=6.1V$	94

Figure 5.9 Measured source-to-drain voltage response across floating-gate elements at $V_{dd}=6.9V$	94
Figure 5.10 Measured output voltage response for the sensor array when subjected to a loading cycle represented by a piezoelectric output with injection duration 3:2:1	97
Figure 5.11 Measured output voltage response for the sensor array when subjected to a loading cycle represented by a piezoelectric output with injection duration 3:2.5:1	98
Figure 5.12 Measured output voltage response for the sensor array when subjected to a loading cycle represented by a piezoelectric output with injection duration 3:2:0.5	99
Figure 5.13 Measured output voltage response using the sensor array in which the first 1000 cycles have been used as calibration intervals and the subsequent three level loading cycles with the duration of injection are in the ratio 3:2:1	100
Figure 5.14 Measured output voltage response using the sensor array in which the first 1000 cycles have been used as calibration intervals and the subsequent three level loading cycles with the duration of injection are in the ratio 3:2.5:1	101
Figure 5.15 Measured results to calculate the resolution for event counting: (a) Change in source voltage measured for different relative counts of voltage pulses for over 100,000 events; (b) Inset showing zoomed area between 10,000 to 40,000 events	103
Figure 5.16 Supply current drawn by the sensor at different supply voltages.....	104
Figure 5.17 (a) Voltage generated by a piezoelectric transducer in response to periodic loading; (b) Measured response of the floating-gate injector array	106
Figure 5.18 Setup environment for MTS machine	108
Figure 5.19 Voltage responses measured when the prototype is interfaced with a PVDF transducer and subjected to controlled cyclic strain levels with magnitude $2107\mu\epsilon$	108
Figure 5.20 Voltage responses measured when the prototype is interfaced with a PVDF transducer and subjected to controlled cyclic strain levels with magnitude $2546\mu\epsilon$	109

Figure 5.21 Voltage responses measured when the prototype is interfaced with a PVDF transducer and subjected to controlled cyclic strain levels with magnitude $2809\mu\epsilon$	109
Figure 5.22 Slope deviation observed for injection currents less than 1 electron per second	110
Figure 6.1 System architecture of a complete implanted device that integrates the proposed floating-gate sensor array	116
Figure A.1 Micrographs of different prototypes	120
Figure A.2 Layout of the prototype tested in Chapter 5	121
Figure A.3 Layout of the current reference	122
Figure A.4 Layout of the diodes array	123
Figure A.5 Layout of the floating-gate injectors array	124
Figure A.6 Layout of a single floating-gate injector.....	125

CHAPTER 1

INTRODUCTION

1.1 MOTIVATION

Innovative sensors and sensor systems represent one of the foundations of smart structures technology development. The design, fabrication, and implementation of these systems are one of the ultimate challenges to engineering researchers today. Structural monitoring is a primary application for new sensor technologies. Indeed, much attention has been focused in recent years on the declining state of the aging civil infrastructure in the United States. These concerns apply not only to civil engineering structures, but also to other types of mechanical systems, such as aircrafts, rotating machines and biomechanical implants. A critical parameter is the prediction of the remaining life of structural components which is an ongoing research and commercial enterprise that can lead to substantial cost savings. For example, the US Air Force estimates that there will be a cost saving of nearly \$1 billion for the next 15 years for the rotor of the F100 aircraft, due to the procedures that were first implemented in 1986 to detect and predict fatigue damage [1].

However, in many cases the current techniques that have been developed for the evaluation of structural components remain expensive, unreliable or impractical. For example, currently there is no completely reliable means of monitoring sub-surface damage in civil infrastructure, though many expensive techniques such as thermography [2] and ground penetrating radar [3] are currently being developed with various degrees

of success [4]. In many structures the cost-savings of fatigue monitoring cannot be realized since these advanced fatigue life prediction strategies require damage detection through regular non-destructive inspection and relatively sophisticated fatigue life prediction algorithms [5]. This makes these techniques too expensive (or unreliable) for many low-cost (or single unit) structures such as commonly found in civil infrastructure for example (railways, pavements and bridges).

It is largely due to the cost and maintenance time needed for classical non-destructive imaging techniques that the field of Structural Health Monitoring is currently being investigated [6, 7, 8]. The use of embedded sensors, offers several benefits over non-destructive imaging techniques. These include the ability for continuous monitoring without the disruption of use of the structure for inspection. Though structural monitoring is attractive for these reasons, several issues still hamper their wide acceptance. The first disadvantage of wireless embedded sensors is their relative expense. Even at \$100 per sensor node [9] (probably an unrealistically low number), instrumenting an entire structure with many sensors might be prohibitively expensive for many applications. Secondly, the useful life of the sensor nodes is dependent on the battery power [9]. However with current battery operation it is unlikely that the wireless sensor nodes would last more than several years before being replaced (The best shelf-life of batteries is on the order of 5 to 10 years). The expense of periodically replacing batteries, especially for sensors embedded within the structure, remains a major problem for the wide acceptance of wireless-sensor networks. (Other problems such as network size are also a major concern [10, 11]).

Another possibility of structural monitoring is the so called ‘Health and Usage Monitoring System’ (HUMS). This system senses and stores the mechanical usage of a structural component [12, 13, 14]. Though often inaccurate in predicting remaining life, it is still an important tool in the aircraft industry for scheduling further inspection and maintenance. However, current HUMS systems are expensive, bulky and also require a continuous source of power.

This work verifies and tests the hypotheses that a low-cost, self-powered usage monitoring sensor, that can compute and store cumulative history of strain experienced by the structure, can be achieved by combining piezoelectric transduction and low power analog signal processing circuits. The developed system would serve as an important intermediate solution for fatigue life monitoring of many structures.

1.2 BACKGROUND

1.2.1 Fatigue and fatigue prediction

The term fatigue was first introduced by Poncelet [15] in 1839. In the early twentieth century, due to the increasing use of ferrous structure especially in railway systems, significant work has been done to understand and model this phenomenon. Although these models can predict, to some extent the experimental results, they remain inaccurate for certain real applications. For example these models cannot take into account environmental conditions and material imperfections.

Mechanical fatigue is formally defined as the accumulation of damage in a structure under applied fluctuating stresses. Even though the magnitudes of the applied stresses could be less than the tensile strength of the material, the progressive fatigue damage may

ultimately lead to complete mechanical failure. The fatigue life is defined as the number of constant amplitude load cycles necessary to induce fatigue failure in an initially undamaged specimen. Several approaches can be used to characterize fatigue life, such as the energy-based approach and the stress or strain life approach.

A simple energy based prediction of fatigue life can be expressed as follow:

$$N_f = \frac{Q}{q} \quad (1.1)$$

where Q is the total mechanical work absorbed in the material, q is the cyclic energy and N_f is the number of cycle to failure. This criterion is based on the assumptions that q is approximately constant during the fatigue life and Q is constant for the imposed external conditions. Q might be also regarded as the maximum amount of mechanical work the material could absorb untill failure.

For a stress/strain based approach, the fatigue life is typically expressed using S-N curves. An example of an S-N curve is shown in Figure 1.1. Higher load levels require fewer cycles to cause structural failure whereas low load levels require many more cycles to cause failure.

Mathematically, the S-N curve can be modeled by the following equation [16]:

$$\sigma_a = \sigma_f^f (2N_f)^b \quad (1.2)$$

where σ_f^f is the fatigue strength coefficient, and b is the fatigue strength exponent (or the Basquin exponent) that are determined experimentally [16].

In its strain-life form, the S-N curve can be characterized based on the plastic strain amplitude using the Coffin-Manson relation [17] given by:

$$\frac{\Delta \varepsilon_p}{2} = \varepsilon_f^f (2N_f)^c \quad (1.3)$$

where $\Delta \varepsilon_p/2$ is the plastic strain amplitude, ε_f^f is the fatigue ductility coefficient and c is the fatigue ductility exponent. Using (1.2), the total strain amplitude can then be related to the fatigue life as follow:

$$\frac{\Delta \varepsilon}{2} = \varepsilon_f^f (2N_f)^c + \frac{\sigma_f^f}{E} (2N_f)^b \quad (1.4)$$

Where E is the young's modulus.

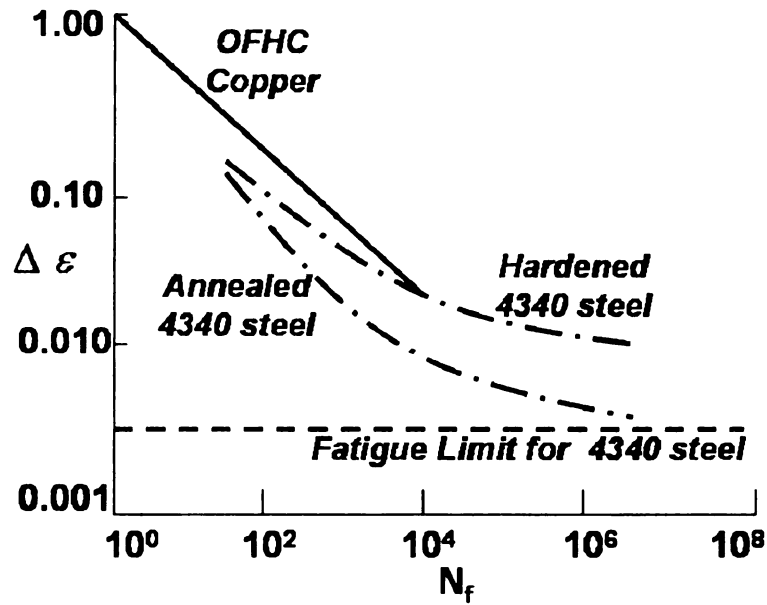


Figure 1.1 Example of an S-N curve (redrawn with parameters adapted from [18])

An important consequence of the S-N curve is that loading cycles less than the so-called fatigue limit (Figure 1.1) should not cause the material to fail (often taken as a stress level that can withstand 10^7 cycles). In the context of fatigue monitoring, it is

therefore unimportant to measure strains less than the fatigue limit of the material since they do not contribute to overall damage of the material. The monitoring system (sensor) could therefore ignore input signals below a level that would be calibrated to match the fatigue limit of the inspected structure. For many construction steels, the fatigue strain limit is greater than $1500\mu\epsilon$ [18].

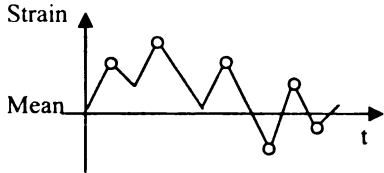
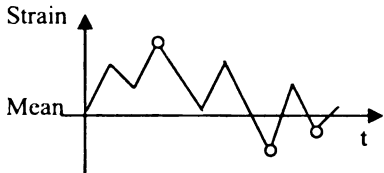
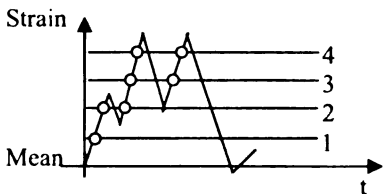
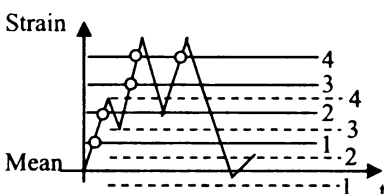
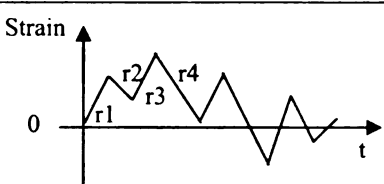
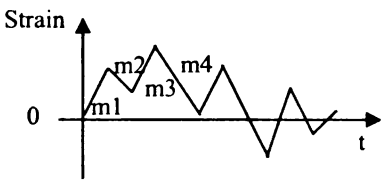
However, the S-N curve can not be directly used to determine fatigue in real-world conditions, since the magnitude of the applied cyclic loads vary depending on the environmental conditions. Several algorithms have therefore been devised for fatigue life-time predictions under non-periodic loading conditions. The most common and widely used algorithm is the Palmgren-Miner's Rule [16] often simply called the Miner's rule. In its basic form, the Miner's rule assumes that each strain cycle with magnitude i uses $1/N_i$ of the total fatigue life, where N_i is the number of fatigue cycles taken to fail the material at a strain level of i . Algebraically this can be stated as:

$$\sum \frac{n_i}{N_i} = 1 \quad (1.5)$$

The Miner's rule algorithm is by no means perfect (because of its omission of load sequence effects) and was not developed for all possible loading conditions. However it is still routinely used in practice to estimate the fatigue life for structural components.

A pre-processing step is required before Miner's rule can be applied to calculate statistics of arbitrary loading cycles. This typically involves counting methods which reduces a spectrum of varying stress-strain measurements into a set of simple stress-strain reversals. The objective is to identify the range and mean values of the loading events, within the random spectrum, which contribute to the specimen fatigue so that the proper amount of damage due to each event can be accounted for. Table 1.1 presents an illustrat-

Table 1.1 Cycle counting methods [19, 20, 21, 22]

Name	Illustration	Description
Peak		All maximums above the mean and all minimums below the mean are counted
Mean crossing peak		Only the largest peak between successive crossing of the mean is counted
Level crossing		All positive slope level crossing above the mean, and negative slope level crossing below the mean are counted
Fatigue meter		Similar to level crossing except that only one count is made between successive crossing of a lower level associated with each counting level
Range		Each range (the difference between successive peak values) is counted as 1/2 cycle, the amplitude of which is half the range
Range - mean		Ranges are counted as above and the mean value of each range is also considered

ion and a small description of six commonly used empirical cycle counting methods. In this thesis, the level-crossing method is selected. The algorithm counts the total number of occurrences when the magnitude of strain exceeds a pre-defined threshold. The thresholds are typically quantized strain levels as shown in Table 1.1 which also shows the threshold crossing events (denoted by circles). The total count of events denoted by n_i is then normalized by N_i (from the S-N curve) according to the Miner's rule (Equation (1.5)).

1.2.2 Smart sensors for structural monitoring

A smart sensor differs from a standard sensing unit mainly by its on-board intelligence capabilities (on-board computations). Three important features typically characterize a smart sensor: an on-board processing unit, wireless capability, and networking capability.

Some of the first efforts in developing a smart sensor for civil engineering applications were presented in [23, 24, 25]. Two types of monitoring systems were identified: extreme event, and long-term monitoring systems. The designed hardware consisted mainly of a microprocessor, radio modem, data storage, and batteries. Data analysis programs were developed to analyze the acquired data and facilitate damage detection diagnosis. While the developed systems provided ease of installation and portability, several problems were identified such as synchronization of communications signals between nodes and data collection system, battery durability/longevity, and significant variations of the host structure characteristics due to environmental changes such as loading, boundary conditions, temperature, and humidity.

Several research groups [7, 11, 26, 27, 28, 29] have focused on solving the wireless communication problems. In [26], a bridge monitoring system, consisting of a battery operated sensing interface and a small radio transponder, was investigated. The complete system consisted of a data collection system and a network of transducers distributed throughout the structure. The micro-sensors monitoring systems developed in [27] use a multiplexer to allow data from multiple transducers to be communicated over a single communication channel. Data is transmitted at the rate of 50Kbps over a range of approximately 0.25 miles. Damage is detected via variations in the natural frequencies of the structure.

The battery life of these sensors remained a major issue. For example, the prototype presented in [28] operates only for 15 hours continuously on two 9V batteries. In order to conserve power the sensors are put in an ultra low-power sleep mode, only communicating when a significant loading event occurs or at predefined fixed time intervals.

The devices presented in [7, 25] used mixed-mode analog and digital on-board electronics, and were characterized by a number of important attributes such as bi-directional communication, on board local processing, pre-programmed user defined algorithms, and onboard storage memory. The prototype wireless sensor in [7] used standard integrated circuit component (8-bit Motorola 68HC11E1 microcontroller, ADXL210 accelerometer). The whole system was accommodated within a sealed package with an approximate size of 5" by 4" by 1" and was validated through controlled experiments in the laboratory

Driven by the desire to solve the powering issue, energy harvesting has been a topic given great attention in recent years [30, 31, 32, 33, 34, 35]. A number of potential self-powering energy sources have been identified, (e.g, solar power, thermal gradient, piezoelectric, vibrational), yet few are capable of providing the $\sim 100\mu\text{W}$ of continuous power widely believed to be the minimum required to operate a single sensor ([36], PicoRadio Project UC Berkeley). The quantity of energy that can be converted is directly related to the volume of the energy-converter. However in many civil engineering structures, the sensor unit would be embedded into the structure (such as in concrete or asphalt). A volume greater than 5 cm^3 could lead to significant weakening of the structure. In this thesis, all presented results are for a limited sensor size of 5 cm^3 , which is the typical size of concrete aggregate [37].

Several research groups [36, 38, 39] are currently working on decreasing the power-requirement for wireless motes, but even these low-power wireless sensor network nodes would require a minimum energy level of $100\text{ }\mu\text{W}$. In order to decrease sensor-power, on-board memory storage is an attractive alternative [40]. It should be also noted that in the context of civil and mechanical system fatigue monitoring, it is important to be able to capture each loading cycling. Many civil engineering structures are only subjected to significant loading cycles infrequently. During the times between significant loading cycles, it is possible that the sensor would experience periods of brown-outs and black-outs since any on-board battery or ultra-capacitor might lose the charge between these intermittent loading cycles. This further explains the need for using non-volatile memory storage, i.e, volatile memory storage would be lost during power-black outs. Current non-

volatile memory storage (for example floating gate transistors found in FLASH) requires 3 μ J to write 1 byte [University of Berkeley Mote measurement].

Previous research in [41, 42] has shown that it is possible to self-power some basic electronic switching and RF circuits using a 28 μ m x 4cm² PVDF piezoelectric material under a single trapezoidal pulse of applied strain (approximately 1500 $\mu\epsilon$ in magnitude and 0.5 seconds in duration). The estimated total energy generated by the loading is approximately 3 nJ. It should be noted that this corresponds to an average operational power-levels of 3 nW! The piezoelectric generated voltage is approximately 15 V.

1.3 OBJECTIVES AND OVERVIEW

The main objective of this work is to design and develop a novel structural fatigue monitoring sensor based on the integration of a piezoelectric transducer with ultra-low power computational analog circuits. The miniaturized sensor will enable continuous battery-less monitoring of engineering structures (for example civil, mechanical, and biomechanical). This will facilitate efficient maintenance and repair schedules by localizing possible failure points in a structure. The novel features of the sensor are:

- **Self-powered, continuous and autonomous sensing.** The proposed sensor will use novel analog signal processing circuits that will require less than 1 μ W of power (to our knowledge this is two orders of magnitude less power than previously demonstrated self-powered sensors [39]). The operational energy will be harvested directly from the sensing signal that is generated by a piezoelectric transducer.

- **Autonomous computation and non-volatile storage of sensing variables.** The sensor will use floating gate transistor injection principles [43] for computing cumulative mechanical strain patterns experienced by a structure. The method will obviate the use of data converters and digital computational circuitry, thus reducing the power requirement of the sensor.

Even though all the subcomponents of the sensor will be integrated, the scope of this thesis work will not include fatigue tests and challenges involved in packaging of the microelectronic components. The aim is to demonstrate practical applications of the sensor to autonomous sensing by validating and benchmarking its performance in realistic laboratory simulated structural monitoring scenarios. The specific objectives are:

- Objective 1: Piezoelectric characterization with respect to electrical power generation.
- Objective 2: Development of ultra-low power electronic sensing system which can sense, compute and store cumulative statistics of signals generated by the piezoelectric transducer.
- Objective 3: System integration, calibration and testing of a proof-of-concept prototype under laboratory conditions.

Chapter 2 presents simple mechanical and equivalent electrical models of the piezoelectric generator under different loading configurations. The presented models are validated using experimental results.

In chapter 3, the electrical energy that can be generated from typical civil structures such as bridges and buildings is evaluated under normal and extreme conditions. Results are obtained using models developed in chapter 2. It is shown that power converted from average dynamic events such as wind, traffic and low-scale earthquakes is approximately $1\ \mu\text{W}$, which is insufficient to run currently available sensors which require a minimum of $100\ \mu\text{W}$ of continuous power.

In chapter 4, the design and theoretical model of a novel self-powered event monitoring system based on a combination of piezoelectric transduction and floating gate injection are presented. Cadence based spice simulations of different components confirm the desired behavior of the proposed design.

Using a fabricated prototype, the design and models presented in chapter 4 are validated in chapter 5. A complete system, piezoelectric transducer and the fabricated prototype, is tested under realistic low-frequency, civil engineering loading in the laboratory. It is shown that the developed sensor can sense store and compute over 10^5 loading event cycles at a total power dissipation of less than $800\ \text{nW}$.

The work reported in this dissertation demonstrates the feasibility of a self-powered smart sensor for continuous monitoring of mechanical systems. This work provides an initial step toward the implementation and deployment of a low cost and reliable ‘smart’ networks for the long term monitoring of civil infrastructure.

CHAPTER 2

PIEZOELECTRIC ENERGY HARVESTING

2.1 INTRODUCTION

Currently, three major approaches are being investigated to convert mechanical energy to electrical energy for self-powering sensor electronics. These include: (1) electromagnetic, (2) electrostatic, and (3) piezoelectric harvesters. Though this chapter focuses only on piezoelectric power conversion, it should be noted that the other vibration self-powering approaches can be investigated with similar methods.

Piezoelectric energy harvesting, which is the ability of converting ambient mechanical loading into electrical energy, can potentially transform electronic sensing by providing a renewable and continuous energy source. Since a number of different approaches have been suggested for modeling piezoelectric energy harvesters ([35, 44, 45, 46]), a new researcher or designer in the field of piezoelectric energy harvesting might be overwhelmed by the number and complexity of the various models.

In this chapter, simple mechanical and equivalent electrical models that can be easily used for a general piezoelectric generator analysis are presented. The electrical models could be easily implemented into existing circuit simulation programs (such as SPICE) and provide reasonably accurate estimates of the generator performance under a wide variety of ambient loading environments.

2.2 PIEZOELECTRIC BASICS

The direct piezoelectric effect is the ability of certain crystalline materials to generate electric charge from an applied mechanical stress. Since most piezoelectric are

anisotropic, their physical constants (elasticity, permittivity etc.) are tensor quantities and relate to both the direction of the applied stress, electric field etc., and to the directions perpendicular to these. For this reason the constants are generally given two subscript indices which refer to the direction of the two related quantities (e.g. stress and strain for elasticity, displacement and electric field for permittivity). A superscript index is used to indicate a quantity that's kept constant. In the discussed examples in this work, stresses/stains are applied along the X-direction noted '1'. The direction of positive polarization is chosen to coincide with the Z-axis of a rectangular system and is noted '3'. The physical constants used in piezoelectric modeling are (1) permittivity ϵ (or dielectric constant), defined as the dielectric displacement per unit electric field, (2) the compliance s_{ij} of a material is the strain produced per unit stress. It's the reciprocal of the modulus of elasticity. The first subscript refers to the direction of strain, the second to direction of stress, (3) the piezoelectric charge constant d_{ij} , defined as the electric polarization generated in a material per unit mechanical stress applied to it. Alternatively, it is the mechanical strain experienced by the material per unit electric field applied to it. The first subscript refers to the direction of polarization generated in the material (at $E = 0$) or to the applied field strength, the second refers respectively to the direction of the applied stress or to the direction of the induced strain, (4) the piezoelectric voltage constant g_{ij} , defined as the electric field generated in a material per unit mechanical stress applied to it. Alternatively, it is the mechanical strain experienced by the material per unit electric displacement applied to it. The first subscript refers to the direction of the electric field

generated in the material or to the applied electric displacement, the second refers respectively to the direction of the applied stress or to the direction of the induced strain.

Consider a piezoelectric material with dimensions $L \times b \times h$ polled through its thickness with electrodes on the top and bottom surfaces (Figure 2.1). A mechanical force (F) is applied along the materials length. The generated voltage can be expressed in a number of different ways as shown below:

$$V = \frac{Fg_{31}}{b} = SY^Ehg_{31} = \frac{SY^Ed_{31}h}{\epsilon} \quad (2.1)$$

where V is the generated voltage, g_{31} and d_{31} are piezoelectric constants, S is the applied mechanical strain, Y^E is the short circuit elastic modulus and ϵ is the electrical permittivity. Another important property of piezoelectric materials is their capacitance. The capacitance of a piezoelectric generator is given by:

$$C = \frac{Lb\epsilon}{h} \quad (2.2)$$

Two different piezoelectric material classes are commonly used for electric energy harvesting. The first class of material is a ceramic composed of lead zirconate titanate (PZT), the second is a semi-crystalline plastic polyvinylidene fluoride (PVDF). These two materials have very different properties and are typically used for different applications. The mechanical and electrical properties of these two materials are compared in Table 2.1.

To illustrate the difference between the two materials, consider two piezoelectric strips 30 mm long and 12 mm wide. PVDF is typically formed in 28 μm thickness, while PZT is manufactured in thicknesses of 0.1 mm or thicker.

(1) For $L=30$ mm, $b=12$ mm, $T=28$ μm

PVDF film: $C = 1.36$ nF; $V = 12 \times 10^{-3}$ V/ $\mu\epsilon$

(2) For $L=30$ mm, $b=12$ mm, $T=100$ μm

PZT: $C = 38$ nF; $V = 65$ V/ $\mu\epsilon$

Though PZT can generate significantly more voltage than PVDF per unit strain, PZT is a brittle ceramic and thus can fracture at relatively low strains. Furthermore, tensile strains as low as 500 $\mu\epsilon$ can cause fatigue damage in PZT. On the other hand, PVDF is a flexible plastic that can withstand at least 10,000 $\mu\epsilon$ of applied tensile strain.

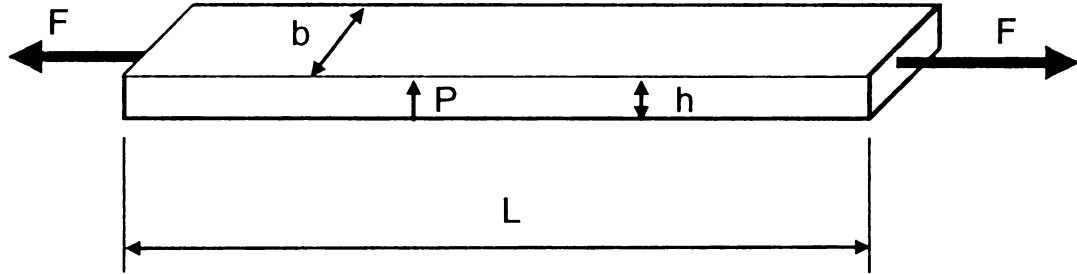


Figure 2.1 Schematic depiction of a piezoelectric material pulled by a force F . The material undergoes an axial strain S

Table 2.1 Comparison of material properties of two commonly used piezoelectric materials

Property	PVDF	PZT-5H
Young's Modulus (Y^E)	2×10^9 N/m ²	60×10^9 N/m ²
Permittivity (ϵ)	106×10^{-12} F/m	106×10^{-10} F/m
Piezo Strain Constant (d_{31})	23×10^{-12} C/N	110×10^{-12} C/N
Piezo Stress Constant (g_{31})	216×10^{-3} m/C	10×10^{-3} m/C

2.3 PIEZOELECTRIC MODELING

2.3.1 Strain Energy Harvesting

Piezoelectric material is typically used in two energy harvesting modalities. The first modality is by attaching the material to a substrate and applying a slowly changing

dynamic load (Figure 2.2(a)). A mathematical generator model can be expressed using a set of equations of the form:

$$\begin{cases} Ku - \Theta v = F \\ \Theta \dot{u} + C \dot{v} = I \end{cases} \quad u = SL \quad (2.3)$$

$$Energy = \int_0^t vI \, dt$$

where K is the stiffness, Θ is the electromechanical coupling coefficient, C is the piezoelectric capacitance, u is the displacement of the generator induced by the imposed strain S , F is the applied force, v is the generated voltage, and I is the circuit current. The mechanical and electromechanical parameters can be derived using a simplified Rayleigh-Ritz [44] approach and are given by:

$$K = \frac{Y^E h b}{L}$$

$$\Theta = Y^E d_{31} b \quad (2.4)$$

In this modality, the piezoelectric element can be modeled using a simple high-pass filter circuit as shown in Figure 2.2(b). The piezoelectric voltage generated is given by Equation (2.1). The capacitance is given by Equation (2.2). The nature of the high-pass filter circuit shows that very little voltage is generated for slow loading rates. The adequate matching of both the generated voltage and the capacitance to the applied mechanical load magnitude and frequency content is therefore critical for maximal electrical energy generation. It should be noted that the method of attachment (bond) of the piezoelectric material to its substrate in this modality is critical, and significant voltage loss (a factor as high as two to four) is common.

If the sensor circuit in Figure 2.2 is modeled by a resistor R_L , then for a harmonic loading of the piezoelectric transducer at a frequency f Hz, the magnitude of voltage across the sensor is given by:

$$V_L(f) = \frac{2\pi f R_L C V}{(1 + 4\pi^2 f^2 R_L^2 C^2)^{1/2}} \quad (2.5)$$

and the power delivered to the sensor can be expressed as:

$$P_L(f) = \frac{|v_L(f)|^2}{R_L} = \frac{4\pi^2 f^2 R_L C^2 V^2}{(1 + 4\pi^2 f^2 R_L^2 C^2)} \quad (2.6)$$

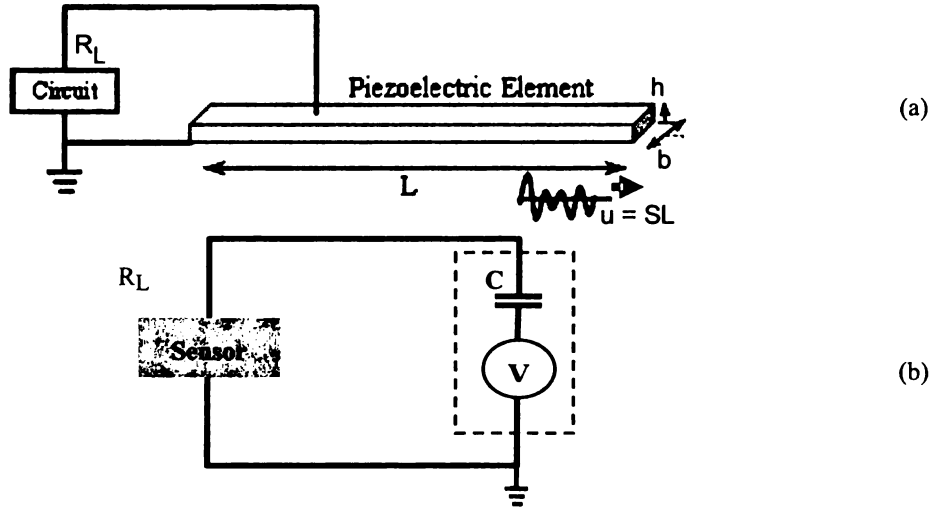


Figure 2.2 (a) Schematic of a piezoelectric scavenger of length L , width b and height h ; (b) Equivalent circuit diagram (the dashed block) for a piezoelectric material under slow dynamic loading

The maximum power that can be delivered at a loading frequency can be obtained by optimizing Equation (2.6) with respect to R_L which can be expressed as the condition:

$$\frac{dP_L}{dR_L} = \frac{4\pi^2 f^2 C^2 R_L V}{(1 + 4\pi^2 f^2 R_L^2 C^2)} - \frac{16\pi^4 f^4 C^4 R_L^3 V}{(1 + 4\pi^2 f^2 R_L^2 C^2)^2} = 0 \quad (2.7)$$

The optimal value of the load resistance R_L is then given by:

$$R_L = \frac{1}{2\pi f C} \quad (2.8)$$

For a loading frequency of 1 Hz and a transducer capacitance of 10 nF the optimal load according to Equation (2.8) is 15 MΩ. For a 5-V open circuit voltage, the optimal resistor would produce a current of 300 nA.

2.3.2 Vibration energy harvesting

2.3.2.1 Background

The second mode of energy generation is through higher frequency vibration. In this case the piezoelectric material is driven by ambient mechanical vibration.

The theoretical maximum energy that can be extracted from a vibration source can be estimated by calculating the energy dissipated through an equivalent damper. Figure 2.3 shows the schematic for a single-degree-of-freedom mass subjected to ground motion. An electrical energy harvester is included via an equivalent damper in parallel to the mechanical damper.

The governing equations for the theoretical energy harvester shown in Figure 2.3 are given by the standard dynamic equations:

$$M\ddot{u} + (c_m + c_e)\dot{u} + ku = -M\ddot{u}_g \quad (2.9-a)$$

$$Energy = \int_0^t c_e \dot{u}^2 dt \quad (2.9-b)$$

where M is the vibrating mass, c_m is the mechanical damping, c_e is the equivalent electric damping, k is the spring stiffness, x is the unknown relative displacement of the mass, and \ddot{u}_g is the prescribed ground acceleration.

A basic layout for a piezoelectric energy harvester is shown in Figure 2.4. The ambient vibration produces base acceleration, \ddot{u}_g , and this induces motion in the piezoelectric cantilever beam.

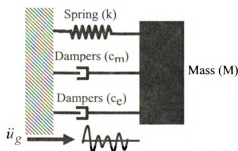


Figure 2.3 Theoretical energy harvester with an equivalent electric damper

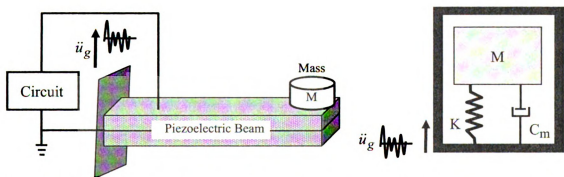


Figure 2.4 Schematic of a piezoelectric vibration scavenger of mass (M), length (L), width (b) and height (h). The equivalent mechanical single degree of freedom system is also shown

The material strains are converted into electrical charge through the piezoelectric effect. The generated charge is dissipated through the electronic circuit and thus acts to dampen out the vibration. The mathematically rigorous generator modeling approach typically leads to a set of equations of the form:

$$\begin{aligned}
M\ddot{u} + c_m\dot{u} + k_p u - \Theta v &= -M\ddot{u}_g \\
\Theta\dot{u} + C\dot{v} &= I \\
\text{Energy} &= \int_0^t v I dt
\end{aligned} \tag{2.10}$$

where k_p is the beam stiffness, Θ is the electromechanical coupling coefficient, C is the piezoelectric capacitance, x is the tip displacement of the beam with respect to the base, v is the generated voltage, and I is the piezoelectric current. The remaining symbols have the same meaning as in Equation (2.9). For a full description of piezoelectric beam modeling, the reader is referred to work in the literature [47, 48].

In general the complexity of solving Equation (2.10) arises from including the circuit current (I). By assuming that only a resistor (R) is connected to the generator, i.e. the “Circuit” in Figure 2.4 is made up of an equivalent single resistor, the current is expressed as $I = -v/R$, and Equation (2.10) can be solved using a numerical approach such as the Runge-Kutta method. In most instances however, a more complicated non-linear circuit is connected to the generator. Such circuits are significantly more difficult to analyze. The response of the electric circuit is typically solved using standard electrical engineering software such as SPICE. Accounting for the piezoelectric element within the circuit simulator remains a problem. Several two port models [45, 49, 50] and a 5 port piezoelectric model [46] have been proposed.

This work presents a simple one degree of freedom model (based on the previous work of [46, 48, 49]) that can be readily incorporated into any circuit simulation program (e.g. SPICE [89]) by using an equivalent circuit for the mechanical structure of the piezoelectric sensor. The presented model provides an accurate description for a single vibration mode that includes the backwards and forwards coupling between the electrical

and mechanical systems. The performance of the piezoelectric model attached to a relatively complex non-linear circuit is also compared with experimental results.

2.3.2.2 Simplified Mechanical and Equivalent Electrical Models

Most ambient vibration environments consist of a relatively narrow band vibration source characterized by a single dominant frequency. In this case a single degree of freedom damped oscillator, as shown in Figure 2.4, can capture the mechanical response adequately. The mechanical and electromechanical parameters (K , M , C_m , and Θ) can be either derived using simplified approach such as the Rayleigh-Ritz ([44, 47]) or by more complicated finite element methods. In many cases rectangular piezoelectric bimorph cantilevers generators are used. Table 2.2 summarizes the equivalent mechanical parameters and the Rayleigh-Ritz approximation. The mechanical parameters can also be measured experimentally as discussed below.

Table 2.2 Generator parameters assuming an Euler-Bernouli cantilever bimorph. The displacement shape function is assumed to be, $w = u(t)[1 - \cos(\pi x/(2L))]$ where x is the horizontal distance from the support. The electrical potential shape function is given by $\psi = zv/h$, where z is the vertical distance from the beam center, i.e, the beam's displaced shape. E is the modulus of elasticity of the beam, e_{31} is the piezoelectric coupling coefficient, ϵ is the electric permittivity, $I = bh^3/12$ is the second moment of area and \bar{m} is the mass per unit length.

Parameter	Approximation for Piezo Bimorph
K	$\frac{EI\pi^4}{32L^3}$
M	$M_{tip} + \bar{m}L\left(\frac{3\pi - 8}{2\pi}\right)$
Θ	$\frac{e_{31}bh\pi}{2L}$
C	$2\epsilon\left(\frac{bL}{h}\right)$

Equation (2.10) can be represented by the equivalent electric circuit of the mechanical and electromechanical nature of the harvester as shown in Figure 2.5 (see [46] and [35]). The advantage of this model is that it can be analyzed easily using only a standard circuit simulation program such as SPICE.

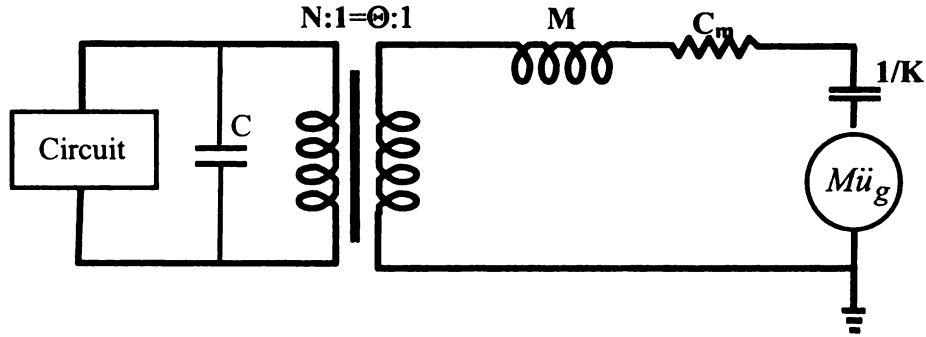


Figure 2.5 The equivalent circuit for a single degree of freedom piezo-generator. The mechanical force input is simulated as a voltage generator element with magnitude $M\ddot{u}_g$

2.3.2.3 Experimental Validation of Models

A- Using Lead Zirconate Titanate (PZT) in a High Frequency Environment

A relatively simple experimental method of measuring the generator parameters is illustrated in Figure 2.6. The piezoelectric generator is attached to a mechanical vibrator and its open-circuit voltage response is measured over a range of input frequencies, in the region of the resonant frequency of the generator. The open-circuit voltage can be measured using a high impedance oscilloscope. This experimental method is applicable for the measurement of any generator configuration. The tip mass and capacitance of the piezoelectric generator can be measured directly. From Table 2.2, approximately 20% of the piezoelectric mass can be added to the tip mass to give a sufficiently accurate estimate of the effective mass.

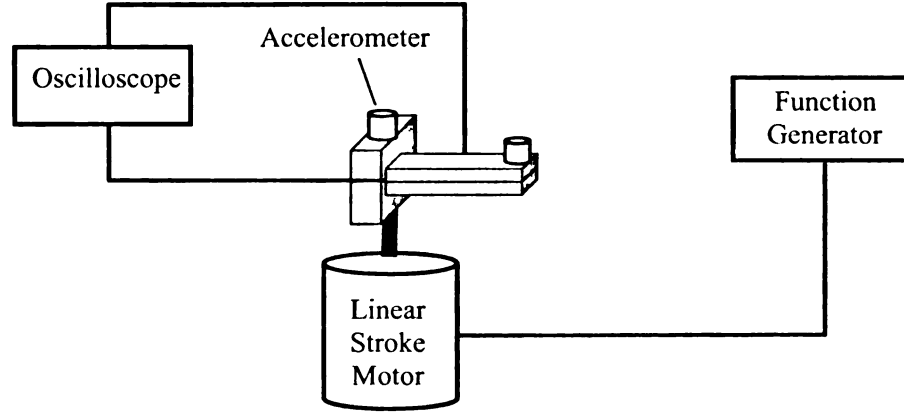


Figure 2.6 Method of experimentally measuring piezoelectric generator parameters. The vibrator is driven over a range of frequencies to obtain the open-circuit voltages. The accelerometer is used to measure the base excitation \ddot{u}_g directly

For the open-circuit case, Equation (2.10) can be reduced to

$$\begin{aligned}
 M\ddot{u} + C_m\dot{u} + (K + \Theta^2 / C)u &= -M\ddot{u}_g \\
 v &= -\frac{\Theta u}{C} \\
 |TF| &= \frac{\Theta M}{C} \left| \frac{1}{-M\omega^2 + i\omega C_m + (K + \Theta^2 / C)} \right|
 \end{aligned} \tag{2.11}$$

where $|TF|$ is the magnitude of the voltage-acceleration transfer function and ω is the driving frequency of the excitation.

Figure 2.7 shows an experimentally measured transfer function for a piezoelectric 35mm diameter unimorph PZT disk (CEB-35D26, CUI Inc., Tualatin, OR) clamped on one edge. A non-linear least square curve fitting routine can be used to estimate the stiffness (K), damping ratio (ζ) ($\zeta = C_m / 2\sqrt{MK}$) and mechanical coupling coefficient (Θ). It is suggested that the stiffness and damping ratio are then independently checked by measuring the open circuit voltage in a ring-down (free-vibration) test.

The equivalent circuit model shown in Figure 2.5 can be validated by using a standard full-bridge generator circuit as shown in Figure 2.8. The full-bridge diode circuit is typic-

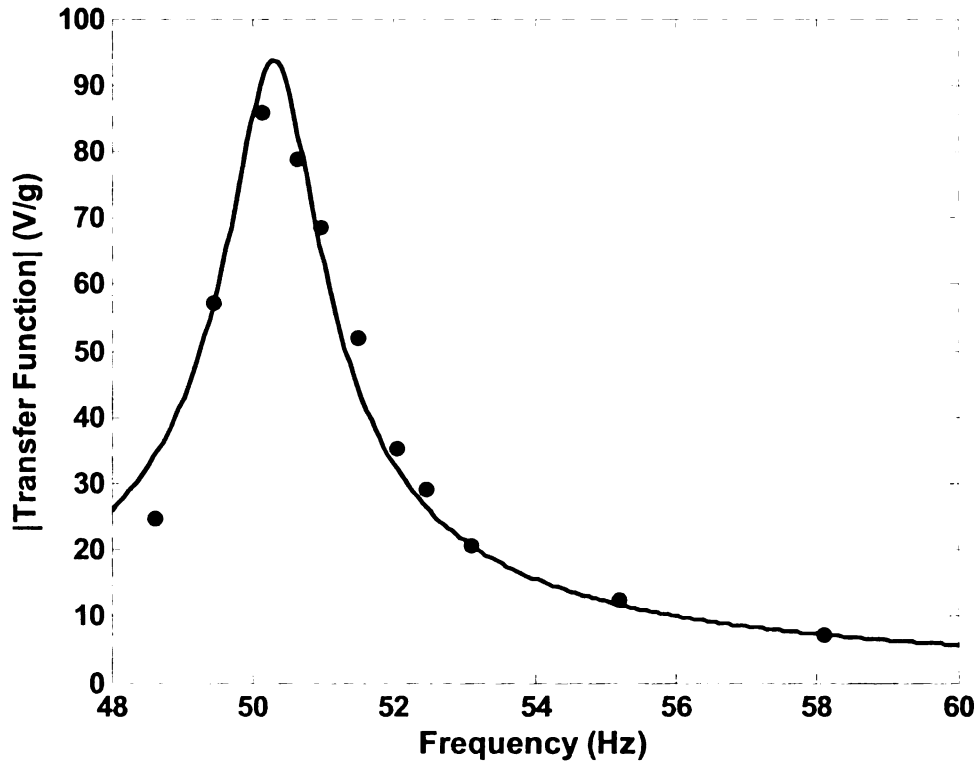


Figure 2.7 Open-circuit piezoelectric voltage transfer function (the least square fitted model is shown as a solid line, and the experimental results are shown as dots). The non-linear least square fitted parameters are $K=985\text{N/m}$, $\Theta=6\times 10^{-4}\text{C/m}$, and $\zeta=1.3\%$. The measured parameters are $M_{tip}=9.4\text{g}$ and $C=25.2\text{nF}$. The coefficient of correlation is $r=0.98$

ally used to collect the generated electric charge on the storage capacitor (C_s). A drainage resistor (R_d) can also be attached to the storage capacitor to represent leakage through the rest of the circuit and through C_s .

Using the same mechanical vibration setup as shown in Figure 2.6, except now connecting the harvesting and storing circuit of Figure 2.8, the voltage on the storage capacitor can be measured for a set time over a relatively wide range of acceleration input frequencies and magnitudes. As explained above, an electric simulation program (e.g,

SPICE) can be used to predict the response of the harvester and electronic circuit. The measured and calculated voltages over the storage capacitor are compared in Figure 2.9-a for the disk unimorph piezoelectric generator described in Figure 2.7. The simulated and experimental time history of the voltage stored on the capacitor show good agreement (Figure 2.9-b). For smaller storage voltages, the simulated and measured results tend to show worse agreement. A number of factors contribute to this worse agreement, including the resolution error of the measurement equipment (accelerometer etc.), and the low-voltage behavior of the diode model.

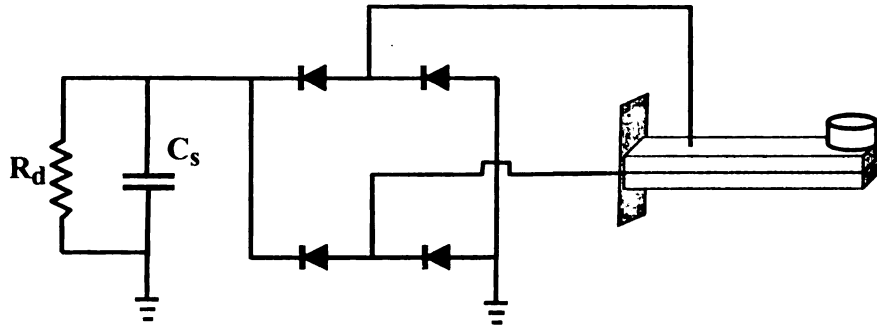
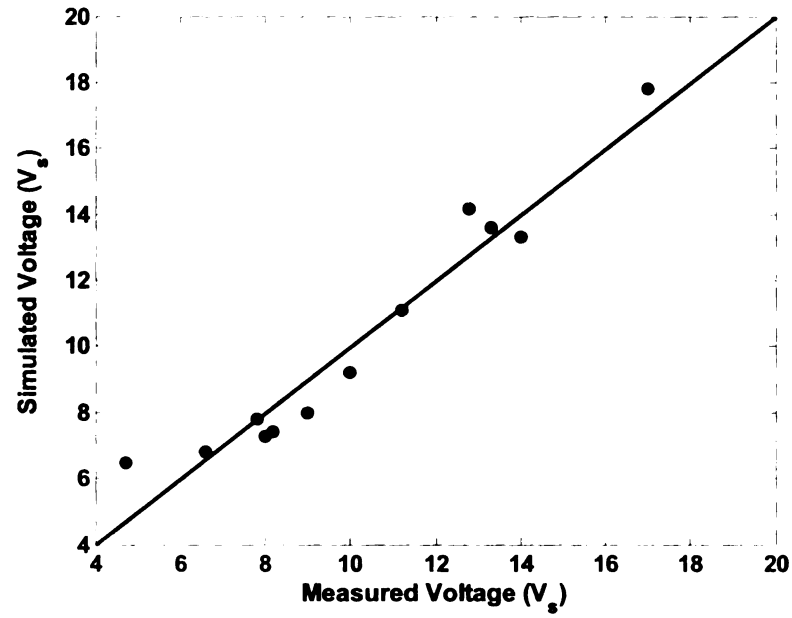
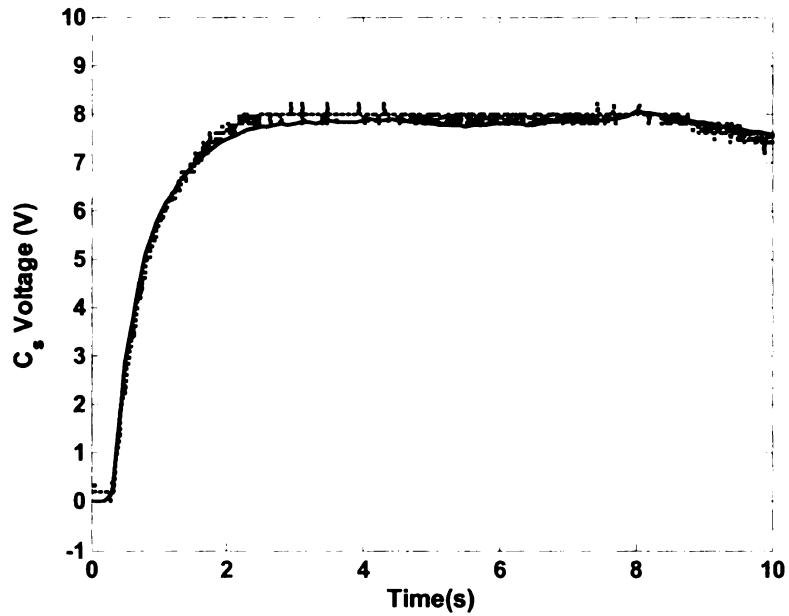


Figure 2.8 A full diode bridge piezoelectric circuit for storing electrical charge on a capacitor (C_s), the circuit leakage is represented by the resistor (R_d)

It should be noted that, in general, PZT-based energy harvesters would be significantly more efficient in converting mechanical energy to electrical energy due to their higher electromechanical coupling coefficient ($e = 20 \text{ C m}^{-2}$ for PZT compared to 0.07 C m^{-2} for PVDF). However, the brittleness of PZT-based sensors makes them difficult to use for practical applications. The damage strain for PZT is on the order of $500 \mu\epsilon$ (compared to a yield strain of 1.5% for PVDF). Once over-strained, PZT loses a significant fraction of its piezoelectric properties, even without any visible cracking. Several PZT bimorph



(a)



(b)

Figure 2.9 (a) Measured and calculated voltages for the piezoelectric unimorph with properties calculated from Figure 2.7. The input accelerations are compared at 5 seconds after the linear stroke motor is switched on. The circuits elements properties are: storage capacitor $C_s = 3.3 \mu\text{F}$; drain resistance $R_d = 10 \text{ M}\Omega$, and diodes 1N4148. The line represents equal measured and calculated voltages, the coefficient of correlation, assuming the simulated voltage is equal to the measured voltage is $r=0.97$; (b) a simulated (solid) and experimental (dashed) voltage time history on the storage capacitor

specimens were over-strained during routine handling in the laboratory. Furthermore, the elastic modulus of PZT is approximately 25 times greater than that of PVDF. Thus, for the same geometric dimensions, a PZT beam would have a resonant frequency of approximately five times greater than PVDF. This becomes a significant effect in terms of energy conversion for low-frequency excitations that are typical for most civil engineering structures. It is possible to overcome the brittleness issue of PZT by using fiber geometries and embedding them in epoxy to form advanced composite materials. However, this procedure significantly complicates their use, and is beyond the scope of this thesis.

B- Using Polyvinylidene Fluoride (PVDF) Under Low Frequency Environment

To check the validity of the energy harvester model under dynamic loading, simplified experiments were performed. The experimental results were then compared to the predictions of the theoretical model. The first experiment consisted of measuring the voltage transfer function of a piezoelectric scavenger. The piezoelectric beam was subject to base excitation. In the second experiment, the piezoelectric scavenger was subject to a simulated earthquake ground acceleration history. The time response of the generated voltage was then measured.

In all the experiments, a standard commercial unimorph piezoelectric sensor (LDT1-028-from MSIUSA Inc.) was used. The piezoelectric unimorph consists of a single layer of active piezoelectric material (PVDF) attached to mylar plastic. The properties of the material (from MSIUSA Inc.) for the sensor are summarized in Table 2.3. The sensor

geometry is shown in Figure 2.10. This material is a polymer and hence much easier to handle and use than the brittle PZT ceramic.

Table 2.3 Piezoelectric Sensor Properties

Piezoelectric (PVDF) Properties	
Modulus of Elasticity	$c_p=3\text{GPa}$
Capacitance	$C=1.38\text{nF}$
Piezoelectric coupling coefficient	$E=0.07\text{C/m}^2$
Density	$\rho_p=1780\text{kg/m}^3$
Piezoelectric thickness	$h_p=28\mu\text{m}$
Length	$L=31.7\text{mm}$
Width	$b=16\text{mm}$
Backing (Mylar) Properties	
Modulus of Elasticity	$c_b=3.79\text{GPa}$
Backing thickness	$h_b=172\mu\text{m}$
Density	$\rho_b=1390\text{kg/m}^3$
Resistance	$10\times 10^6\Omega$
Tip Mass	$M_{tip}=1.2\text{g}$
Beam Stiffness (Calculated)	$K=3.6\text{N/m}$
Lumped Mass (Calculated)	$M=1.23\text{g}$
Electromechanical Coupling (Calculated)	$\Theta=3.69\times 10^{-6}\text{C/m}$
Capacitance (Measured and Calculated)	$C_{EXP}=1.38\text{nF}$ and $C_{CAL}=1.41\text{nF}$
Damping (Measured)	$B=5.1\times 10^{-3}\text{Nm/s}$
Natural frequency (Measured and Calculated)	$F_{EXP}=8.7\text{Hz}$ and $f_{CAL}=8.6\text{Hz}$

For the theoretical model, a shape function of the form $w = d(t)[1 - \cos(\pi x/2L)]$ for the deflection of the beam and a potential shape function of $\psi = vz/h_p$ are assumed. The stiffness (K), mass (M), electromechanical coupling (Θ) and capacitance (C) can be readily calculated, assuming an Euler–Bernoulli beam and using the Rayleigh–Ritz approach. These results are summarized in Table 2.3. The damping coefficient is

calculated by fitting the theoretical voltage–acceleration transfer function to the experimentally measured transfer function.

Figure 2.11 shows the experimental setup. A servo-hydraulic actuator was used to provide a controlled displacement to the unimorph piezoelectric sensor. The piezoelectric sensor was attached to the actuator's cross-head using epoxy. Both the voltage across the resistor (R) and the displacement from the servo-hydraulic machine were measured and acquired by a data acquisition system.

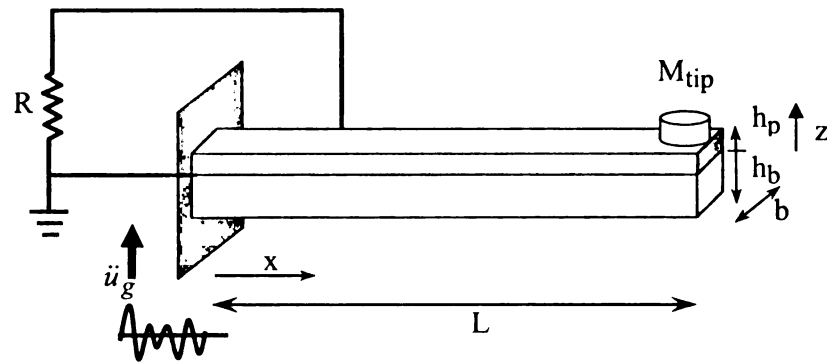


Figure 2.10 Schematic representation of a PVDF vibration energy scavenger

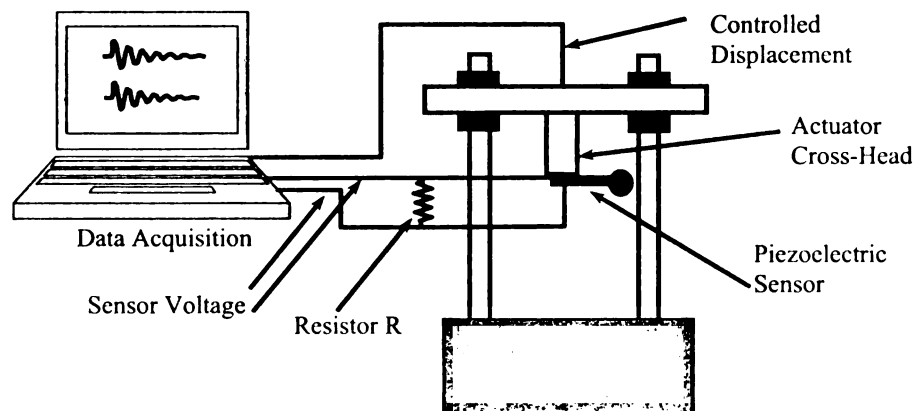


Figure 2.11 Experimental setup to test the piezoelectric bimorph generator

The transfer function was obtained by manually inputting a number of different sinusoidal displacements and measuring the output sensor voltages. The magnitudes of the experimental and theoretical voltage–acceleration transfer function are shown in Figure 2.12. The theoretical model shows good agreement with the experimental results.

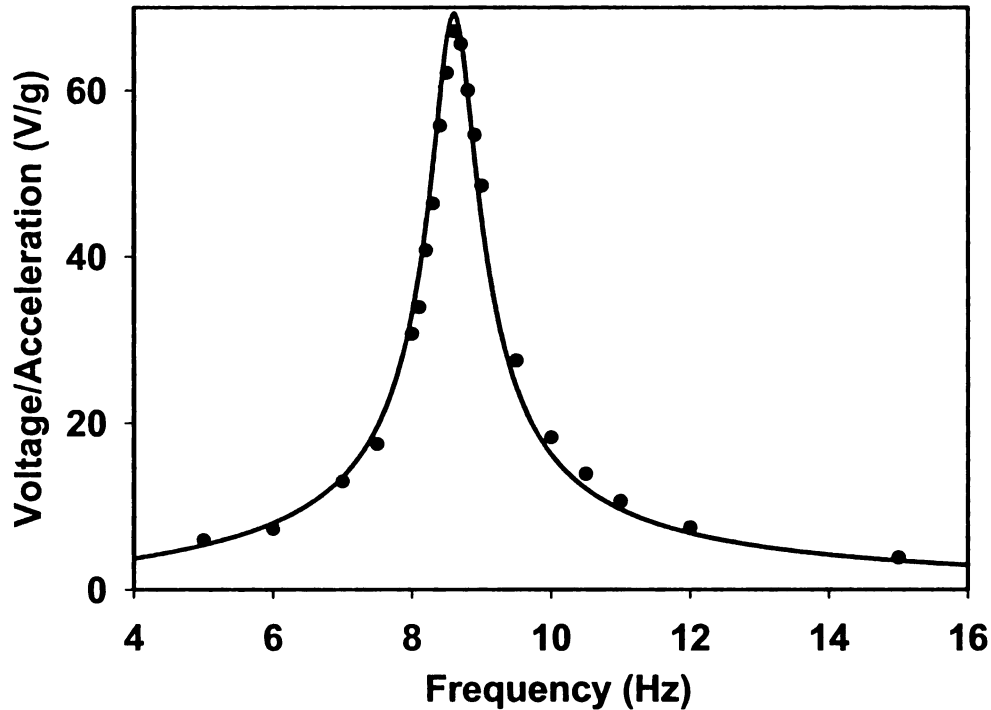


Figure 2.12 Experimental (dots) and theoretical (line) acceleration–voltage transfer function for piezoelectric energy harvester

In the second experiment, the 1940 El Centro earthquake’s displacements were input into the actuator. The El Centro earthquake’s displacement time-history is obtained by doubly integrating the acceleration record and filtering the very low-frequency components (a cut-off frequency of 0.5 Hz was used). Time-history records of El Centro are shown in Chapter 3 (Figure 3.3). The filtering eliminates the large deflection error (i.e. drift) caused by the numerical double integration of the acceleration record. Since

only a small fraction of the El Centro earthquake's energy is less than 0.5 Hz, this filtering should not have a significant effect on the energy calculations. Figure 2.13 shows the theoretically simulated and experimentally measured voltages for part of the El Centro earthquake. The calculated converted electrical energy for the entire 50s El Centro earthquake is $0.43 \mu\text{J}$, while the measured electrical energy is $0.49 \mu\text{J}$. These values are in good agreement.

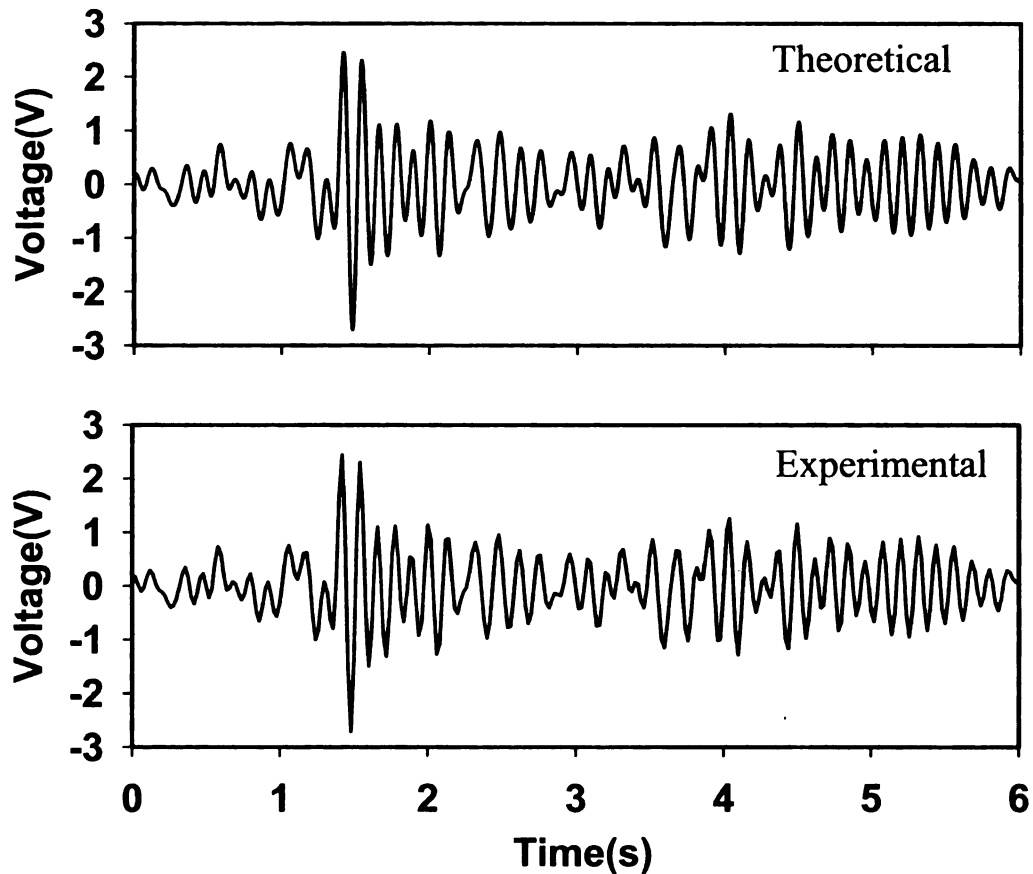


Figure 2.13 Theoretical and experimental results for the piezoelectric energy generator subjected to the El Centro earthquake (only 6 s is shown for clarity)

2.4 CONCLUSION

This chapter has presented simple methods of modeling and estimating the performance of piezoelectric energy harvesters. A two step approach can be used to estimate first the electromechanical piezoelectric properties (either using a simple Rayleigh-Ritz model or by experimental measurements). The estimated piezoelectric properties can then be incorporated into an equivalent electric network that can be readily solved by any circuit simulation program such as SPICE.

The proposed mechanical and electrical models show good agreement with measured circuit performance for a typical non-linear circuit.

Since only one degree of freedom models are used for the vibration piezo-harvester, it is limited to analyzing relatively narrow band excitations and generators without closely spaced mechanical vibration modes. For the case of a rectangular cantilever generator analyzed in this study, it can be shown that the second generator mode has a resonant frequency of approximately nine times the first. Thus in the unlikely situation where the vibration source has a significant frequency component at the second generator mode, it can be ignored without sacrificing the accuracy of the proposed method.

CHAPTER 3

FEASIBILITY OF STRUCTURAL MONITORING WITH VIBRATION POWERED SENSORS

3.1 INTRODUCTION

The ability to monitor infrastructure using a sensor network could provide significant benefits. For example, the load history could be used to predict the life expectancy of the structure. The structure's vibration signature can be used to identify the location and extent of damage. Currently, a number of techniques exist to monitor large-scale infrastructure [26, 27, 29]. These include conventional resistive strain gauging, embedded or attached optical fiber sensors, accelerometers and linear variable displacement transducers. The major issues with these monitoring methods are implementation cost, ruggedness/robustness, data interpretation and, most importantly, powering. The implementation cost of a single sensor is gradually decreasing with the introduction of wireless sensor networks which can eliminate some of the implementation problems and costs associated with providing hardwired communication lines [9].

One of the major problems associated with implementing wireless (and wired) sensor networks is providing continuous power to each of the sensor nodes. To date, batteries have been the primary means of powering wireless devices. Battery power can last anywhere from a few days to 10 years. For practical infrastructure monitoring, it is desirable that the sensors last the service lifetime of the structure; typically, a structure's lifespan is several decades, but it can be as long as 100 years. For example, one study of concrete bridges has shown that their expected lifetimes range from 44 to 83 years [51]. Even with the continued trend of decreasing the power consumption of electronic

systems, it is likely that battery self-discharge would limit the useful lifetime of any sensor to 10 years. For structures and embedded sensors, it is impractical and costly to change batteries periodically through the lifetime of the structure.

The problems associated with powering wireless sensors have led several research groups to investigate self-powering as a means of providing continuous power to remote sensors. In the context of this thesis, self-powering refers to the ability of the device to ‘harvest’ (sometimes referred to as ‘scavenge’) ambient energy from its environment, and convert it to electrical energy.

A number of energy harvesting techniques are being investigated and implemented. These techniques are based on one of the following: solar energy, thermal gradients, and vibration energy. The most successful energy harvesters to date use solar power. However, for structural monitoring, where sensors could be embedded (as in concrete structures), it is not always feasible to use solar powering. Using heat or thermal gradients provide energy levels that are too low to power sensors for infrastructure monitoring [52] (see Table 3.1). Currently, several research groups are developing energy harvesters based on ambient vibration energy [52, 48].

The aim of this chapter is to investigate the electrical energy that can be generated from motion in high vibration civil environments and typical civil structures such as bridges and buildings. The generated energy levels will be produced by: (1) routine (service) loading, and (2) extreme loading conditions, in particular earthquakes. Vibration histories used in this work have been gathered from published data. The mechanical-to-electrical energy conversion for a piezoelectric generator is modeled theoretically (Chapter 2). The

Table 3.1 Comparison of Energy Scavenging Sources [52]

	Power Density ($\mu\text{W}/\text{cm}^3$) 1 Year lifetime	Power Density ($\mu\text{W}/\text{cm}^3$) 10 Year lifetime	Source of information
Solar (Outdoors)	15,000- direct sun 150- cloudy day	15,000- direct sun 150- cloudy day	Commonly Available
Solar (Indoors)	6- office desk	6- office desk	Experiment
Vibrations	100-200	100-200	Experiment and Theory
Acoustic Noise	0.003 @ 75 Db 0.96 @ 100 Db	0.003 @ 75 Db 0.96 @ 100 Db	Theory
Daily Temp. Variation	10	10	Theory
Temperature Gradient	15 @ 10 °C gradient	15 @ 10 °C gradient	
Strain (Piezoelectric)	330	330	Starnier 1996 [53] Shenck and Paradiso 2001 [54]
Batteries (non-recharg. Lithium)	89	7	Commonly Available
Batteries (rechargeable Lithium)	13.7	0	Commonly Available
Gasoline (micro heat engine)	403	40.3	Mehra, 2000 [55]
Fuel Cells (methanol)	560	56	Commonly Available

required energy consumption for performing various electrical processes in a low-power sensor is also reported. These required energy levels are compared to the generated electrical energy.

3.2 ELECTRONICS AND SUBSYSTEM POWER CONSUMPTION

The power consumption and size of integrated circuits are continuing to decrease, while their speeds are increasing. It is now becoming feasible to embed electronics in everyday objects to enhance their usability and performance. In structural monitoring, a typical wireless sensor node would consist of the sensor, an embedded microprocessor, digital logic circuits, radio receiver, radio transmitter, a timer and a multi-channel analog-to-digital converter. Current commercial electronics have sleep-power consumptions as low as 200 nW (for example, the MSP430 microprocessor by Texas Instrument). The same processor is capable of operating at 0.5 million operations per second, consuming 350 μ W. Commercially available whole sensor nodes (such as Telos by Moteiv Corp.) require approximately 50 mW to run their sampling, processing and radio transmission functions. These commercial sensor nodes typically process and transmit wireless data at 250×10^3 bits s^{-1} . This would allow the sensor to process and transmit approximately 500 bytes of data per millijoule. The central question is how much energy can a power harvester generate?

Table 3.2 shows the approximate energy consumption of commercial and research electronics. It should be noted that the power consumption shown in Table 3.2 corresponds to a continuous energy supply.

Table 3.2 Approximate energy consumption in a wireless sensor node (references in brackets). Volatile memory (VM) is assumed to be replaced by low-power non-volatile memory (NVM) [56]

Operation	Commercial	Research
Microprocessor Operation ⁺	350 μ W [62]	20 μ W [57]
Receive 1 bit	200 nJ [65]	12 pJ [59]
Transmit 1 bit	200 nJ [60]	16 pJ [59]
Retain Volatile Memory (VM) – 1 bit	100 pW [62]	Replaced by NVM
Write 1 bit to NVM	200 nJ [61]	25 pJ [63]
Analog-Digital (A/D) Conversion – 1bit	2 nJ [62]	50 pJ [59]
Sleep	300 nW [62]	5 nW [59]
Digital Signal Processing ⁺	200 μ W [64]	20 μ W [57, 58]
Pin Leakage	100 nW [62]	2.2 nW [66]

⁺ Operation is scaled to processor speeds of 500 kHz

3.3 PRACTICAL CONSIDERATIONS

The vibration harvester should allow volume for the beam element, suspended mass, electronic circuits and space for deflection under vibration. For example, consider a piezoelectric energy harvester shown in Figure 3.1. Significant volume is taken up by actual displacements of the beam and mass under base excitation.

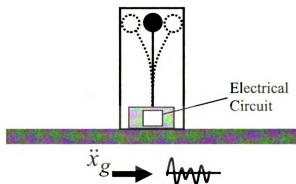


Figure 3.1 Schematic of a piezoelectric vibration scavenger

Practical manufacturing considerations would also have to be taken into account. For example:

(a) It might be impossible to match the optimum beam stiffness with current ceramic piezoelectric materials.

(b) Handling thin ceramic piezoelectric wafers is difficult due to their brittleness.

3.4 VIBRATION ENERGY HARVESTING IN TYPICAL CIVIL ENVIRONMENTS

Vibrations are induced in structures due to commonly occurring dynamic loads such as wind, traffic movement, and more severe loadings such as ground motion (earthquakes). Figures 3.2 and 3.3 are included to demonstrate the magnitude and duration of typical ground accelerations to which the power harvester can be subjected. It is well known that most civil engineering structures have fundamental vibration modes that occur at frequencies less than 5 Hz. Furthermore, typical dynamic load frequency spectra range from 0 to 5 Hz. Structural accelerations have been measured for different structures, subject to typical loading conditions by many research groups. One example acceleration time trace and frequency spectrum for a concrete bridge with traffic loads is shown in Figure 3.2 [67]. Monitoring behavior and performance under severe loading conditions such as earthquake or blast loading is paramount to assess the safety of the structure. A collection of ground accelerations for a large data set of earthquakes is available from the US Geological Survey; this data set can readily be used to test power harvesting schemes in monitoring civil structures. One well studied and commonly used earthquake time-history benchmark—the 1940 El Centro earthquake—is shown in Figure 3.3(a). Figure 3.3(b) shows the acceleration frequency spectrum for this earthquake.

In general, acceleration magnitudes at a particular location of a structure are affected by

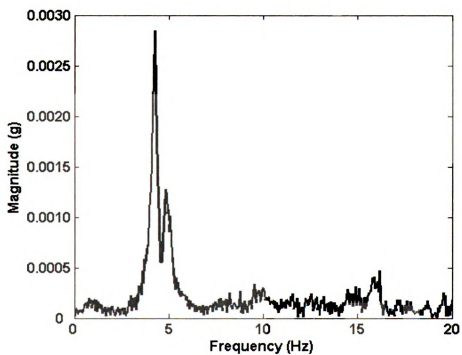
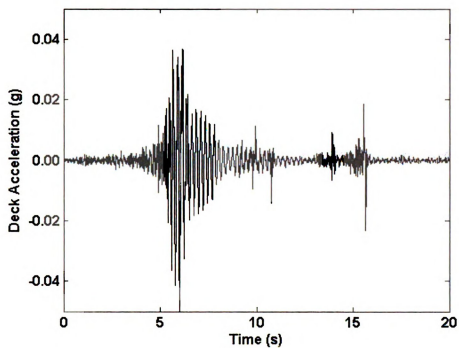


Figure 3.2 (a) Time-history and (b) frequency spectrum for the acceleration measurements from the deck of a concrete bridge under traffic loading [67]

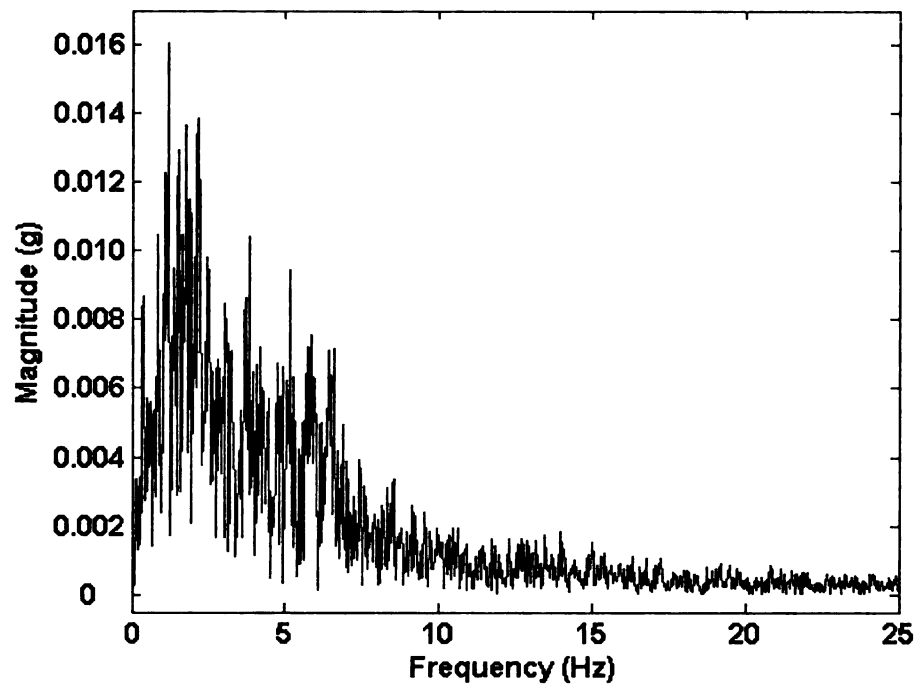
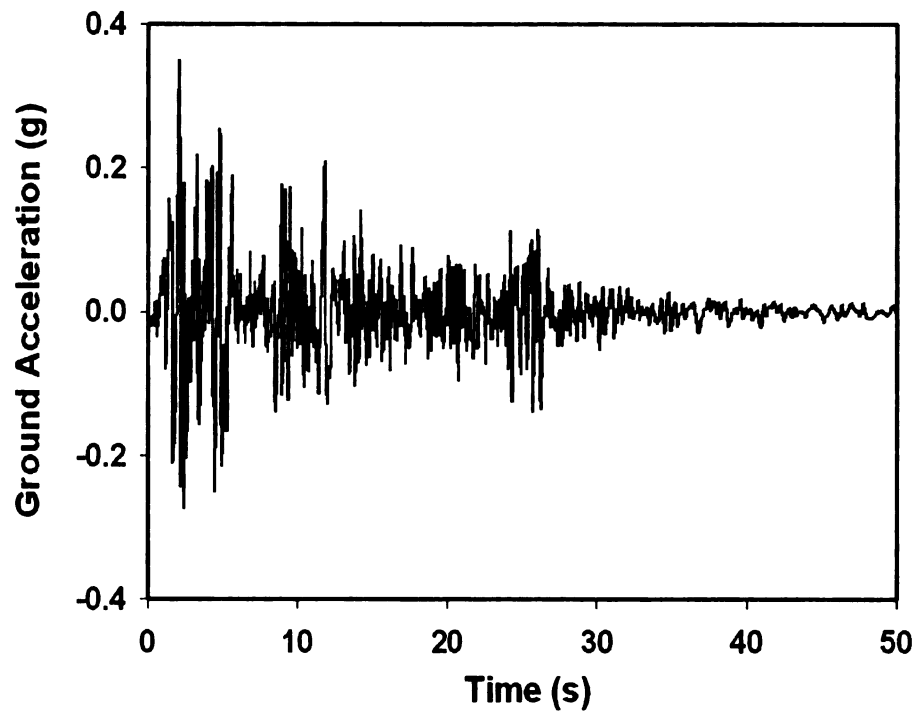


Figure 3.3 (a) Ground acceleration time-history and (b) frequency spectrum from the El Centro earthquake (North-South direction)

loading magnitude, structure type, construction materials and methods.

3.4.1 Harvestable Power

For this study, published data has been used as input to the convertible electrical energy model during service and extreme structural dynamic loading. As both energy scavenging techniques and power conversion efficiencies improve with future research, the maximum energy conversion will not exceed the maximum theoretical power level calculated from Equation (2.9). In this study, the maximum volume of one sensor node is constrained to be 5 cm^3 . This relatively small volume is approximately the size of a large concrete aggregate (roughly 20 mm in diameter [37]). Thus, existing concrete manufacturing methods can be used to incorporate the sensor within the structure. This is also the approximate size of other currently developed embedded sensors such as the ‘Smart Pebble’ [68]. It has been clearly shown that the mechanical properties of inclusions in concrete have a significant effect on its strength [69]. Thus, limiting the size of the sensor would reduce the impact of the sensor on the overall strength of the structure. Neither sensor cost nor implementation feasibility is considered.

For a simplified pure sinusoidal structural vibration, with acceleration magnitude A and frequency ω , the maximum possible mean power that can be extracted is readily derived from Equation (2.9) and is given by:

$$P = \frac{c_e \omega^2 A^2 M^2}{2[\omega^2 (c_e + c_m)^2 + (M\omega^2 - k)^2]} \quad (3.1)$$

The power (P) given by Equation (3.1) is plotted for various vibration frequencies, ω , in Figure 3.4. In this Figure it is assumed that the mechanical vibration resonant frequency

is 1 Hz, the amplitude of the input acceleration is 0.1g, the mass is 10 g, and the mechanical damping ratio (ζ_m) is 5%. Figure 3.5(a) shows the maximum vibration magnitude (when the resonant frequency of the energy harvester is equal to the frequency of the applied mechanical vibration) for various mechanical (ζ_m) and electrical damping ratios (ζ_e). Figure 3.5(b) shows the normalized frequency bandwidth for the various mechanical and electrical damping ratios. The bandwidth (BW) is taken as the frequency difference between the points where the power is $P_{\max}/\sqrt{2}$. In general, the bandwidth increases with increasing total damping.

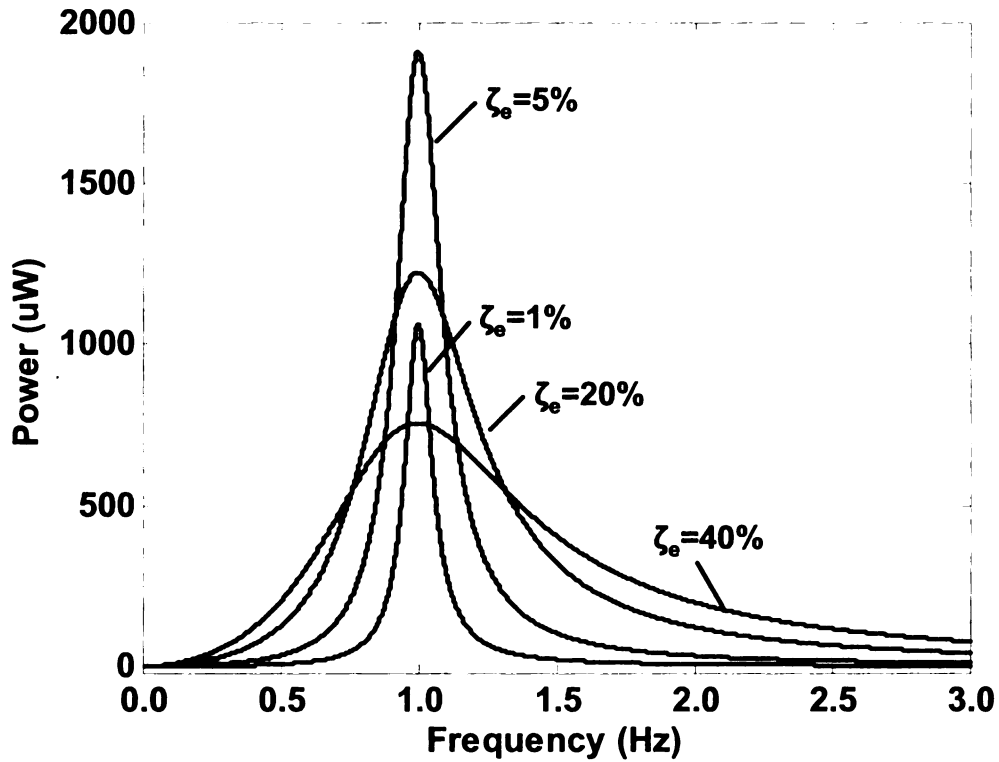


Figure 3.4 Theoretical average power output for various electric damping ratios. The mechanical damping is assumed to be 5%.

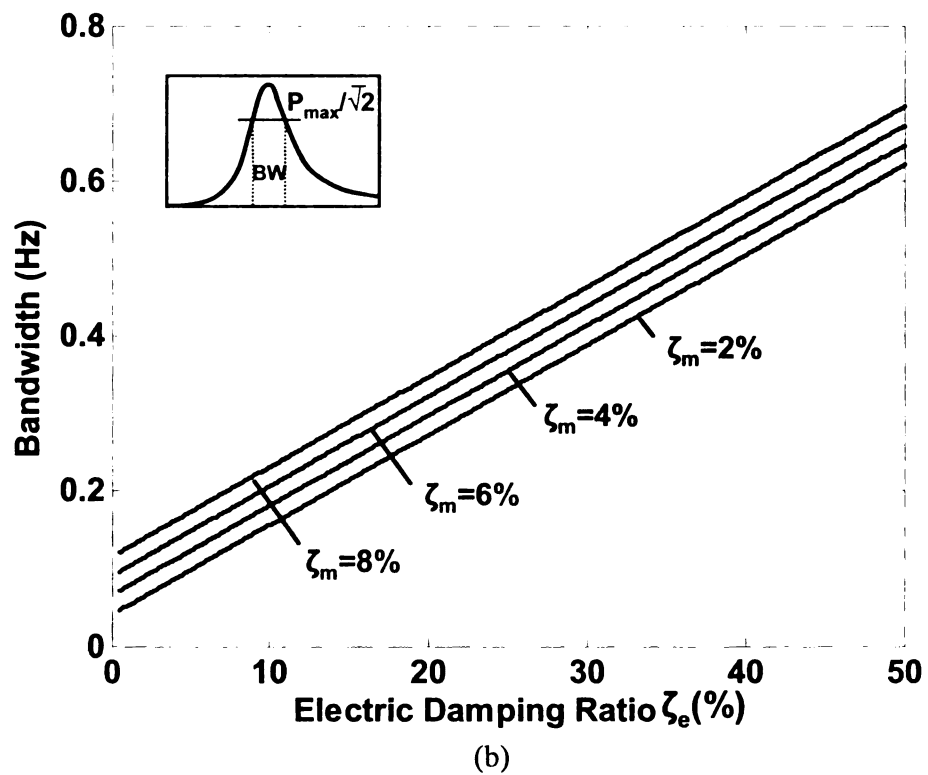
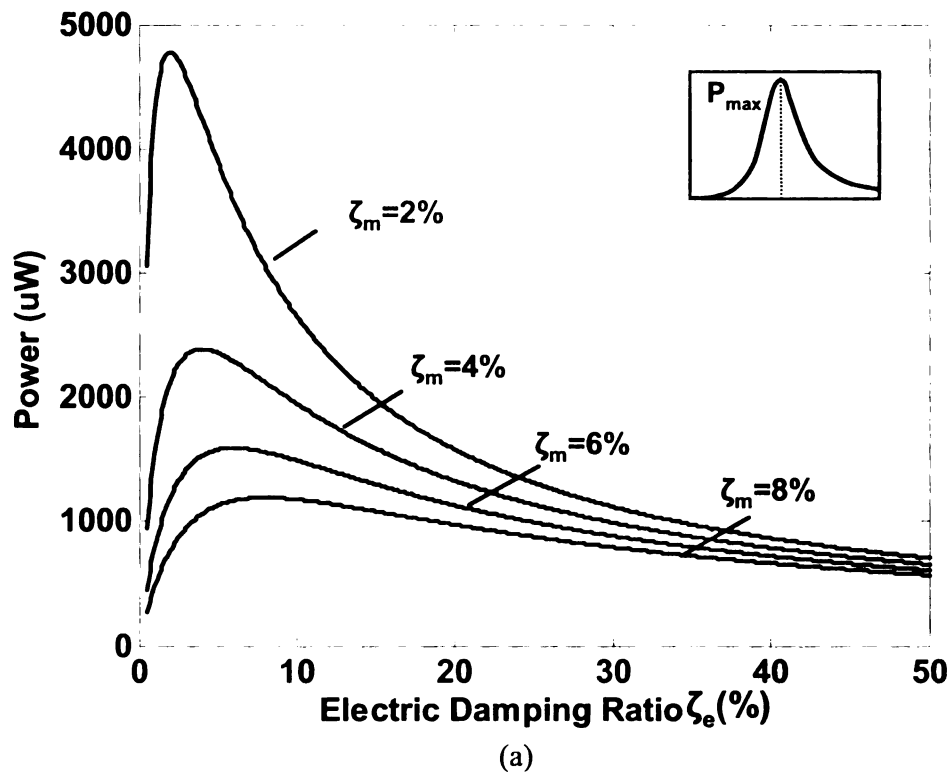


Figure 3.5 (a) Maximum power and (b) bandwidth for various electrical and damping ratios

From Figure 3.5, it can be seen that there is an optimal electrical damping ratio for which the magnitude of the generated power (P_{\max}) is a maximum. For the values assumed, the optimal electrical damping ratio (ζ_e) is 5%. It should also be noted that the bandwidth of the harvested power is also an important metric since, in general, the input spectrum for dynamic loading is not given by a single frequency but by a frequency spectrum. Thus it is possible that the maximum power that can be generated from a particular dynamic excitation would be greater for an energy scavenger with less maximum power output at resonance but with a broader bandwidth. Equation (3.1) shows that increasing the sensor vibrating mass increases the maximum power that can be generated.

3.4.2 Maximum Theoretical Harvestable Power

In this work, half the sensor volume is assumed to be occupied by the mass. The rest of the volume is taken by electronics and free space to allow for vibration. Assuming a density of $10\,000\text{ kg m}^{-3}$ (the approximate density of heavy metals such as silver, lead etc), the 5 cm^3 volume constraint gives a maximum tip mass is 25 g. Structural damping is typically between 2 and 5% of critical damping, thus the mechanical damping is taken as 4%. The maximum deliverable power for any vibration excitation can be found by searching for the optimum stiffness (k) and electrical damping (c_e).

In the calculation for the magnitude of energy that is harvestable under various loading conditions, the Wilson–Theta time-step integration method was applied to Equation (2.9-a), to obtain the response of the single-degree-of-freedom system. The total kinetic

energy for the loading time-history was then computed by numerically integrating Equation (2.9-b).

Three dynamic loading types were considered: earthquake, wind and traffic. The earthquake data was obtained from 32 different earthquakes (COSMOS - Consortium of Organizations for Strong Motion Observation Systems). Acceleration data for wind and traffic was obtained directly from researchers [70, 67] and from published data [71, 72, 73].

The resulting maximum harvestable energy is plotted in Figure 3.6. The results are segregated by structure type, subject to various loading conditions. It should be noted that the extreme earthquake event (labeled '1' in Figure 3.6) is for the Llolleo earthquake which occurred in Chile in 1985. The Llolleo earthquake is one of the longest large-magnitude earthquakes in recorded history. Also note that the maximum energy that would be harvested for tall buildings (labeled '2') is for a 44-story building subjected to a small earthquake [71]. Point 3 in Figure 3.6 is the maximum energy that would be harvested from the flexible Calgary tower subject to 100 km h^{-1} wind gusts; this wind speed corresponds to 62% of the design wind load [73].

As noted previously, the sensor stiffness and electrical damping levels were optimized to provide for maximum electrical energy output. In Figure 3.6, the optimal stiffness for maximum electrical energy output ranges from 0.1 to 20 N/m. The optimal electrical damping coefficient ranges from 5% to 43%. Electrical energy is presented instead of electrical power since, in all investigated cases, the loading events tend to be discrete (i.e., lasting a finite time). Thus it might be misleading to quote average power, which could imply that continuous electrical power is available for the sensor node. For the wind-

loading cases that tend to be more continuous in nature, the loading record was calculated for a period of 30s. In the earthquake and traffic loading, all loading durations ranged from 30 to 60s.

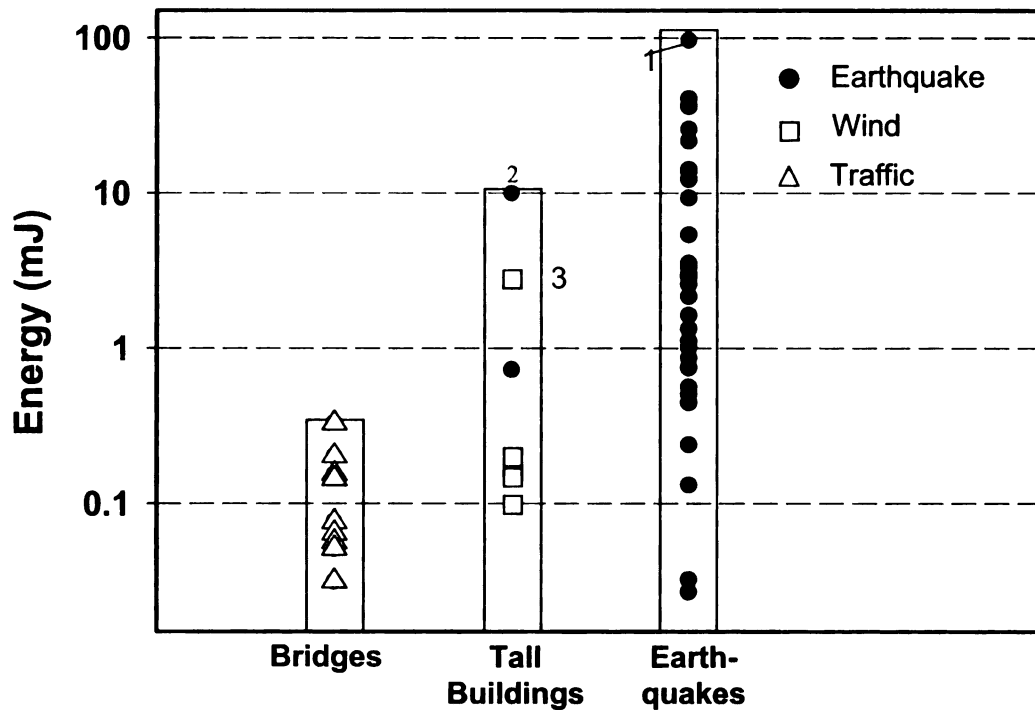


Figure 3.6 Maximum theoretical vibration energy for various structures and loading conditions

3.4.3 Piezoelectric Energy Conversion Efficiency

The energy levels shown in Figure 3.6 are the maximum achievable values for a 5 cm^3 vibration scavenger (i.e, it assumes that all the available kinetic energy is converted to electrical energy). In general, the amount of energy available to drive the circuit sensor is dependent on how efficiently the vibration is converted to electrical energy. This conversion is a function of the electromechanical coupling of the generator. Assuming no

losses in the circuit caused by unwanted leakages and nonlinearities, Equation (2.10) can be integrated to calculate the generated electrical energy.

The PZT-5H piezoelectric material properties are used in the current simulations. This material has one of the highest electromechanical coupling coefficients, thus providing a good approximation of the upper bound to the electrical power that can be harvested by commercially available piezoelectric materials.

The geometry of the sensor is assumed to be as follows. The sensor has overall dimensions of $50 \times 10 \times 10 \text{ mm}^3$ (the volume is 5 cm^3). The actual beam dimensions are: length $L = 30 \text{ mm}$, thickness $h = 0.2 \text{ mm}$, and width $b = 10 \text{ mm}$. The maximum allowable tip-deflection of the beam is constrained to 2 mm since, under larger deflections, the mechanical strains can cause the PZT to lose its piezoelectric properties. The maximum tip mass is assumed to be $M = 25 \text{ g}$, as explained in section 3.4.1 above.

For these dimensions and mass, and a PZT piezoelectric cantilever beam, the resonant frequency is approximately 7 Hz (Given by $f \approx \sqrt{Ebh^3/16\pi^2L^3M}$, where E is the elastic modulus for the piezoelectric material.). However, most civil structural dynamic loadings have extensive vibration components at around 1 Hz . Since this frequency is far from resonance, it is evident that the sensor will not be effective in converting most of the mechanical vibration to electrical energy. Although matching the dominant frequencies might be possible, by using different sensor geometry and materials, the maximum allowable tip displacements and piezoelectric failure strains would significantly constrain the magnitude of generated energy.

The generated electrical energy is calculated by solving the piezoelectric equations (Equation (2.10)) using a Runge–Kutta time-step integration routine. It has been shown

previously [48] that the extractable electric power is strongly dependent on the load resistance. The optimal load resistance to maximize the generated charge is found using the optimization algorithm given as follows:

- (1) Estimate or measure the base acceleration time history.
- (2) Set the tip mass, length, width, material and damping properties of the generator.
- (3) Choose an initial estimate for circuit resistance (R).
- (4) Calculate generator parameters K , C_m , Θ and C .
- (5) Solve for the total energy in Equation (2.10) using a numerical integration technique such as the Runge-Kutta algorithm.
- (6) Modify the resistance (R) and repeat step (4) and (5) until the energy is maximized

The results for the piezoelectric extractable energy are presented in Figure 3.7; the same loading histories and structures as in Figure 3.6 are used.

Comparing Figure 3.7 to Figure 3.6 shows that, in general, the converted energy is much lower due to weak electromechanical coupling of the piezoelectric material. The coupling is strongly dependent on the resonant frequency of the host structures and on the resonant frequency of the harvester. For example, the tall buildings analyzed here generally have resonant frequencies under 0.5 Hz. Since the energy harvester has a natural frequency of approximately 7 Hz, it is evident from the transfer function shown in Figure 3.4, that very little energy will be coupled from the structure to the harvester. This results in the extractable energy from tall buildings being approximately 10^4 times less than the maximum available energy. For earthquakes, the dominant excitation frequency ranges from as low as 0.2 Hz to as high as 10 Hz. At the higher excitation frequencies,

more energy is coupled into the harvester and thus more energy can be extracted. On average, the energy extracted from ground motion is only approximately 30 times smaller than the maximum theoretical value. For the case of bridges, the natural frequency of many medium-span bridges is around 5 Hz. Since this frequency is close to the 7 Hz resonant frequency of the harvester, which can be considered as moderate coupling; there is approximately 10 times less energy than the theoretical maximum for bridges.

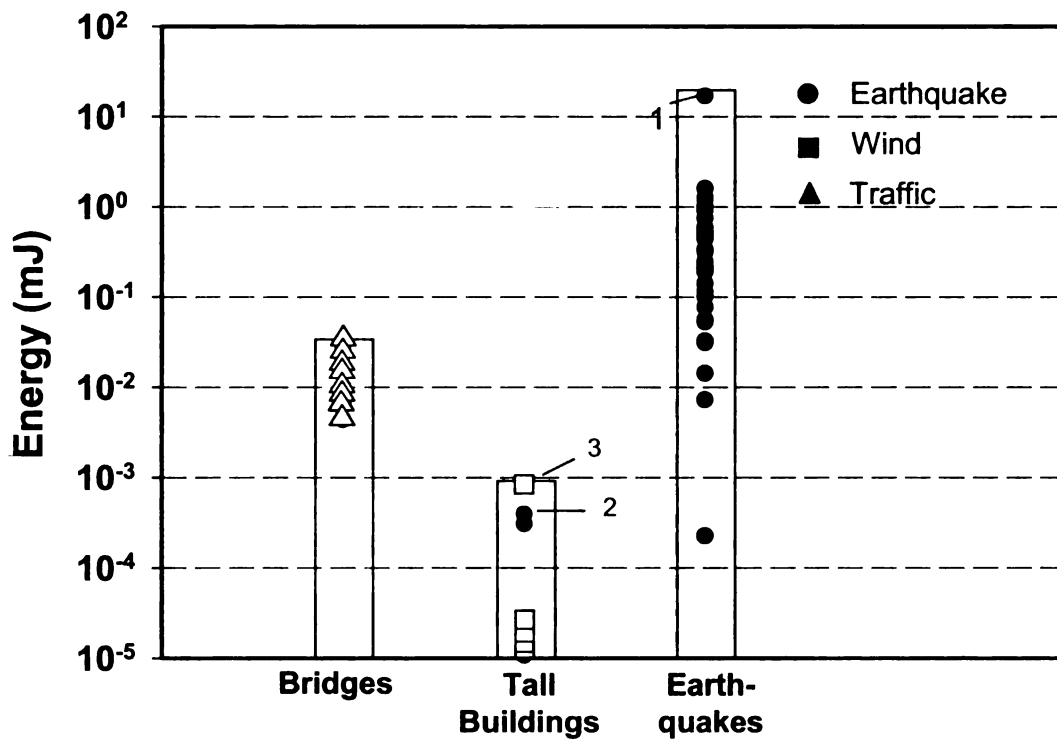


Figure 3.7 Electric energy output from a piezoelectric bimorph for various dynamic excitations

For the theoretical case (Figure 3.6), the structure loaded by earthquakes (point 2) shows larger output energy than for wind loading (point 3). The case is the reverse for the more realistic piezoelectric bimorph (Figure 3.7). This is due to the fact that the fundamental frequency of the Calgary tower (point 3) is 0.36 Hz, while for the 44 story

building (point 2) it is 0.23 Hz. This again illustrates that even small relative frequency shifts of the host structure, towards the resonant frequency of the sensor (7 Hz) can produce large changes in generated electrical energy.

3.5 ENERGY HARVESTING IN HIGH VIBRATION CIVIL ENVIRONMENTS

Typical civil engineering structures have their first fundamental natural frequency below 5Hz. Furthermore, dynamic loading such as wind, traffic and earthquakes have significant frequency components below 10 Hz. In the previous section, it was shown that under such low frequency excitation and using commercially available piezoelectric materials, it is difficult to generate more than 1 mJ of electrical power even under earthquake loading. Only very limited sensor operation can be performed with such low power levels. This section focuses on evaluating the harvestable electrical energy in some unusual high vibration civil environments.

Previous work [35, 44] has shown the feasibility of continuous circuit powering under mechanical vibration at high amplitude (greater than 0.1 g) and high frequency excitation (greater than 50 Hz). Such high frequency loading, though not typical, can be found in industrial civil engineering structures subjected to impact loading and supporting rotating and traveling machinery. The actual base excitation spectrum applied to the piezoelectric generator is then dependent on factors such as the frequency of the machinery, motor-imbalance, mounting of the machine, and the natural frequencies and damping of the support structure. In most cases the vibration magnitudes in the supporting civil structure are constrained by building design codes that include: (1) the ultimate strength of the structure, and (2) the structures' serviceability that limits distortion of the structure and

the physical discomfort of the buildings' occupants. In most cases the serviceability requirements are more limiting than the strength requirements. These requirements are dependent on the frequency and amplitude of the excitation and whether the vibration is continuous or transient. Most serviceability design standards (for example ISO-2631 [74], and AISC 11 [75]) limit the low frequency accelerations (defined to be in the 2 Hz to 10 Hz range) to between 0.05 m/s^2 and 0.1 m/s^2 depending on the duration of the vibration (Figure 3.8). Tolerable acceleration amplitudes increase with increasing frequency. In general peak acceleration amplitudes greater than 1.5 m/s^2 are considered to be extreme [76]. For many civil engineering structures, high vibration loads are often transient, and thus might not be able to provide continuous powering to electronic sensors.

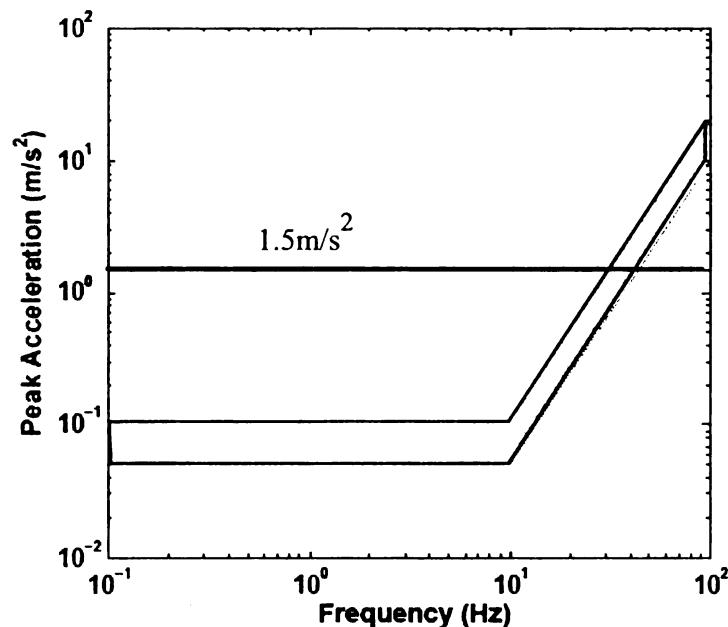


Figure 3.8 Approximate serviceability structural vibration limits (based on [74], [75] and [76]). The shaded region represents the limits based on various exposure times. The lower boundary represents longer duration vibrations; the upper boundary represents shorter duration vibrations. The solid line at 1.5 m/s^2 represents extreme vibration conditions

3.5.1 Optimal Energy Harvesting

For a given base excitation, the piezoelectric generator parameters (M , K , C_m , Θ , and C) in Equation (2.10) can be optimized to yield the maximum converted electrical energy. In general, increasing the tip mass (M), increasing the electromechanical coupling (Θ), and decreasing the mechanical damping coefficient (C_m) tends to increase the generated energy. However this optimization problem is constrained by the actual material properties, the strength and the size of the generator. Although not considered in this study, the cost of the piezoelectric material will ultimately also play an important role. In order to compare the harvested power to results in section 3.4, the size and shape of the piezoelectric material are assumed to be the same as in section 3.4. The generator size fits into a 5 cm^3 volume, while allowing space for the electronic circuitry and generator displacement under dynamic loading. The generator material is assumed to be PZT-5H which gives the highest electromechanical coupling coefficient of commercially available piezoelectric materials. The mechanical damping is assumed to be 4% of critical.

Under the given constraints, this optimization problem has two free parameters. The first free parameter is the height of the beam (h) which affects: the beam stiffness (K), generator capacitance (C) and electromechanical coupling coefficient (Θ). The second free parameter is the impedance of the sensor, which influences the current (I) drawn by the circuit. For example, for a purely resistive load (R), the current drawn is given by $I = v/R$. The optimal energy is determined using the same optimization procedure as in section 3.4.3.

As previously mentioned, a myriad of factors influence the harvester's base acceleration and thus the input excitation might be difficult to estimate a priori. The vibration history might change under different operating conditions. Furthermore, the structural and machine properties could change with time because of damage and wear. It is thus advisable to optimize the performance of the generator with various estimated or measured inputs.

3.5.2 Example

To demonstrate both the optimization algorithm and to estimate the amount of convertible energy in a high vibration civil industrial environment, the support beam under an overhead crane is investigated in this study.

This structure consists of a continuous steel I-beam, (height: 252mm, width: 115mm, flange thickness: 13mm, and web thickness: 8mm) supporting a 3 ton crane (Figure 3.9).

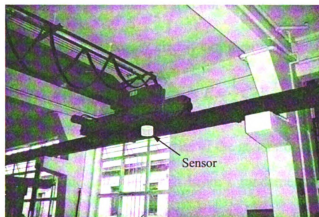


Figure 3.9 Investigated structure consisting of a steel I-beam with an overhead moving crane. Position of accelerometer node is as shown

The crane can operate at two speeds (0.8 m/s and 0.3 m/s). The accelerations at mid-span of the supporting beam (span 4.8m) was measured using a wireless, custom-built,

lightweight data recorder (ZeroPoint Technology, Johannesburg, South Africa) at a sampling rate of 2000 Hz. The accelerometer in the ZeroPoint device was a 3 axis accelerometer (ADXL330, Analog Devices Inc., Norwood, MA). Throughout this experiment, all accelerations are measured by this device.

A typical time history and associated frequency spectrum for the acceleration at the mid-span of the beam is shown in Figure 3.10. The crane is started and stopped at the midpoints of the adjacent beam spans. The time history and frequency spectrum shows the transient nature of the excitation (lasting approximately 15 seconds), with a very wide excitation frequency bandwidth (0 to 200 Hz).

3.5.3 Optimal Energy Harvesting Results

In many cases it is not possible to match the impedance of the circuit to the ambient vibration. Further, the generated energy is often stored for future use. In one such circuit, the converted voltage (V_s) is stored onto a capacitor (C_s) through a full diode bridge as discussed in section 2.3.2.3. The sensor circuit can then be represented by a drainage resistor (R_d). In this case, the generated energy is $E = \frac{1}{2} C_s V_s^2$.

Assuming the material and geometry properties of the generator shown in Table 3.3, the maximum energy can be calculated for each beam's fundamental resonant frequency using the optimal resistance. The result of this optimization for the over-head crane moving from left to right at its higher speed is shown in Figure 3.11. Three separate crane base accelerations were used for the resistive circuit simulation showing good consistency from case to case. The mechanical natural frequency of the generator can be

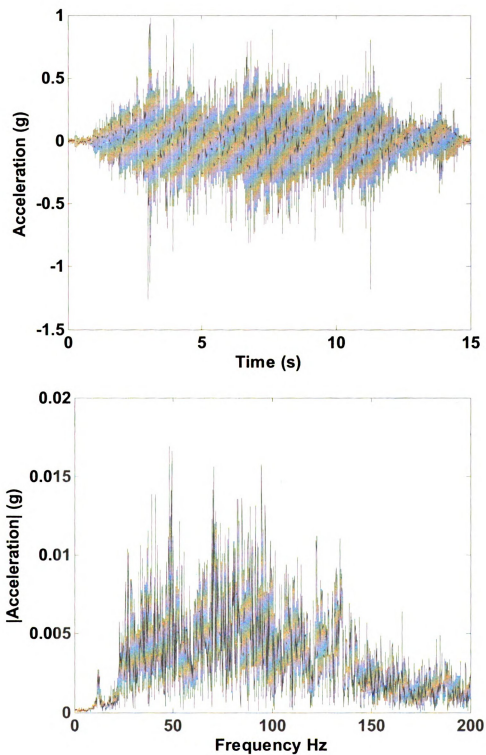


Figure 3.10 A typical input acceleration time history and the associated frequency spectrum for a lightweight crane moving at 0.8 m/s, measured at mid-span on the supporting beam

Table 3.3 Piezoelectric and Circuit Sensor Properties

Piezoelectric (PZT-5H) Properties	
Modulus of Elasticity	$c_p=63 \text{ GPa}$
Permittivity	$\epsilon=1.21 \times 10^{-8} \text{ F/m}$
Piezoelectric coupling coefficient	$e=11.3 \text{ C/m}^2$
Piezoelectric Density	$\rho=7500 \text{ kg/m}^3$
Tip Mass	$M_{tip}=25 \text{ g}$
Length	$L=30 \text{ mm}$
Width	$b=10 \text{ mm}$
Damping coefficient	$\zeta=4\%$
Circuit Elements	
Diodes	1N4148
Storage Capacitor	$C_s=3.3 \text{ }\mu\text{F}$
Drainage Resistor	$R_d=10 \text{ M}\Omega$

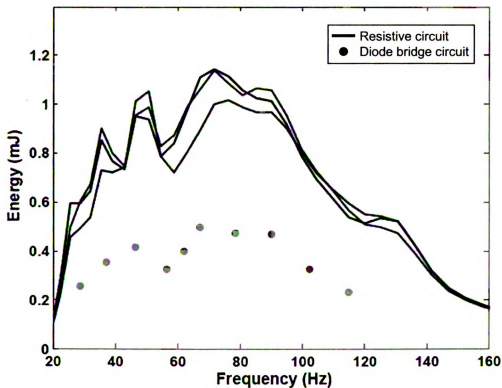


Figure 3.11 Maximum extractable electrical energy for a resistive circuit (solid lines) and diode-bridge circuit (circles), for the crane moving from left to right at 0.8m/s. The three solid lines represent acceleration histories from three different crane runs

related approximately to the generator's height, h , using a Rayleigh-Ritz approach by:

$$f \approx \frac{\pi h}{L} \sqrt{\frac{Ehb}{1536ML}} \quad (3.2)$$

The maximum resistive energy that can be extracted from the crane is approximately 1.17mJ when the vibrator's mechanical natural frequency is 76Hz, corresponding to $h = 0.99\text{mm}$. The maximum diode-bridge energy that can be extracted is approximately 0.5mJ when the vibrator's natural frequency is 68Hz, corresponding to $h = 0.92\text{mm}$. These values are approximately the same when the crane moves in the opposite direction (right to left), with the maximum extractable energy being 10% less than the left to right case.

3.6 DISCUSSION

Good electromechanical coupling between the host structure and sensor is critical for maximum electrical power conversion. For example, the commonly used El Centro earthquake generates approximately 0.5 μJ from a PVDF unimorph generator. Using a PZT generator would produce approximately 1.2 mJ. In comparison, an electric generator, as described in section 3.4.1, with perfect coupling would produce 13.9 mJ.

Sensor nodes need energy to wake up and start collecting and transmitting—this was not considered in this study. The energy levels for sensor start-up are of the order of 10 μJ [77]. Therefore, using today's integrated circuits, 10 μJ is the absolute minimum energy required to be converted from structural vibrations for the sensor node to even switch on. Thus, for PVDF generators scavenging vibration energy on civil structures subject to the

El Centro earthquake, no useful electronic sensor functions can be performed. For a PZT-based generator, approximately 5000 data bits could be transmitted, compared to 70 000 bits if perfect electromechanical coupling is realized. Choosing a greater tip mass in a piezoelectric generator could increase the power harvested. This increase is achieved by:

- (a) Directly increasing the kinetic energy (as shown in Equation (2.10)), and
- (b) Reducing the resonant frequency of the beam to more closely match the spectral energy content of the loading.

However, increasing the tip mass would also increase the maximum tip deflection, and the maximum strain in the beam. As discussed above, this might overload the beam, resulting in a significant reduction or loss of piezoelectric properties.

The effect of changing the resonant frequency of the beam to match the spectral energy of the input loading is shown in Figure 3.12 for the El Centro earthquake. By increasing the length and decreasing the width of the bimorph shown in Figure 2.4 and described in section 3.4.3, it is possible to decrease the resonant frequency of the beam without changing the volume of the sensor. Figure 3.12 shows the significant increase in harvested energy for the El Centro earthquake with better frequency matching. As mentioned previously, the maximum theoretical harvestable energy for the El Centro earthquake is 13.9 mJ. Figure 3.12 shows that the optimal resonant frequency of the PZT generator is between 1.5 and 2 Hz. This closely matches the dominant frequency range for the El Centro earthquake, as shown in Figure 3.3(b). However, the energy numbers in Figure 3.12 are theoretical since for a real PZT bimorph the very large deflections (and strains) at the matched frequency (i.e. 1.5–2 Hz) could lead to sensor damage.

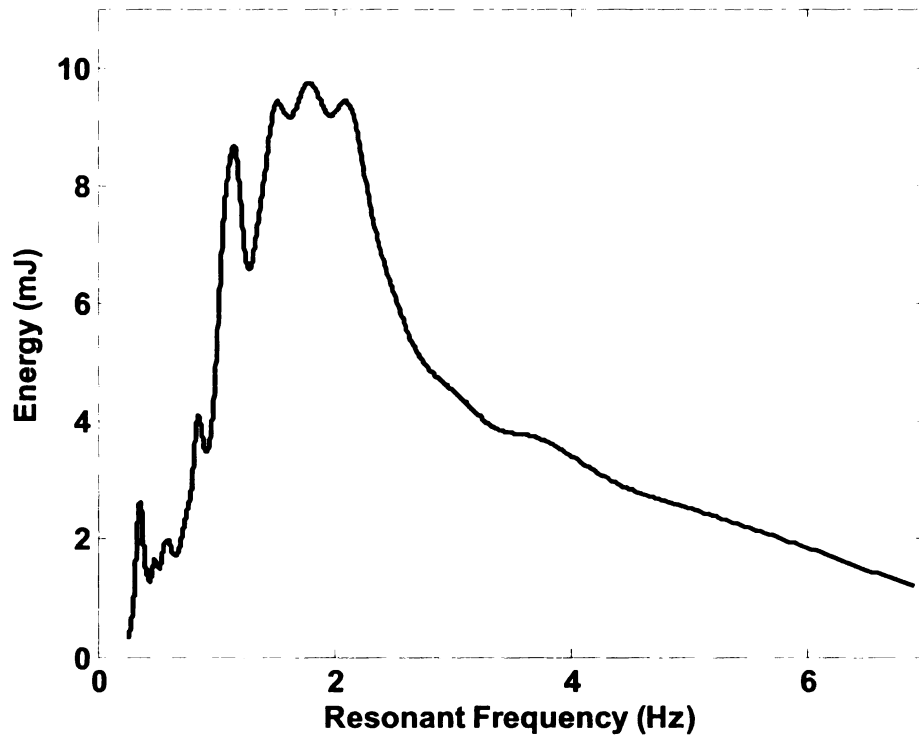


Figure 3.12 Generated electrical energy from the El Centro earthquake for a bimorph PZT with various resonant frequencies

Figure 3.13 shows the maximum theoretical energy that can be generated by a range of traffic loading on a concrete bridge with increasing tip mass (data from [67]). The shading in Figure 3.13 corresponds to the range of dynamic loading from heavy and light traffic loads. The average curve corresponds to the average generated energy from all traffic loading. The generated energy scales approximately linearly with mass. As shown from the piezoelectric analysis, the maximum convertible energy is of the order of 10 to 100 times less than the theoretical maximum. Assuming that $50 \mu\text{J}$ is required for a significant data transmission ($10 \mu\text{J}$ for circuit start-up, $20 \mu\text{J}$ for data transmission, $10 \mu\text{J}$ for sensor operation, and $10 \mu\text{J}$ for microcontroller energy), a mass of 100–1000 g is needed for adequate circuit powering under average traffic loading. Under the same mass

density for the sensor as used in section 3.4.2, this would correspond to a volume between 20 and 200 cm³. For applications where the generator is embedded in the structure, this volume might be too large, thus creating problems: (a) in manufacturing the structure and effectively embedding the node, and (b) by weakening the structure at the location of the node.

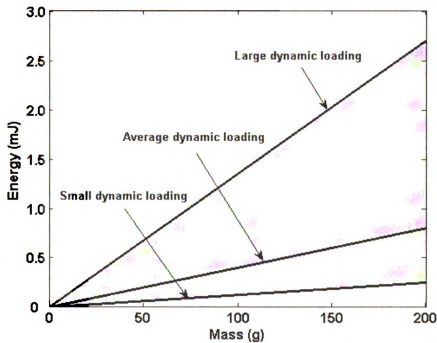


Figure 3.13 Generated electrical energy for various traffic loadings on a concrete bridge, assuming perfect electro-mechanical conversion

For the high vibration environment considered (i.e., a moving crane), the optimization shows that a 5 cm³ piezoelectric generator can convert approximately 1.2 mJ of electrical energy from a single 0.8 m/s crane run. The magnitude of the generated energy is similar to the optimum energy that can be extracted from a mid to large size earthquake. Under continuous crane movement (backwards and forwards at maximum speed) the average power that can be harvested is 125 μ W. This amount is eight times less than the energy

required to operate a basic sensor node continuously. This sensor node would consist of an efficient commercial microprocessor, data acquisition system, and wireless transmission link (section 3.2). As previously discussed, the generated electrical energy scales approximately linearly with generator volume (Figure 3.13). Thus an optimally designed 40 cm^3 generator could continuously power a wireless sensor node today. With the rapid advances in wireless sensor nodes, it is likely that the 1 mW power level will be achieved in commercial electronics components within a few years. Thus the use of piezoelectric power harvesters as energy sources for sensor nodes in high vibration environments can be expected in the near future.

One important note is that the overall vibration environment of the piezoelectric generator could change both in magnitude and frequency throughout the lifetime of the building. For example, the vibration under a crane load can be influenced by the quality and alignment of the supporting rail, the balance of the wheels, the speed of the crane, and the stiffness of the supporting structure. To prevent de-tuning, a good piezoelectric generator design should take into account the possible changes in the input accelerations throughout the lifetime of the structure. For example, changing support conditions throughout the life of the structure could lead to de-tuning of the harvester. For a single dominant base excitation frequency and for a simple sensor circuit (such as a purely resistive load), the de-tuning effect can be readily calculated [52, 78] as shown in Figure 3.12. However for a relatively wide-spectrum excitation (such as is common in civil engineering structures), the effect of changing structural support conditions on energy harvesting has not been investigated adequately. The performance of different harvesting

circuits under these changing conditions also needs to be considered. Future research should focus on quantifying the de-tuning effect.

3.7 CONCLUSION

This chapter set out to answer the following question. Can power harvesters based on vibration energy be used to power wireless sensors and sensor networks? It was found that, assuming perfect electromechanical coupling (the results shown in Figure 3.6), vibration harvesters can produce in the range of 1 mJ. (This range ignores extreme earthquake events, which can produce significantly more energy). This amount of energy can power a basic wireless sensor; approximately 500 bytes of information can be transmitted.

Realistically however, when imperfect electromechanical coupling is taken into account, power harvester's efficiency can be reduced by as much as 100 times (See Figure 3.7 for results). Assuming a 5 cm³ sensor node, the 10 μ J of energy converted from average dynamic events such as wind, traffic and low-scale earthquakes, is insufficient to run modern wireless sensors.

Piezoelectric-based vibration harvesters do produce enough energy from large-scale earthquakes and high vibration environments; these events can allow for approximately 500 data samples to be collected and wirelessly transmitted by a sensor node.

The wake-up energy of a wireless sensor is on the order of 10 μ J [77]. Thus, for most typical dynamic events, it would be impossible to harvest enough energy to power a 5 cm³ wireless sensor. Self-powered wireless sensor communication could become more feasible if this start-up energy barrier is reduced.

Increasing the mass (and thus volume) of the energy converter will increase the maximum power generation. This work shows that, with a circuit energy consumption of approximately $50\mu\text{J}$, the volume of a realistic energy generator would be between 20 and 200 cm^3 . The actual volume will depend on the available kinetic energy and the electromechanical coupling between the generator and the vibrating structure.

Current research is striving to reduce sensor node power consumption to the picojoule range [36]. If this is achieved, then small wireless sensor nodes could process and transmit data even for very low-energy wind loading on tall structures. However, even if the sensor electronic power consumption is reduced, significant effort would still be needed to reduce losses during the energy conversion process. Examples where such losses occur are voltage rectification, and capacitor and resistor leakages.

Lastly, it should be noted that there are several practical considerations in energy-converter design. The fracture resistance of the piezoelectric ceramic, the loss of the piezoelectric properties, and the maximum deflection under dynamic loading could all play major roles in reducing the overall power generation capacity of electromechanical energy harvesters.

CHAPTER 4

SUB-MICROWATT PIEZO-POWERED ANALOG CIRCUITS: MODELING AND ANALYSIS

4.1 INTRODUCTION

The previous chapters discussed some of the limitations of self-powering using piezoelectric transduction. Even though the transducer can generate a large open load voltage (> 15 V), its capacitive nature (see Figure 4.6) limits the total current that can be delivered to its electrical load. Typically this current is in the order of nanoamperes for a loading cycle of 1 Hz or less (section 2.3.2).

The properties of the piezoelectric transducer, however, are attractive for operating analog floating-gate circuits that typically require high voltage and very low current for programming. A floating gate is a poly-silicon gate surrounded by an insulator, which in the standard semiconductor fabrication process is silicondioxide [43, 79]. Because a floating gate is surrounded by high-quality insulation, any electrical charge injected onto this gate is retained for long intervals of time (> 8 years). The basic principle behind the integrated piezoelectric floating-gate sensor is illustrated in Figure 4.1, in which the floating gate is coupled to a p-channel metaloxide-semiconductor (pMOS) transistor. The electrical energy produced by the piezoelectric transducer is used to inject electrons from the transistor channel onto the floating gate. The repeated accumulation of charge on the floating gate is indicative of the history of mechanical loading and therefore can be used as an integrated platform for sensing, computation, and storage in structural monitoring applications. The following sections present an overview of the developed structural monitoring micro-system based on floating-gate VLSI circuits.

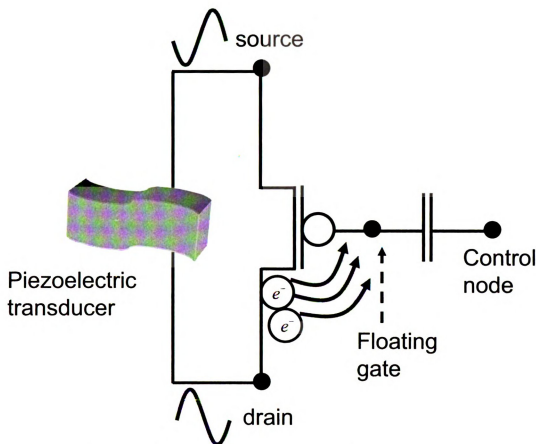


Figure 4.1 Principle of the piezo-powered floating-gate sensor

4.2 FLOATING GATE TRANSISTORS

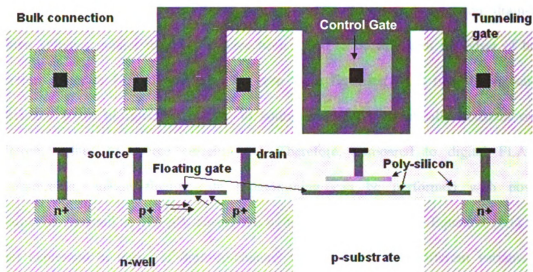
In a standard CMOS process, a floating gate is a poly-silicon gate surrounded by silicon-dioxide that acts as insulator. When the floating gate is coupled to a gate of a transistor, as shown in Figure 4.2(a), the cumulative charge stored on the floating gate can be sensed by measuring the transistor's drain current.

The charge on the gate can be modified using either hot electron injection or using tunneling [79]. Hot electron injection in a pMOS transistor occurs when a high-electric field is formed at the drain-to-channel depletion region. Due to this high-electric field, the holes gain significant energy to dislodge electrons by hot-hole impact ionization. The

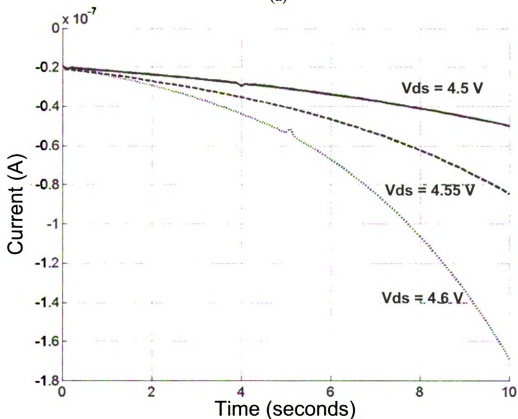
released electrons travel back into the channel region, gaining energy and when their kinetic energy exceeds the silicon and silicon-dioxide (> 3.2 eV) barrier, the electrons are injected into the oxide. As more electrons are added to the floating gate, its potential decreases, which results in an equivalent increase in the drain current through the transistor. Hot-electron injection in a pMOS transistor is a feedback process because an increase in injection onto the floating gate (decrease in gate potential) reinforces the injection process. Thus injection is required to be carefully controlled to be able to perform any useful and sustained computation. Empirically, the injection current has been found to be proportional to the source current through the pMOS cell and drain-to-channel (source) potential and can be expressed as:

$$I_{inj} = I_S e^{f(V_{dc})} \quad (4.1)$$

where $f(V_{dc})$ is a smooth function of drain-to-channel potential V_{dc} and I_S is the source current through the pMOS transistor. Figure 4.2(b) shows measured injection characteristics of a pMOS floating-gate transistor when the source-to-drain terminal is subjected to 1 second pulses of varying voltage amplitude. For each excitation pulse, the pMOS transistor injects a packet of charge on the floating gate that results in an increase in the drain current. Subsequently, a larger packet of charge is injected per pulse as evident from Figure 4.2(b) reiterating the positive feedback nature of pMOS injection. This mechanism has been used by several researchers [43, 79, 80] to accelerate programming of the floating gate to a pre-determined voltage. It has also been demonstrated that the injection current is practically independent of the floating-gate-to-channel potential, as long as the gate potential is greater than the drain potential, which is naturally satisfied for pMOS transistors operating in weak-inversion [43]. For a pMOS tr-



(a)



(b)

Figure 4.2 (a) Top and cross-sectional view of a floating-gate transistor and (b) the measured drain current when injection pulses of different amplitude are repeatedly applied across the drain-source terminal

ansistor fabricated in a 0.5 μ m CMOS process and biased in weak-inversion, drain-to-source voltages greater than 4.2 V have been found to be sufficient for onset of hot-electron injection [43]. It can also be seen from Equation (4.1) that the injection efficiency (ratio of injection current to source current) is practically constant over different values of source current [43]. Therefore, compared to digital FLASH programming, analog floating-gate programming can be performed with power dissipation as small as 100 pW during the write cycle. Even though Equation (4.1) has been expressed in terms of drain-to-channel potential [81, 82], different variants of Equation (4.1) have been proposed that employ measurable potentials that are the drain, source, and gate potentials. In this study, it was found that a simplified empirical model is sufficient for injection-based circuits and it is expressed as:

$$I_{inj} \approx \beta I_S e^{\frac{V_{sd}}{V_{inj}}} \quad (4.2)$$

with β and V_{inj} are bias-dependent parameters. Hot-electron injection is typically a one-way process in which electrons can be added to the floating gate.

Removal of electrons from the floating gate can be achieved either through exposure to ultraviolet (UV) radiation or by use of tunneling. Tunneling is a quantum mechanical phenomenon whereby the electrons, instead of surmounting an energy barrier, propagate through it. A tunneling capacitor as shown in Figure 4.2(a) is coupled to the floating gate and a large potential is applied to initiate tunneling. The magnitude of the tunneling current has been empirically determined as:

$$I_{tun} \approx -I_{tun0} e^{-\frac{V_f}{V_{ox}}} \quad (4.3)$$

where I_{tun0} is a pre-exponential current, V_{ox} is the voltage across the oxide and V_f is a constant that depends on the oxide thickness. In addition to the tunneling capacitor, the floating gate is capacitively coupled to other terminals. A model of a pMOS floating-gate transistor with capacitive elements is shown in Figure 4.3.

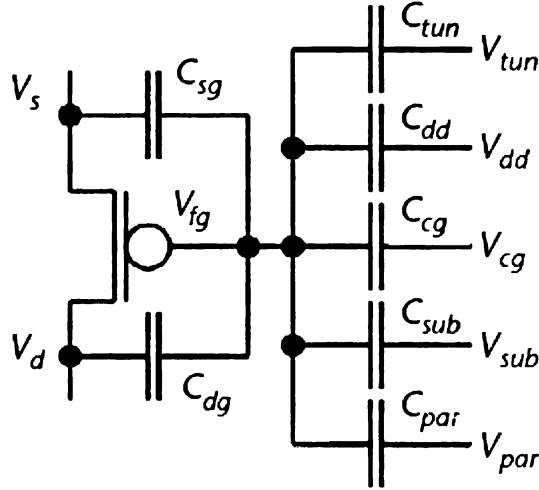


Figure 4.3 Capacitive model of a pMOS floating-gate transistor

The control gate capacitance C_{cg} serves as the dominant capacitance and is used for modulating the drain-to-source current. The tunneling capacitor in Figure 4.3 is denoted by C_{tun} , the parasitic capacitance between the supply voltage and substrate is denoted by C_{dd} and C_{sub} respectively and the overlap capacitance between the floating gate to the drain and source terminal is denoted by C_{dg} and C_{sg} . The auxiliary parasitic capacitance to the neighboring buses is denoted by a lumped capacitance C_{par} . All these capacitors play key roles in achieving uniform and matched injection response in an array of floating-gate transistors. Based on the circuit model in Figure 4.3, the voltage on the floating gate V_{fg} can be expressed as:

$$V_{fg} = \frac{Q_{fg} + C_{cg}V_{cg} + C_{dd}V_{dd} + C_{sub}V_{sub} + C_{par}V_{par} + C_{dg}V_d + C_sV_s}{C_T} \quad (4.4)$$

where $C_T = C_{cg} + C_{dd} + C_{sub} + C_{par} + C_{dg} + C_s$ and Q_{fg} is the residual charge on the floating gate modulated by injection and tunneling. The source-to-drain current through the pMOS transistor when biased in weak-inversion can then be expressed in terms of the floating-gate voltage V_{fg} , drain voltage V_d and source voltage V_s as:

$$I_{ds} = I_o \frac{W}{L} \exp(-\kappa \frac{V_{fg}}{U_T}) \left[\exp(\frac{V_s}{U_T}) - \exp(\frac{V_d}{U_T}) \right] \quad (4.5)$$

where W and L are the width and length of the transistors, κ is the floating gate efficiency, I_o is the specific current and U_T is the thermal voltage (26mV at room temperature). For $V_{sd} > 3U_T$, Equation (4.5) simplifies to

$$I_{ds} = I_o \frac{W}{L} \exp(-\kappa \frac{V_{fg}}{U_T}) \exp(\frac{V_s}{U_T}) \quad (4.6)$$

which is the saturated mode of operation for the pMOS transistor biased in weak-inversion.

4.3 FLOATING-GATE INJECTOR AND ITS MATHEMATICAL MODEL

The schematic of a single-channel piezo-powered floating-gate sensor is shown in Figure 4.4. The injection rate of the floating gate transistor Q_1 can be controlled by limiting the source current in Equation (4.2) using a constant current reference I_b . Also, as shown in section 4.5, the drain-to-source voltage can be controlled by inserting diodes between the current reference and the floating-gate transistor. Let V_g denote the voltage of the floating gate at a fixed control gate bias voltage V_B . The total floating gate

capacitance is given by C_T according to Equation (4.4). The current reference biases the floating transistor in weak-inversion satisfying the following relationship:

$$I_b = I_o \frac{W}{L} \exp\left(-\kappa \frac{V_g}{U_T}\right) \exp\left(\frac{V_{out}}{U_T}\right) \quad (4.7)$$

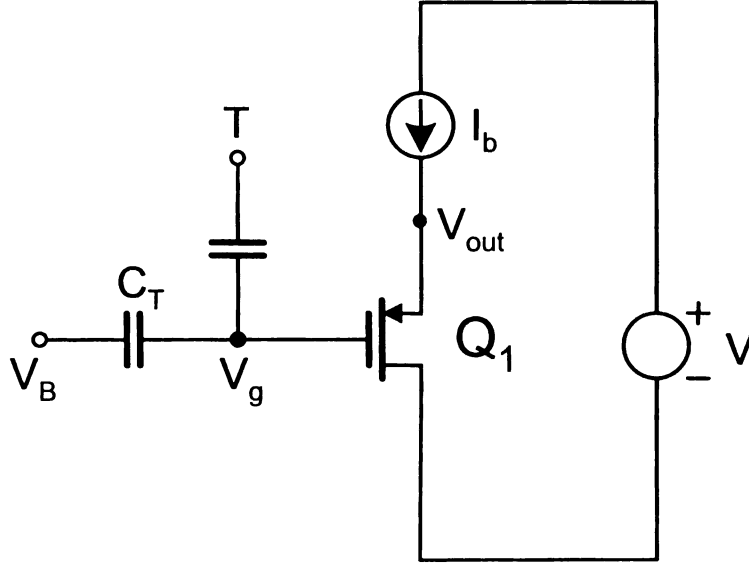


Figure 4.4 Simplified circuit model for piezo-driven floating-gate sensor [83]

Provided that conditions are suitable for hot-electron injection (high-electric field at the drain-to-channel region), the injection current charges the floating gate capacitor according to:

$$I_{inj} = -C_T \frac{dV_g}{dt} = \beta I_b \exp\left(\frac{V_{out}}{V_{inj}}\right) \quad (4.8)$$

where Equation (4.2) was used.

Eliminating the variable V_{out} using Equations (4.7) and (4.8), the first-order differential equation is obtained in terms of the gate voltage V_g :

$$C_T \frac{dV_g}{dt} = -\beta \frac{(I_b)^{1+\frac{U_T}{V_{inj}}}}{(I_o \frac{W}{L})^{\frac{U_T}{V_{inj}}}} \exp\left(\kappa \frac{V_g}{V_{inj}}\right) \quad (4.9)$$

which is written in its closed form as:

$$V_g(t) = -\frac{1}{K_2} \log \left(K_1 K_2 \int_{\tau \in t} d\tau + \exp(-K_2 V_{g0}) \right) \quad (4.10)$$

with the values of K_1 and K_2 given by

$$K_1 = \left(\frac{\beta I_b}{C_T} \right) \left(\frac{I_b W}{I_o L} \right)^{\frac{U_T}{V_{inj}}}$$

$$K_2 = \frac{\kappa}{V_{inj}}$$

V_{g0} in Equation (4.10) is the initial floating-gate voltage and t denotes the total duration during which the injector circuit in Figure 4.4 is operational. The output voltage $V_{out}(t)$ can also be expressed in terms of $V_g(t)$ as:

$$V_{out}(t) = V_g(t) + K_3 \quad (4.11)$$

with $K_3 = U_T \log(I_b/I_o)$.

Figure 4.5 shows a typical response of the output voltage $V_{out}(t)$ as a function of injection duration t . The response as shown in Figure 4.5 consists of two distinct regions. The linear region which is characterized by the condition $t \ll (1/K_1 K_2) \exp(-K_2 V_{g0})$ and by using Equation (4.11) can be simplified to:

$$V_{out}(t) = V_{g0} + K_3 - \frac{K_1 K_2}{\exp(-K_2 V_{g0})} t \quad (4.12)$$

where the approximation $\log(1+x) \approx x$ has been used. Thus in the linear region, the change in the output voltage is linear with respect to the injection duration and therefore is

suitable for short-term fatigue monitoring (typically less than 100 loading cycles). The other region, which is particularly important for long-term monitoring, is the log-linear region and is characterized by the condition $t \gg (1/K_1 K_2) \exp(-K_2 V_{g0})$, which when applied to Equation (4.11) leads to:

$$V_{out}(t) = K_3 - \frac{1}{K_2} \log(K_1 K_2) - \frac{1}{K_2} \log(t) \quad (4.13)$$

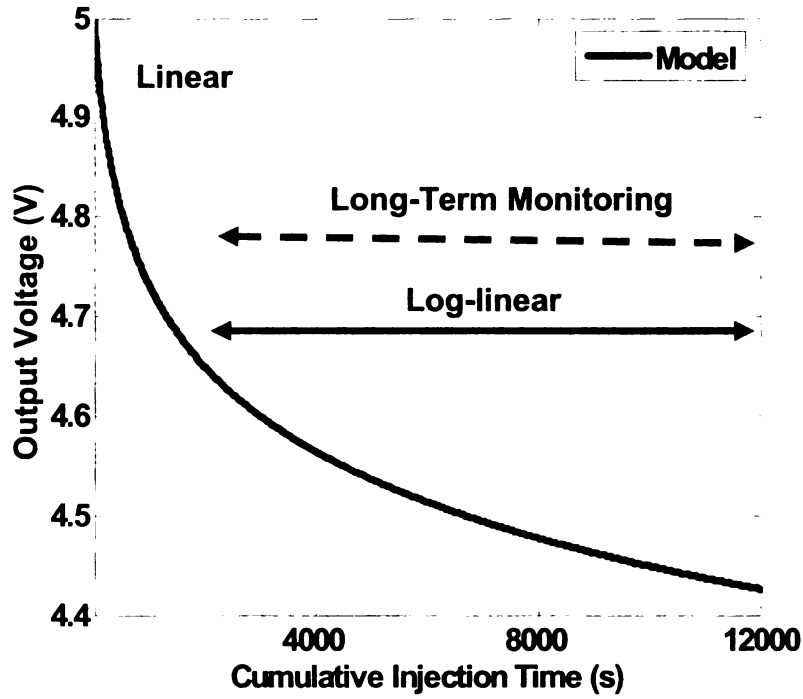


Figure 4.5 Response of a floating-gate injector based on the mathematical model in Equation 4.10

Thus, the change in output voltage is a logarithmic function of time and could be used for long-term event monitoring. The first part in Equation (4.13) is an offset term that captures the dependence of the output voltage on the biasing conditions, initial conditions, and ambient temperature.

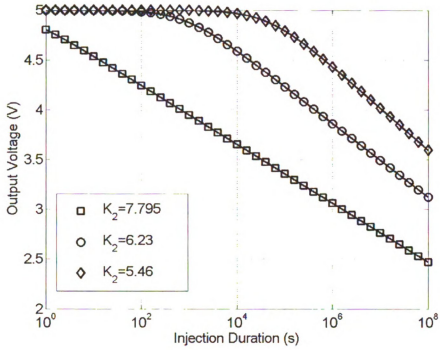
Figures 4.6(a) and (b) show the output voltage $V_{out}(t)$ response plotted on a logarithmic scale for typical values of parameters K_1, K_2 . It can be seen from Figure 4.6(a) that the slope of the log-linear response is a function of K_2 and hence determines the maximum monitoring duration. Using typical parameters obtained from a 0.5 μm CMOS process, we have verified that “log-linear” response can easily last beyond a million injection seconds. The parameter K_1 , which is a function of the ambient conditions, only introduces an offset in the log-linear response. This principle will be important in compensating the response of the injector for initialization errors that can be seen when Equation (4.13) is expressed in its incremental form as:

$$\Delta V_{out}(t) = -\frac{1}{K_2} \log\left(\frac{t}{t_0}\right) \quad (4.14)$$

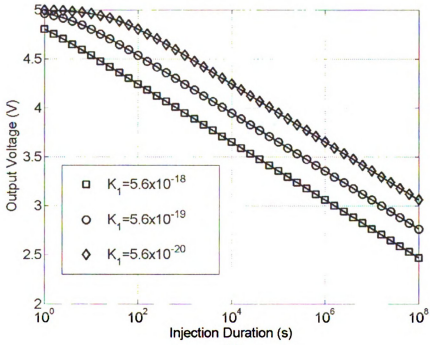
where $\Delta V_{out}(t)$ is the change in voltage measured with respect to voltage at reference time-instant t_0 . Details related to calibration will be discussed in section 5.3.3 of chapter 5.

4.4 CMOS CURRENT REFERENCES

The current reference in the schematic shown in Figure 4.4 is important for ensuring stable floating-gate injection. The reference therefore has to establish a bias current that is insensitive to the voltage fluctuation at the output of the piezoelectric transducer. Also the reference should be robust to variations in process and ambient conditions (for example temperature). In the literature most current references fall into either one of the following categories: (a) references whose output is proportional to absolute temperature (PTAT); (b) references whose output is temperature independent. In this section, the principles be-



(a)



(b)

Figure 4.6 Response of the floating-gate injector for different values of (a) parameter K_2 and (b) parameter K_1

hind the design of a CMOS PTAT current reference are discussed, and then some of its performance limitations are illustrated [84, 85, 86].

Figure 4.7 shows a schematic of a basic current reference, that was first proposed using bipolar transistors [87], and later in its CMOS form [88].

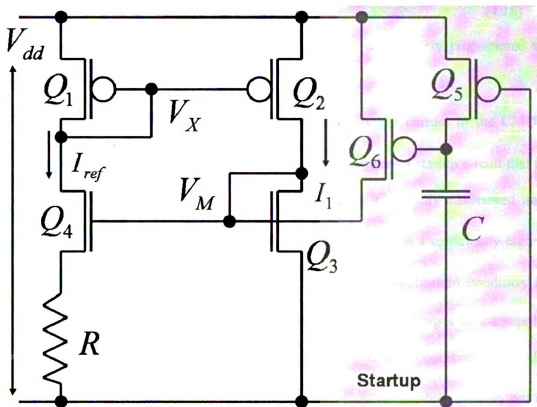


Figure 4.7 Schematic of a CMOS current reference

If the width-to-length ratio W/L of transistors Q_1 and Q_2 is denoted by W_1/L_1 and W_2/L_2 , then I_{ref} is given by:

$$I_{ref} = KI_2 \quad (4.15)$$

with $K = W_1L_2/L_1W_2$.

The current I_{ref} determines the potential drop across the resistor R , which in turn determines the ratio of the currents flowing through the nMOS transistors Q_5 and Q_6 . If the transistors are biased in weak-inversion, the current I_{ref} can be calculated as:

$$I_{ref} = \frac{U_T}{R} \log K \quad (4.16)$$

which is theoretically independent of the supply voltage and linearly proportional to temperature through U_T .

It can be verified that $I_{ref} = 0$ is also a stable state for the current in the CMOS reference circuit. The schematic in Figure 4.7, therefore, requires a startup circuit that is formed by transistors Q_5 and Q_6 . Initially the capacitor C is fully discharged and therefore Q_5 and Q_6 are ON. This ensures that the node V_M is at a sufficiently higher potential than the source of Q_4 during startup. When the equilibrium condition is achieved as determined by the Equation (4.16), the capacitor C charges to the supply voltage, which then turns off the transistors Q_5 and Q_6 . Under ideal conditions (perfectly matched transistors), I_{ref} does not depend on supply voltage or threshold voltage, but is monotonic in temperature (approximately PTAT in weak inversion). In practice, the reference is affected by the supply voltage variation due to finite drain-to-source impedance of transistor Q_2 , and also by threshold voltage mismatch between the pMOS pair Q_1, Q_2 and nMOS pair Q_3, Q_4 . The sensitivity of the current reference to the supply voltage variations can be reduced by either using long transistors and through cascading. Stability of the current reference is another design consideration that is important during

its start up. By limiting the total capacitance at node V_M , limit-cycle behavior can be avoided.

4.5 DESIGN OF A COMPLETE FLOATING-GATE SENSOR ARRAY

In this section, a complete design of an array of floating-gate injectors is described. The basic sensor circuit given in Figure 4.4 has been extended to an array by inserting MOS diodes between the current reference and the source of the floating gate transistor. A schematic implementing a complete floating-gate injector array with an integrated current reference is shown in Figure 4.8. Table 4.1 provides the respective sizes of the transistors, resistors, and capacitors used for this prototype. Seven injectors have been integrated on the chip.

A reference current generator circuit is implemented using transistors $M_1 - M_8$ and a resistor R . If the ratio of the pMOS current mirror transistors M_1, M_5 is denoted by K , then the magnitude of the reference current is $I_b = (U_T / R) \log K$, where U_T denotes a thermal voltage (26 mV at room temperature). Transistors S_1 and S_2 form a startup circuit for the current reference. The reference current is copied by mirrors $P_1 - P_{13}$, which drive the floating-gate cells F1–F7. Diode-connected transistors arrays D1–D6, are used to control the potential drop between the supply terminal and source of the floating-gate transistors, this ensures that each of the floating-gate cells (F1–F7) start injecting at a differential supply potential ($V^+ - V^-$). For an injector circuit consisting of M diodes between the current source and the floating-gate transistor, the minimum supply voltage required for onset of injection is:

$$V^+ - 2V_{dsat} - MU_T \log\left(\frac{I_b}{I_{d0}}\right) - V_{out_i} = V^- \quad (4.17)$$

where V_{dsat} is the drain-to-source voltage drop for the cascaded current mirrors, I_{d0} is specific current for the pMOS diode transistors, and V_{out_i} is the initial floating-gate source voltage for nodes $O_i, i = 1, \dots, 8$.

For transistors biased in weak-inversion $V_{dsat} \geq 3U_T$, which leads to:

$$V^+ - V^- \geq MU_T \log\left(\frac{I_b}{I_{d0}}\right) + V_{out0} + 6U_T \quad (4.18)$$

For $V_{out0} = 5V$, the inequality (4.18) leads to:

$$V^+ - V^- \geq 0.6M + 5.15 \quad (4.19)$$

Therefore the minimum amplitude of voltage pulses required to be generated by the piezoelectric transducer is 5.15 V.

Table 4.1 Component sizes used in circuit in Figure 4.10

Component	Parameter
M1	60 μm /10 μm
M2, M5-M6, P1-P16	30 μm /10 μm
M3-M4, M7-M8	60 μm /10 μm
D1-D7	10 μm /10 μm
F1-F8	6 μm /6 μm
C1-C8	100fF
R	1.5M Ω

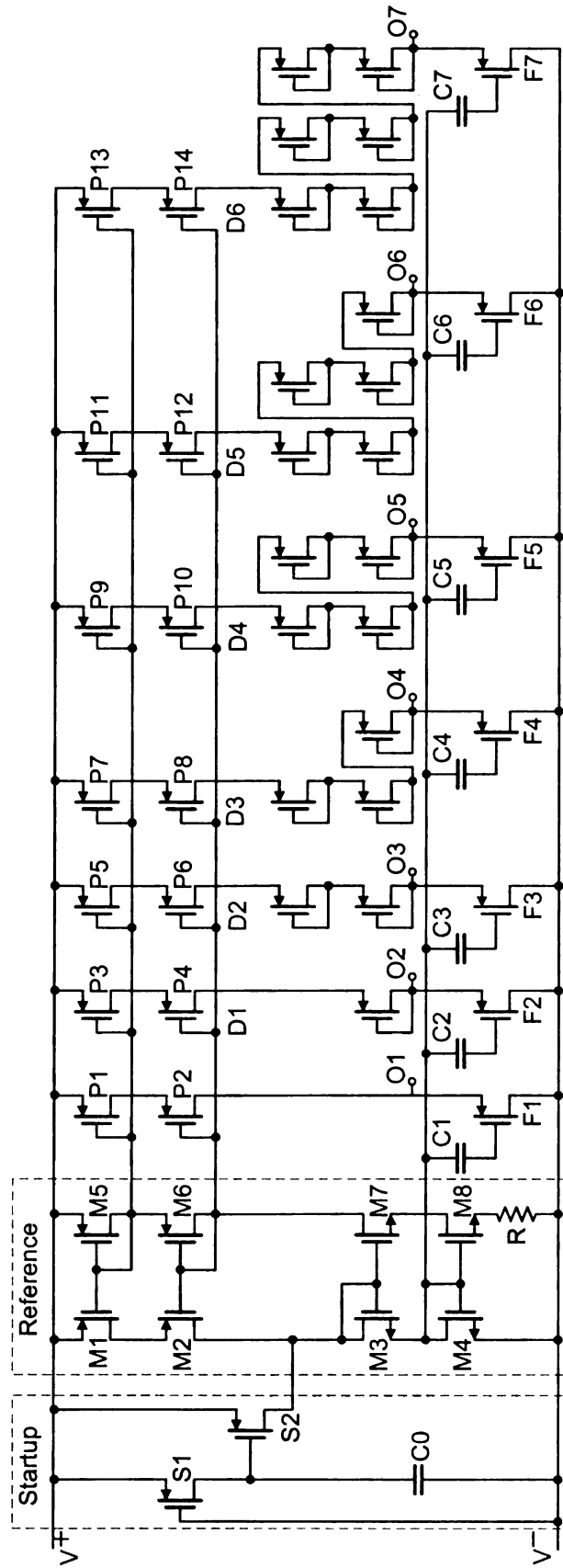


Figure 4.8 Floating-gate reference array

Cadence based SPICE simulation of the circuit in Figure 4.8 demonstrates the activation profile of different floating gate cells F1-F7 at different peak input voltage amplitude. For this experiment a storage capacitor of 10 nF was chosen, and the duration of the simulated piezoelectric pulse excitation was set to 2 seconds. The circuit exhibits a start-up time of about 100 ms, which is sufficient for most civil engineering applications. The start-up however, can be optimized by appropriately sizing the storage capacitor at the rectifier but at the expense of lower coupling voltage (rectifier). Simulation results shown in Figure 4.9 clearly illustrate that different floating-gate cells are activated at different input levels. The simulation also shows poor current regulation of the reference circuit due to sub-threshold operation of the circuit, but does not adversely affect the response of the sensor.

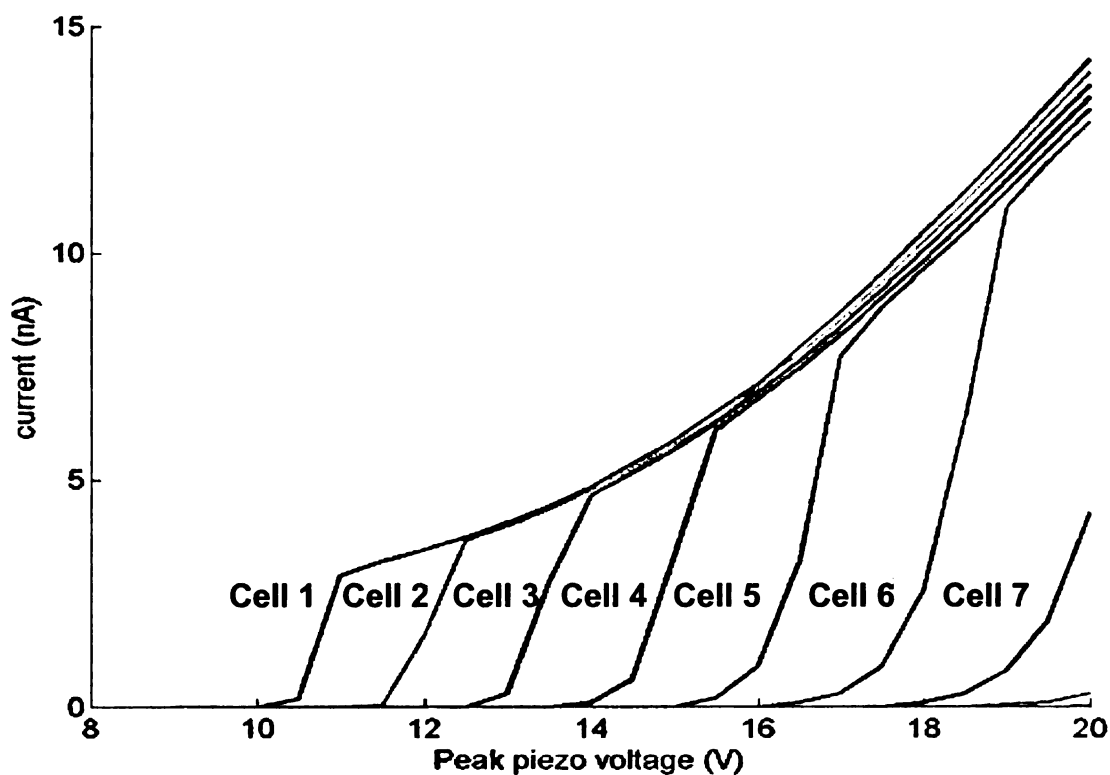


Figure 4.9 Simulation result using the circuit in Figure 4.8, showing the current through the floating gate cells for different peak excitation input voltage

4.6 CONCLUSION

In this chapter, the feasibility of a self-powered event monitoring system based on a combination of piezoelectric transduction and floating gate injection was shown. The proposed system exploits computational primitives inherent in a current starved IHEI on a floating-gate transistor that is biased in weak-inversion region. Comprehensive theoretical models for different components of the VLSI circuits were discussed. Cadence based SPICE simulation results confirm the desired behavior of the proposed design.

Experimental measured results, that will verify the theoretical models proposed in the previous sections, as well as the global performance of the complete sensor array, will be presented in the next chapter. The integration of the proposed circuits with piezoelectric generators, under real civil engineering environments, will be also discussed.

CHAPTER 5

RESULTS AND DISCUSSION

5.1 INTRODUCTION

In the previous chapters, the feasibility, design and implementation of a novel piezo-powered analog floating gate sensor was discussed. The proposed sensor would be able to record cumulative statistics of the stress/strain history undergone by a mechanical system. The concept of operation is based on the coupling of piezo-electric transducers with floating gate analog memory transistors. Based on the electrical signal generated by the transducer due to the induced stress, electrons are injected onto a floating node. The total charge accumulated on the floating gate would indicate the number of stress-strain events. This chapter focuses on the testing and validation of the presented concept. The important validation factors include: the control of the rate of injection of the floating gate transistor, the monotonic response of the sensor to the cumulative input signal, the robustness of computation to different artifacts (mismatch and temperature), and the power dissipation of the complete system and its accordance with the 1 μ W power requirement determined in chapter 2.

Several prototypes of the floating-gate injector array have been fabricated and tested. Figure 5.1 shows the micrograph of the latest tested version manufactured in a standard 0.5 μ m CMOS process. Its specifications are summarized in Table 5.1. (Detailed graphs of different components and the micrographs of different prototypes are shown in the Appendix).

A complete sensor will have the piezoelectric transducer outputs directly connected to a full-wave rectifier, implemented using a standard diode bridge. For the tested prototype,

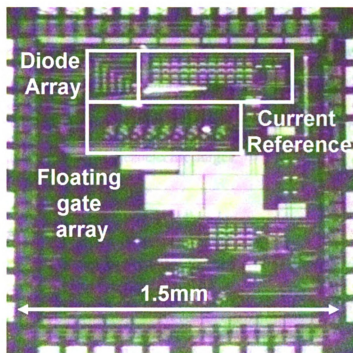


Figure 5.1 Micrograph of the prototype floating-gate sensor

Table 5.1 Summary of measured specifications

Parameter	Value
Technology	0.5 μm CMOS
Size	1.5 mm x 1.5 mm
Number of Injectors	7
Injection Range	4.2 V - 8 V
Maximum Current	160 nA
Startup Time	<30 ms

n^+ / p^- substrate and p^+ / n^- well diodes were used, which are naturally integrated on electrostatic discharge (ESD) protection pads of the VLSI chip. A storage capacitor is used at the output of the rectifier to filter out unwanted high-frequency components. The

size of this capacitor also provides a trade-off between the total hold-time versus the voltage swing at the sensor. For the prototype, an external capacitor (10 nF) was chosen, which is equivalent to a voltage swing of up to 8 V across the rectifier when a 20-V pulse is generated by the piezoelectric transducer. A voltage over-protection and clamping circuitry (consisting of zener diodes) was integrated at the output of the diode bridge to prevent damage due to unwanted piezoelectric surges.

5.2 SYSTEM ROBUSTNESS

From Equation (4.14), it can be seen that the differential response of a floating gate injector, and hence the output of the sensor array, is independent of the parameter K_1 . However, the robustness of the parameter K_2 to process artifacts still needs to be addressed. Several experiments were conducted to quantify the robustness of the parameter K_2 to different biasing and mismatch conditions. Figure 5.2 shows the responses obtained from multiple injectors on the same chip that were biased with different current sources (I_b). The mismatch in the parameter (K_2) was calculated to be less than 10% for a bias current variation greater than 100%. This result is encouraging since it implies that the precision of the current source is not critical for the operation of the floating-gate injector. Figure 5.3 shows the responses obtained from multiple injectors biased using the same source current but implemented on different chips for the same manufacturing run. The fabrication related mismatch was computed to be less than 15%. Figure 5.4 shows the response of the injector obtained for two different temperature

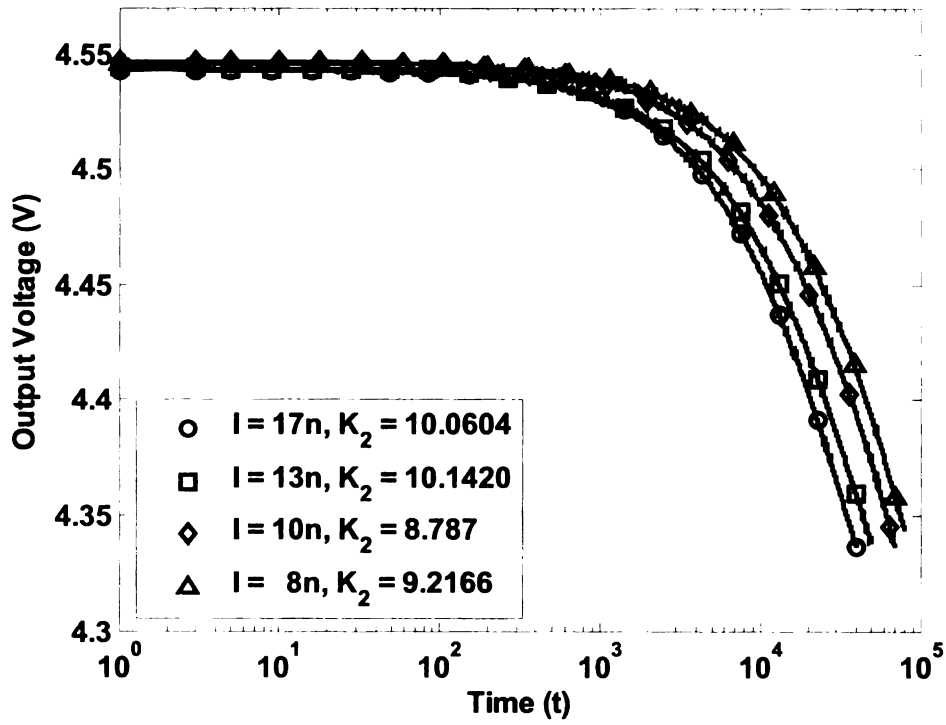


Figure 5.2 Voltage responses measured at various source currents

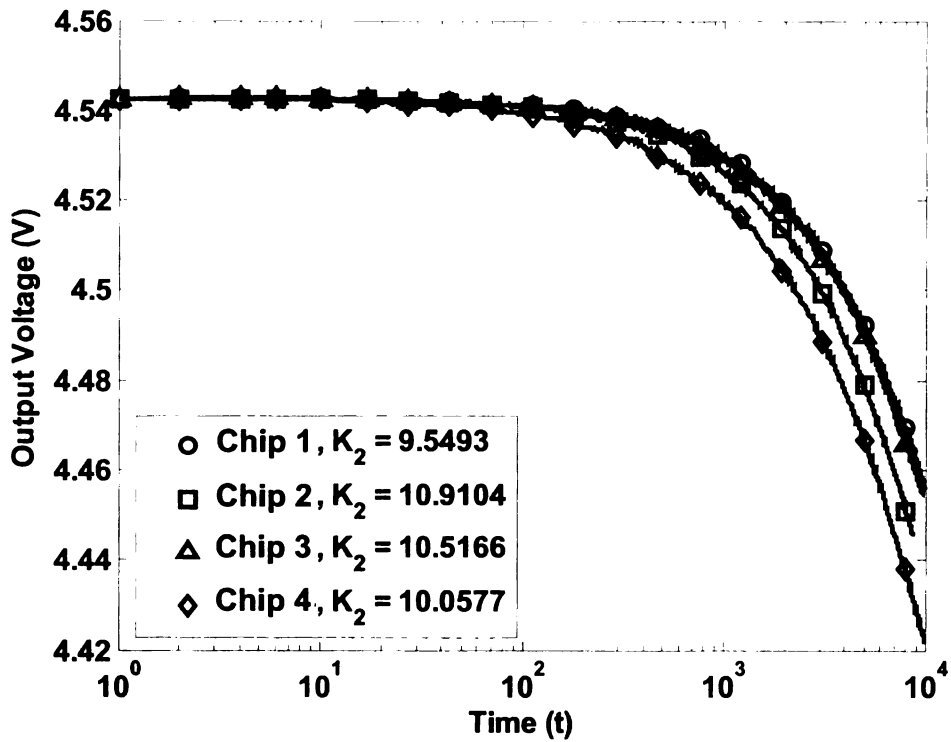


Figure 5.3 Voltage responses measured for various chips in the same run

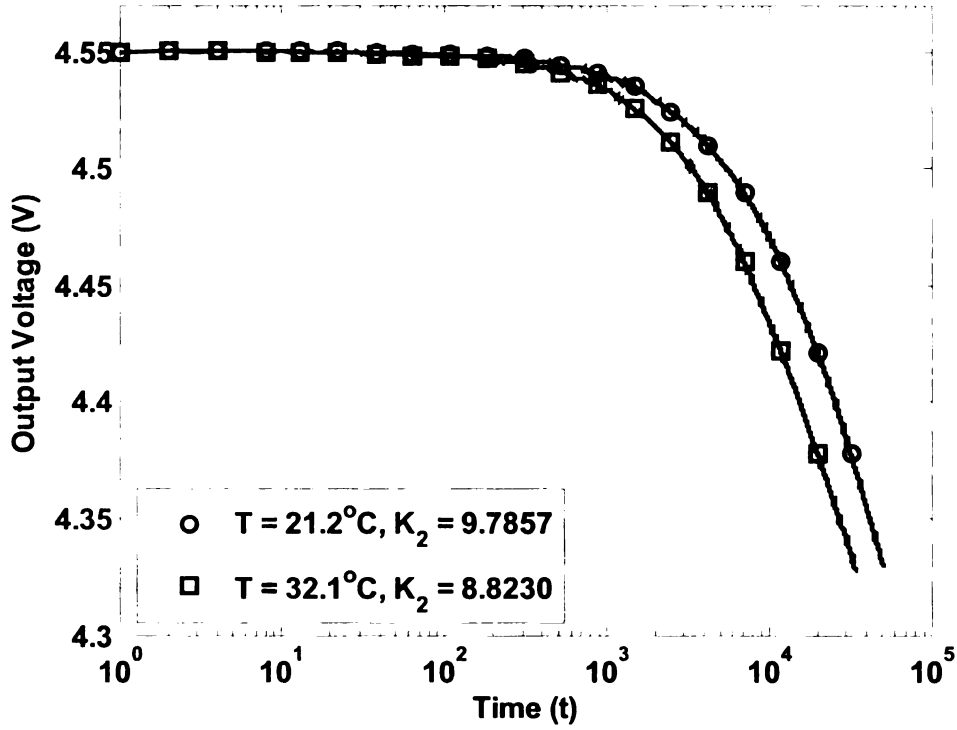


Figure 5.4 Voltage responses measured for various temperatures

levels. We have conducted the experiments over a range of 10°K and have observed less than 10% variation in the slope parameter K_2 . The measured results summarized in Figures 5.2 – 5.4 thus demonstrate that the parameter K_2 is robust to variations in biasing and ambient conditions.

5.3 EXPERIMENTAL MEASUREMENTS

5.3.1 Initialization of the injectors array

Before the prototype is used for monitoring, an equalization procedure is required to initialize the state of the floating-gate injector array. The equalization algorithm is summarized as a flow chart in Figure 5.5.

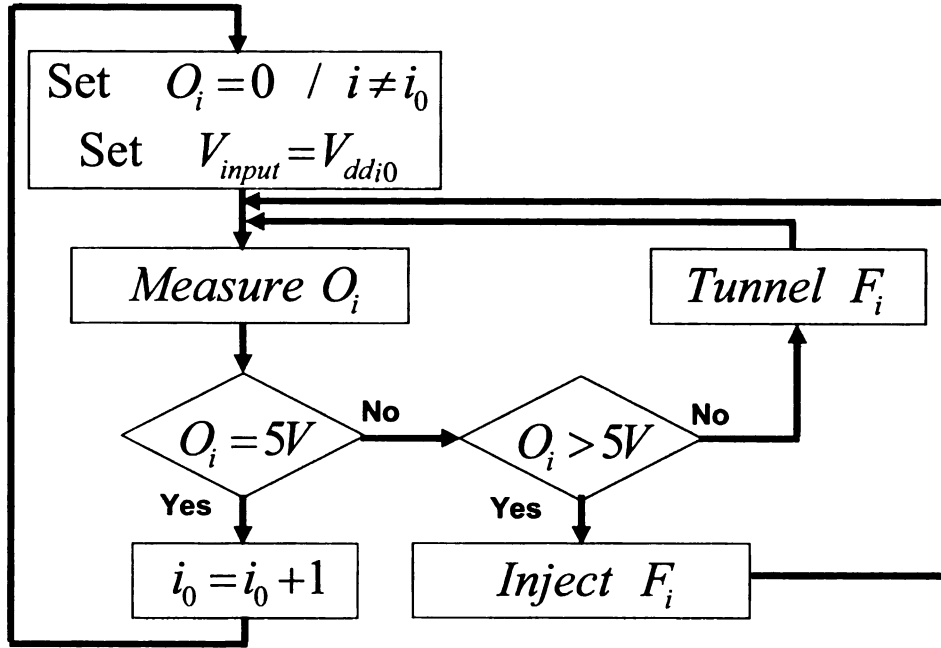


Figure 5.5 Flow-chart describing the sensor initialization algorithm

Initially, each of the floating-gate cells F1–F7 (Figure 4.10) is programmed (using tunneling and injection) to store a fixed amount of charge and hence a fixed floating-gate voltage across F1–F7. The channel to be initialized is first selected by connecting the source of all other channels to the terminal V^- . This ensures that these channels are unaffected when the selected channel is being initialized. For the sake of clarity the programming transistors have not been shown in Figure 4.8. The IHEI is then initiated on the selected channel by applying a large potential difference across the terminals V^+ and V^- . As a result the potential of the selected output node decreases. FN tunneling is then used by applying a large potential (>16 V) on the tunneling node (also not shown in Figure 4.8 – shown as node T in Figure 4.4) which results in an increase in the output voltage. These gate voltages are indirectly monitored by measuring drain-to-source

voltages across each of the floating-gate cells ($O_i, i = 1, 2, \dots, 7$). For different supply voltages $V_{ddi}, i = 1, 2, \dots, 7$, the procedures are repeated until the output node potential is programmed to $V_{s0} = 5$ V. The choice of this voltage was to ensure that sufficient drain-to-channel potential exist to initiate the IHEI process, when input voltage exceeds a prescribed threshold.

5.3.2 Threshold adjustment and levels detection

The minimum voltage required to initiate injection on a floating-gate cell can be calculated according to Equation 4.18 where M is the number of series pMOS diode connected transistor for the channel. It can be seen that the resolution of thresholds can be controlled either by changing M or by changing the reference current I_b (using a different value of resistance R for the current reference). Figure 5.6 shows the measured results obtained after the output voltage of the first four injectors in Figure 4.8 were initialized, using the algorithm shown in figure 5.5, and the input voltage ($V^+ - V^-$) is varied from 4V to 8V. It can be seen from Figure 5.6 that the responses of the injectors are offset by potential difference proportional to the number of series diodes. This implies that different channels will start the IHEI at different levels of the input voltages. Figure 5.6 also illustrates the heuristic threshold level (drain-to-channel voltage) required to trigger the IHEI. For the 0.5- μm CMOS process, the injection threshold is approximately 4.2 V which also justifies the choice of the initialization voltage $V_{s0} = 5$ V.

The level-selection functionality of the prototype was validated by applying voltage pulses of different magnitude using a programmable signal generator. These voltage

pulses were used to emulate the output of a piezoelectric transducer. The startup time for the current reference and injection circuitry was measured to be less than 30 ms, which is sufficiently fast for a typical loading cycle (assumed to be 1000 ms). Figures 5.7 to 5.9 show the measured output voltages O1–O3 corresponding to the three injector cells F1–F3, for continuous amplitude voltage pulses of different amplitude ($V_{dd1}=5.3$ V, $V_{dd2}=6.1$ V and $V_{dd3}=6.9$ V). Before each run, the floating-gate cells were initialized using the algorithm described in section 5.3.1.

It can be seen from Figure 5.7 that only cell F1 injects when pulses of amplitude 5.3 V are applied. Also the response of the injector F1 is log-linear and produces a change in output voltage as a function of the duration of injection. The cells F2 and F3 show negligible injection compared to cell F1. Figure 5.8 shows the response of the injector array when voltage pulses with amplitude 6.1 V were applied. Both F1 and F2 inject at an identical rate, whereas cell F3 shows negligible injection. Thus cells F1 and F2 gather statistics of occurrence of events when voltage amplitude exceeds 6.1 V. For pulses with amplitude greater than 6.9 V, all the cells F1–F3 inject at identical rates (Figure 5.9) and the responses show excellent agreement with the mathematical model in Equation (4.13) shown in Figure 4.5. Using the model in Equation (4.13), the total duration that a cell injects before it approaches the threshold (4.2 V) is calculated to be approximately 70,000 seconds. This period can be easily extended to beyond 10^7 cycles by varying the design parameters such as gate capacitance and injection current.

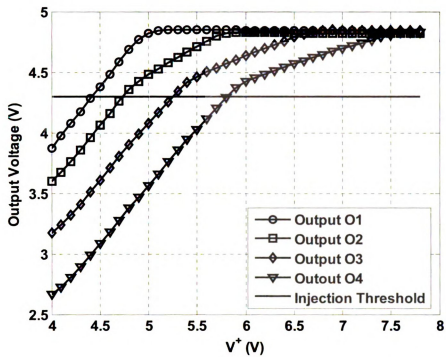


Figure 5.6 Measured output voltages (O1–O4) response vs. input voltage

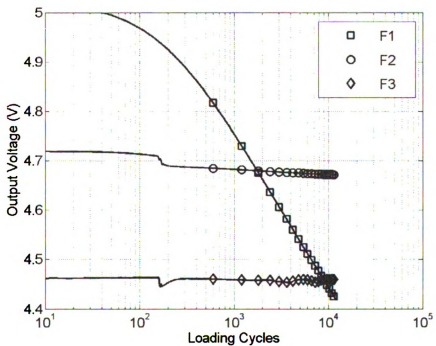


Figure 5.7 Measured source-to-drain voltage response across floating-gate elements at $V_{dd}=5.3V$

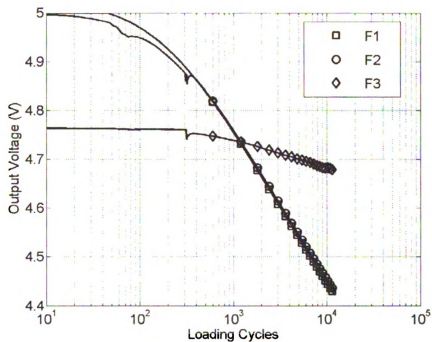


Figure 5.8 Measured source-to-drain voltage response across floating-gate elements at $V_{dd}=6.1V$

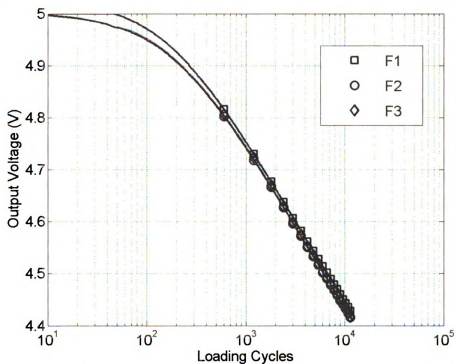


Figure 5.9 Measured source-to-drain voltage response across floating-gate elements at $V_{dd}=6.9V$

5.3.3 Level-crossing Counter

The next set of experiments was designed to evaluate the performance of the injector array under variable loading conditions and verify the level-crossing algorithm. The floating-gate elements were first initialized using the algorithm described in Figure 5.5. The programmable voltage source was used to generate a periodic arbitrary waveform consisting of three different levels (5.3 V, 6.1 V, and 6.9 V).

A sample voltage waveform used for one of the experiments is shown in Figure 5.10, where the duration of the three levels were programmed to be in the ratio of 3:2:1. The measured response from the injector array is also shown in Figure 5.10. The difference in duration of injection translates into an offset in the log-linear response and is evident from the measured results. Figures 5.11 and 5.12 show the response of the injector array for loading cycles with different durations at the various voltage levels. It can be seen from the measured results that the array indeed can capture the monotonic relationship of the statistics in the offsets between the measured voltage curves. The offset, however, also contains information regarding the initial conditions, thus, any error in initializing the injector array will appear as a measurement error.

A calibration scheme based on Equation (4.14) has been applied to compensate for offsets introduced by ambient conditions. The calibration scheme exploits the log-linear response of the floating-gate injector as described by Equation (4.13). When the injector operates for a long duration $t \gg \exp(-K_2 V_{s0})/K_1 K_2$ the response of the injector can be approximated by $V_{out}(t) \approx -\ln(t)/K_2$, which is independent of the initialization conditions. For initialization errors less than 10%, the shortest duration (referred to as calibration period in this thesis) required to achieve compensation is approximately 10^3

seconds. This is verified using measured responses as shown in Figures 5.13 and 5.14, where three injectors (corresponding to channels 1-3) are initialized using the procedure in Figure 5.5. The initialization errors can be seen as the offset in the source voltage measured for each of the channel at $t = 0$ s. The calibration procedure entails operating all the injectors for a duration of 1000 seconds. It can be seen from the measured responses that all three injectors self-calibrate themselves (converge to the same output voltage) at the end of the calibration period (1000 cycles).

Subsequently, the cells are subjected to variable loading cycles, whereby each cell injects only for a fraction of the duration. If α denotes the fraction of total injection period, then

$$\Delta V_{out}(t) = -\frac{1}{K_2} \log\left(\frac{t_0 + \alpha \Delta t}{t_0}\right) \quad (5.1)$$

and the parameter α can be calculated as:

$$\alpha = \frac{\exp[-K_2(V_{out1}(t) - V_{out1}(t_0))] - 1}{\exp[-K_2(V_{out2}(t) - V_{out2}(t_0))] - 1} \quad (5.2)$$

where V_{out1} and V_{out2} are the output voltage for cells F1 and F2. In Figure 5.13, the parameter α is computed to be equal to 0.30 for cell F3 and 0.71 for cell F2, which is close to the ratios 1/3 and 2/3. The sources of error include a mismatch in parameter K_2 for the different cells, as well as imperfect startup and shutdown of the injector cells. Figure 5.14 shows a similar result but for a different ratio (3:2.5:1) of loading cycles. It can be seen from Figure 5.13 and Figure 5.14 that the offset between injection response for cells F1 and F3 is identical, whereas the offset between F1 and F2 has been reduced, which is consistent with the statistics of the loading cycles.

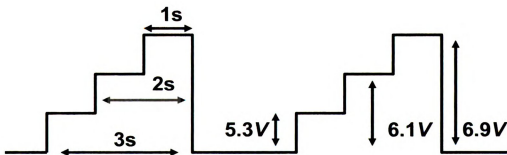
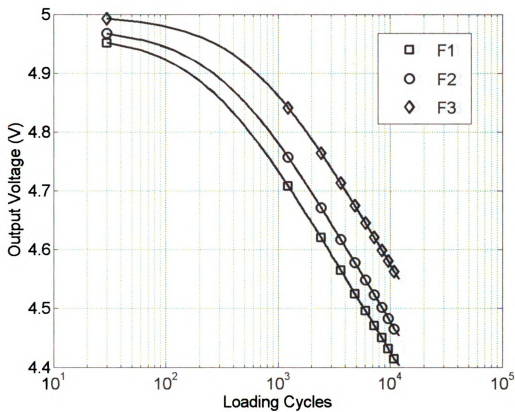


Figure 5.10 Measured output voltage response for the sensor array when subjected to a loading cycle represented by a piezoelectric output with injection duration 3:2:1

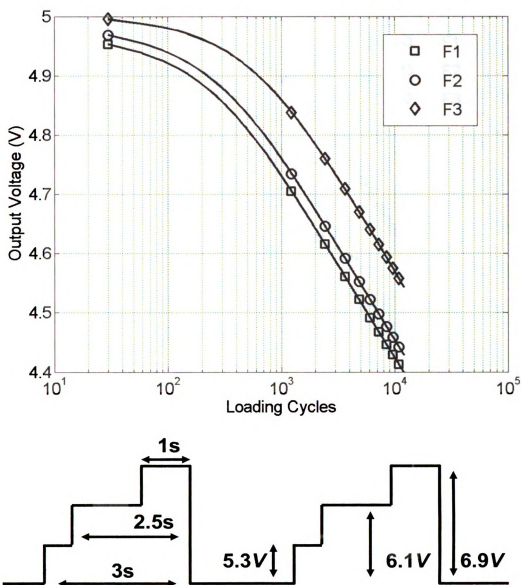


Figure 5.11 Measured output voltage response for the sensor array when subjected to a loading cycle represented by a piezoelectric output with injection duration 3:2.5:1

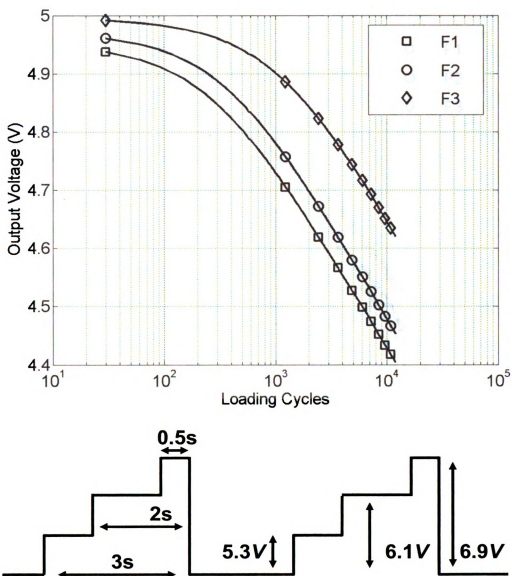


Figure 5.12 Measured output voltage response for the sensor array when subjected to a loading cycle represented by a piezoelectric output with injection duration 3:2:0.5

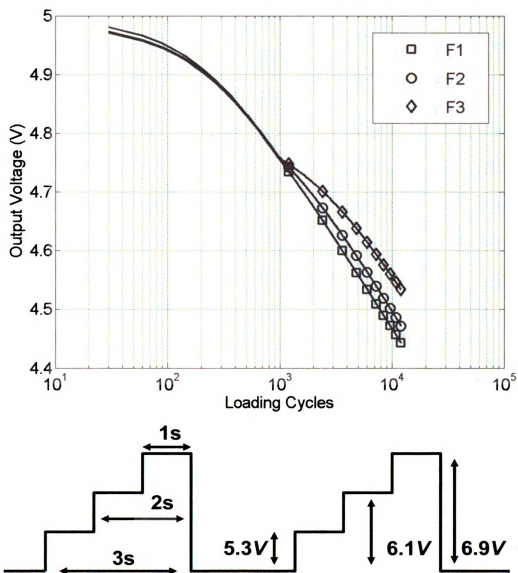


Figure 5.13 Measured output voltage response using the sensor array in which the first 1000 cycles have been used as calibration intervals and the subsequent three level loading cycles where the durations of injection are in the ratio 3:2:1

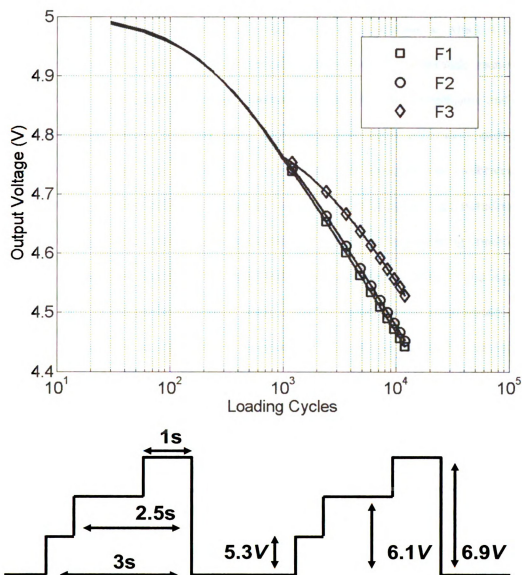


Figure 5.14 Measured output voltage response using the sensor array in which the first 1000 cycles have been used as calibration intervals and the subsequent three level loading cycles where the durations of injection are in the ratio 3:2.5:1

5.3.4 Counting Resolution

The next sets of experiments were used to determine the resolution at which a single floating-gate injector can count the number of events (when the amplitude exceeds a given threshold). Only the first injector channel was used for this experiment and was subjected to voltage pulses (generated using a programmable signal generator), each with a duration of 1 second and amplitude of 5.5V. First, the injector was calibrated by applying 1000 calibration pulses of a duration of 1 second to eliminate any initialization errors. The voltage pulses were then programmed according to the following conditions: for the first set of experiments 256 voltage pulses were directly applied to the injector (referred to as 256/256 in the measured result); for the second set of experiments only 248 out of 256 pulses were applied to the injector; the process was repeated using 240 out of 256 pulses until 0 pulses out of 256 were applied to the injector. The measured results for all of the above set of experiments are summarized in Figure 5.15(a) and its inset in Figure 5.15(b). The measured results show a monotonic relationship between the injector voltage and the count of the voltage pulses applied to the injector. It can also be seen that the proposed injector can count events at a resolution of more than 5 bits.

5.3.5 Power dissipation

The power dissipation of the sensor (current reference and floating gate array) was calculated at different voltage levels and is summarized in Figure 5.16. It can be seen that the total current drawn by the sensor saturates around 6.5 V where all the injectors become active. Thus, the nominal power dissipation of the sensor at 5.5 V is 800 nW. More importantly, the impedance of the sensor is 40 M Ω , implying that the proposed sen-

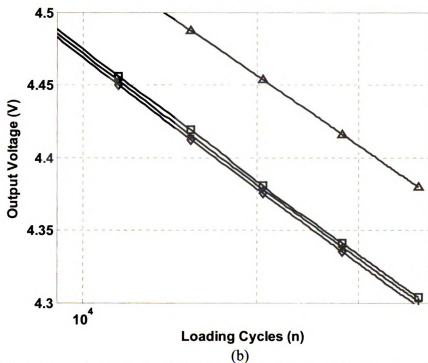
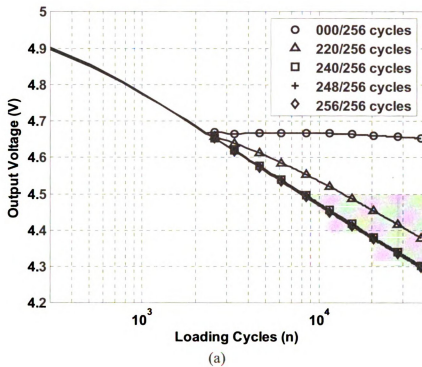


Figure 5.15 Measured results to calculate the resolution for event counting: (a) Change in source voltage measured for different relative counts of voltage pulses for over 100,000 events; (b) Inset showing zoomed area between 10,000 to 40,000 events

sor could also be interfaced with other power harvesting sources that typically have low current driving capability.

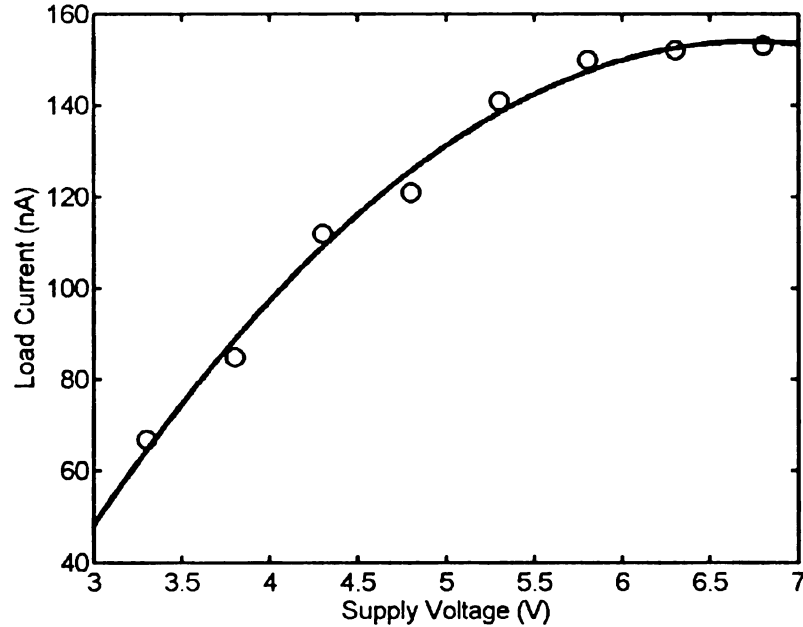


Figure 5.16 Supply current drawn by the sensor at different supply voltages

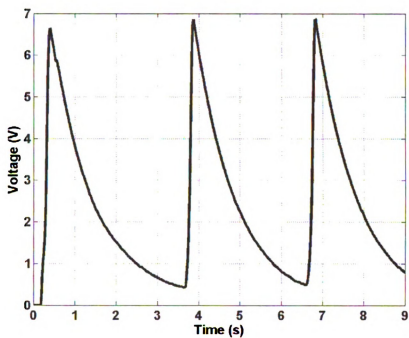
5.4 DESIGN EXAMPLES FOR SYSTEMS MONITORING – SENSOR AND TRANSDUCER INTERFACING

For the first set of experiments, the prototype injector array was interfaced with a piezoelectric transducer (PZT). The transducer was mounted on an extruded acrylic cantilevered beam. The beam was then subjected to periodic loading cycles. An external capacitor (100 nF) was chosen which is equivalent to a voltage swing of up to 8 V across the rectifier when a 20 V pulse is generated by the piezoelectric transducer. An over-voltage protection and clamping circuitry (consisting of zener diodes) was integrated at the output of the diode bridge to prevent damage due to unwanted piezoelectric surges. Figure 5.17(a) shows a sample waveform recorded at the output of the half-wave rectifier

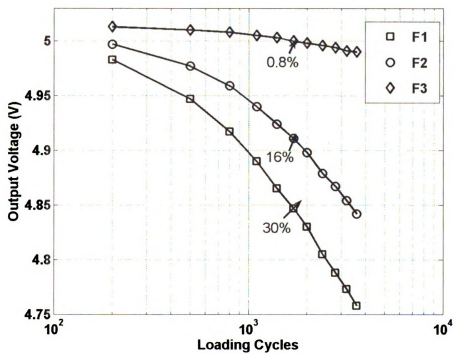
integrated on-chip with the injector array, showing that for the loading cycles the transducer can easily generate voltage levels close to 7 V. The measured response for each of the injectors in the array is shown in Figure 5.17(b). The results clearly show monotonic response across the three injectors and that each response is proportional to the total duration for which the strain levels exceeded the programmed thresholds. The injector responses were then calibrated against Figure 4.5 and Equation (4.13) to determine the loading statistics which can then be used in Miner's rule. For instance, the cumulative loading statistics calculated at a given time are indicated in Figure 5.17(b), which shows that 30% of the time the structure experienced strain levels exceeding the threshold for injector 1, 16% of the time experienced strain levels exceeding the threshold for injector 2, and less than 1% of the time experienced strain levels exceeding the threshold for injector 3.

The second set of experiments was designed to test the ability of the sensor to record low frequency loads. To understand the limitations imposed by low-frequency operation, consider a simplified equivalent model of the prototype sensor interfacing with the piezoelectric transducer. The transducer is modeled using an AC voltage source connected to a decoupling capacitor C (Figure 2.2). The processor has been modeled as a simple resistive load R_z .

As discussed in section 2.3.1, for a harmonic mechanical loading of the piezoelectric transducer at a frequency f Hz, the magnitude of the voltage across the sensor is given by Equation (2.5), and the power delivered to the load (sensor) can be optimized with respect to the load R_z . A typical loading frequency of 1 Hz and a typical PVDF capacitance of 10nF would yield an optimal load of the processor circuit of about 15 M Ω .



(a)



(b)

Figure 5.17 (a) Voltage generated by a piezoelectric transducer in response to periodic loading; (b) Measured response of the floating-gate injector array

For a 5 V input voltage, this is equivalent to a load current of 300 nA. The total current drawn by the fabricated prototype has been measured to be 160 nA at 6.7 V which is clearly less than the optimal load current and hence is ideal for this application.

The integrated sensor (piezoelectric transducer and floating-gate injector IC) was attached to a plexiglass beam and the setup was mounted on a testing system (MTS machine) as shown in Figure 5.18. The MTS machine was programmed to generate three distinct levels of displacement at the center of the beam. The averaged strains over the length of the PVDF transducer were calculated to be 2107 $\mu\epsilon$, 2546 $\mu\epsilon$ and 2809 $\mu\epsilon$. The size of the transducer was selected so that the first tested load level would yield enough voltage to activate only the first injector F1 (a PVDF sheet of dimensions 62 mm x 12 mm x 28 μm was used). The mechanical loading was cyclically applied to the plexiglass beam at a loading frequency of 1 Hz. Figure 5.19 shows that when 2107 $\mu\epsilon$ strain was applied only the first channel records a change in output voltage. When loading cycles corresponding to 2546 $\mu\epsilon$ are applied, both channels 1 and 2 record change in voltage whereas the channel 3 voltage remains unchanged (shown in Figure 5.20). When the input load level exceeds 2809 $\mu\epsilon$, the first three cells F1-F3 are simultaneously active (Figure 5.21). Although no calibration is performed in advance, the offset in measured output voltage can be used to determine the count of loading cycles with different strain levels.

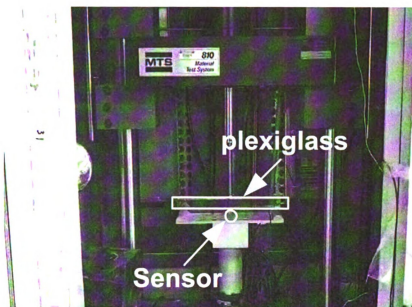


Figure 5.18 Setup environment for MTS machine

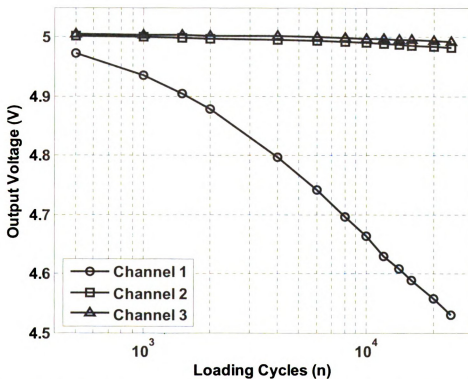


Figure 5.19 Voltage responses measured when the prototype is interfaced with a PVDF transducer and subjected to controlled cyclic strain levels with magnitude $2107 \mu\epsilon$

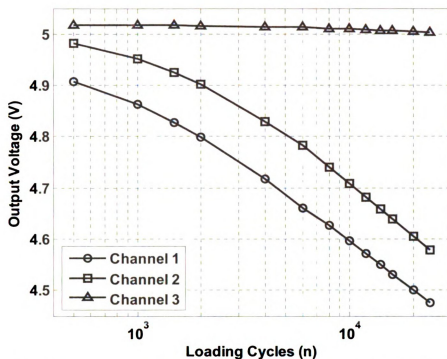


Figure 5.20 Voltage responses measured when the prototype is interfaced with a PVDF transducer and subjected to controlled cyclic strain levels with magnitude 2546 $\mu\epsilon$

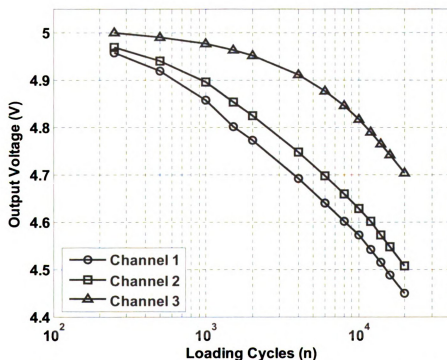


Figure 5.21 Voltage responses measured when the prototype is interfaced with a PVDF transducer and subjected to controlled cyclic strain levels with magnitude 2809 $\mu\epsilon$

5.5 DISCUSSION

Even though the measured results shown in the previous sections have demonstrated the operation of the floating-gate injectors for up to 10^5 loading cycles, we have observed deviations from the log-linear response beyond 10^5 loading cycles. Figure 5.22 shows a sample response obtained using three injectors (channels 1-3) operating up to 10^6 loading cycles. It can be seen from Figure 5.22, that the response follows a superposition of two log-linear responses. We believe that a possible explanation to the appearance of the superposition term could be the contribution from interstitial traps which releases electrons back in to the transistor channel. At high injection rates (greater than 100 electrons per second) the de-trapping behavior is masked but becomes dominant when the injection rate reaches as low as 1 electron per second.

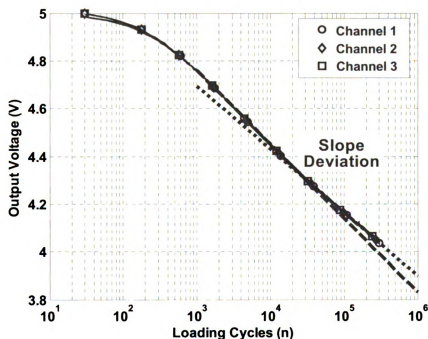


Figure 5.22 Slope deviation observed for injection currents less than 1 electron per second

Even though the power dissipation of the fabricated prototype is less than 800 nW which makes it suitable for self-powered usage monitoring at a harmonic loading of around 1 Hz (which is typical of most mechanical loading in civil engineering), there are applications which require monitoring at much lower frequencies such as the monitoring of strain cycles due to daily temperature fluctuations (corresponding to a period of about 24 hours). In such cases, the required power dissipation is less than 30 nW. We believe that the current design can achieve this requirement by starving the injection currents using a higher value of current reference resistance R .

The minimum amplitude of transducer signal required to initiate injection is measured to be approximately 4.2 V. Even though piezoelectric transducers can easily generate the minimum operational voltage, other transducers typically generate sub-volt signals. We anticipate that this limitation could be overcome by using a sub-100 nm process where the minimum IHEI voltages is significantly lower than that of required by a 0.5- μm CMOS process. In the future, memristors could be used instead of floating-gate injectors. However it is not known if the log-linear response could be replicated.

5.6 CONCLUSION

In this chapter, the design and models presented in chapter 4 were validated using a fabricated prototype. We have demonstrated that the response of the system is robust to device mismatch and temperature variations. Furthermore, it has been shown that the level counting circuit can sense store and compute over 10^5 event cycles with injection currents less than 1 electron per second. At a total power dissipation of less than 800 nW, the fabricated prototype is ideal for interfacing with piezoelectric transducers and was

shown to count the occurrence of mechanical loading of structures. The proposed sensor has numerous applications in long-term structural health monitoring, where a large number of prototypes could be embedded directly inside a material and can autonomously record statistics of its mechanical loading (usage).

CHAPTER 6

CONCLUSIONS AND RECOMMENDATIONS

In this thesis, a novel piezo-powered floating gate array that can sense, compute and store cumulative statistics of loading cycles experienced by a mechanical structure was presented. **The nominal power dissipation of the integrated circuit is less than 1 μW , this is 2 orders of magnitude smaller than the best currently available self-powered sensors.** The lower power usage, along with its small form factor makes it ideal for sensing and long-term monitoring of civil infrastructure. The work reported in this dissertation provides an initial step toward the implementation of complete low cost and reliable monitoring networks.

Traditional self-powered wireless sensor systems consist of a microprocessor, radio, data storage, and batteries. Commercial electronic components are commonly used in these systems. The harvested energy is accumulated in a capacitor, and a switch is used to allow the capacitor to charge to a predetermined voltage value at which point the switch would open and the capacitor is allowed to drain through the circuitry. Once the capacitor had discharged to a second predetermined value, the switch closes and the capacitor is allowed to recharge. The entire process is then repeated. Leakage through the switch, combined with the power requirements of the various components limit the possible functionalities that could be achieved using the extracted power. For example, the MSP430 microprocessor by Texas Instrument operates at a 350 μW power consumption, and a 1-bit Analog to Digital (A/D) conversion consumes 2 nJ of energy.

Directly using analog signal processing circuits eliminates the need for digital conversion, thus reducing the power demand. Furthermore, analog computations can use

solid-state transistor physics to implement complicated mathematical relations. For example, a pMOS operated in the sub-threshold regime inherently calculates the exponential/logarithm relation by simply transforming voltage to current. This alleviates the need for digital logic components, energy costly microprocessor and leaky switches. In addition, analog floating-gate programming can be performed with power dissipation as low as 100 pW during the write cycle, compared to digital FLASH programming that consumes 100 to 200 nW. The principle of operation of the novel sensor developed in this work is based on the integration of piezoelectric transducers with ultra low power analog computation circuits and analog floating-gate memory.

Different approaches to convert mechanical energy to electrical energy for self-powering sensor electronics were discussed. Piezoelectric energy harvesting was selected as the focus of this research as it was proven to be the most appropriate technique for the studied applications. Simple mechanical and equivalent electrical models that can be easily used for a general piezoelectric generator analysis were presented. The electrical models could be easily implemented into existing circuit simulation programs (such as SPICE) and provide reasonably accurate estimates of the generator performance under a wide variety of ambient loading environments.

Using the developed models and assuming a 5 cm^3 sensor node, it was shown that the electrical energy generated under typical civil structures service conditions (approximately $1 \text{ } \mu\text{W}$) is insufficient to run modern wireless sensors. Piezoelectric-based vibration harvesters do produce enough energy from large-scale earthquakes and high

vibration environments; these events can allow for approximately 500 data samples to be collected and wirelessly transmitted by a sensor node.

The design and theoretical model of a novel piezoelectric based self-powered event monitoring system was presented. The novel features of the developed system include (1) self-powered, continuous and autonomous sensing, the sensor uses novel analog signal processing circuits that require less than $1\mu\text{W}$ of power (to our knowledge this is two orders of magnitude less power than previously demonstrated self-powered sensors), (2) autonomous computation and non-volatile storage of the sensed variables, the sensor uses floating gate transistor injection principles for computing cumulative mechanical strain patterns experienced by a structure.

A complete system, piezoelectric transducer and a fabricated prototype, was tested under realistic low-frequency, civil engineering loading in the laboratory. It was shown that the developed sensor can sense store and compute over 10^5 loading event cycles at a total power dissipation of less than 800 nW .

One of the future key challenges will be to remotely access the loading statistics accumulated on the floating gate sensor. Therefore, the sensor array needs to be interfaced with a data transmission circuit which can be remotely powered and interrogated using an RF signal. The envisioned system would consist of a network of low costs sensors distributed through the structure (for example a bridge). Each sensor node would be self-powered and capable of continuously monitoring and storing the dynamic stress/strain levels in the host structure. The data from all the sensors would be

periodically uploaded wirelessly to a central database using low cost RF transponders. The monitored host structures can be frequently monitored to detect changes in structural integrity that may not only foreshadow a severe failure, but also allow for more accurate maintenance and repair scheduling.

Figure 6.1 shows a possible system level architecture of a complete sensor node that integrates the proposed piezo-floating gate array. The sensor would consist of two sub-systems: (a) a self-powered sub-system consisting of a floating-gate sensor array, and (b) a radio-frequency identification (RFID) interface that facilitates remote access to the stored features. Before the sensor is deployed the floating-gate array should be calibrated/equalized offline. The operation of a deployed sensor will then consist of two modes: 1) a continuous monitoring mode where the energy harvested from the applied mechanical stresses is used for computing and storing loading statistics, and 2) an access mode where an RF reader is brought in proximity to the sensor which powers up the analog-to-digital (A/D) converters and transfers the digitized representation of the stored statistics to a reader over the RF link. The measured statistics can then be used to determine the history of strain levels experienced by the structure using a calibration curve that equates the voltage generated by the piezoelectric transducer when subjected to different strain levels.

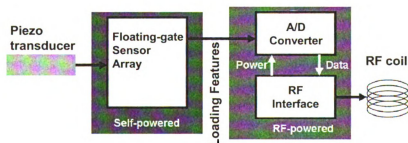


Figure 6.1 System architecture of a complete implanted device that integrates the proposed floating-gate sensor array

Durability of the sensors both during construction and throughout the lifetime of the structure is also a critical aspect for successful implementation. A robust package needs to be developed and tested in order to increase the sensor's robustness to withstand harsh environmental conditions. Several commercially available robust RFID tags use an ABS (acrylonitrile butadiene styrene) plastic package that is durable over a wide temperature range (-50 degrees to 180 degrees F). This packaging also can withstand mechanical abrasion and severe chemical attack, thus making it an ideal candidate for sensor packaging. Another potential candidate for packaging is polyurethane. This epoxy is commercially used for the manufacturing of RFID tags.

Successful development of the proposed sensor could dramatically transform the economics of civil infrastructure inspection by facilitating early damage detection and future condition evaluation. It is envisioned that the piezoelectric strain sensor could be reduced in cost to the order of \$2/sensor in the near term. Given the annual costs of infrastructure inspection, this sensor cost could rapidly pay for itself.

APPENDIX

APPENDIX

MICROGRAPHS AND LAYOUT DETAILS

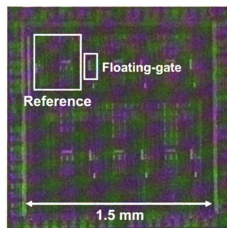
Figure A.1 shows the micrographs of the first three prototypes manufactured and tested in different optimization iterations. Each prototype represented an improvement with respect to previous designs based on experimental observations during laboratory testing.

Floating-gates manufactured in the first tested prototype, shown in Figure A.1 (a), performed as expected, injection curves were measured and matched with the developed theoretical models. But this prototype had a fundamental design problem. Since each floating-gate memory was connected to its own reference circuitry, mismatch between different transistors induced by the manufacturing process resulted in different startup behavior between references.

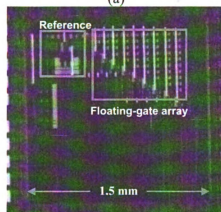
In the second generation shown in Figure A.1 (b), all memory gates were connected to the same reference, eliminating the startup mismatch. An innovative current reference was implemented in this prototype. The design was based on the integration of a floating-gate as a current mirror in the reference circuit in order to accurately control its output and improve its insensitivity to temperature fluctuations. The lack of control pins at the reference gate resulted in failed tests. The charge stored on the reference gate could not be controlled accurately, which resulted in a non-stable behavior of the reference. Similarly to the previous prototype, all floating-gates performed as expected.

The optimal reference design was included on the third prototype (Figure A.1 (c)). In order to improve the matching of injection rates between different gates, the bulk of each cell was connected to a common pin driven by the input voltage. This configuration disrupted the injection characteristics of the gates due to parasitic capacitances which

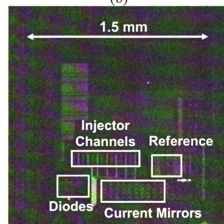
were not accounted for in the simulations. All optimal designs of the reference and the floating-gate cells were included in the fourth generation tested in Chapter 5.



(a)



(b)



(c)

Figure A.1 Micrographs of different prototypes

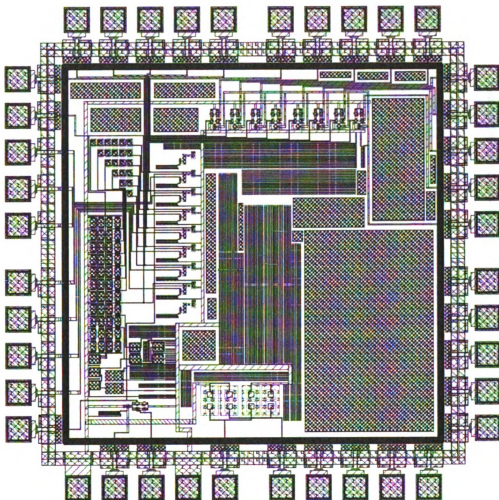


Figure A.2 Layout of the prototype tested in chapter 5

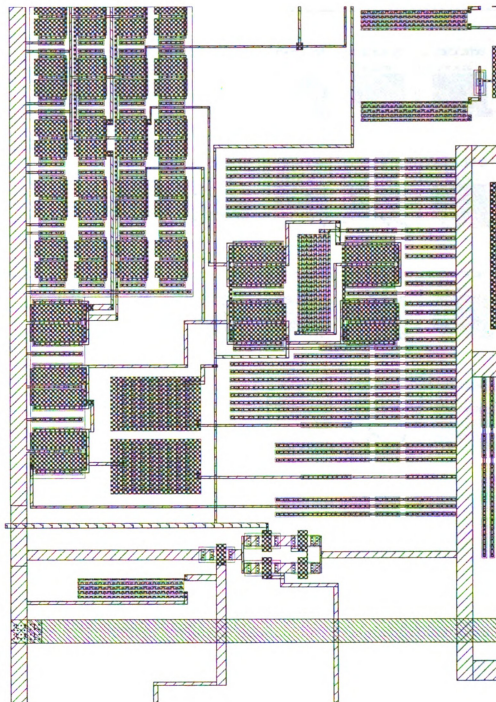


Figure A.3 Layout of the current reference

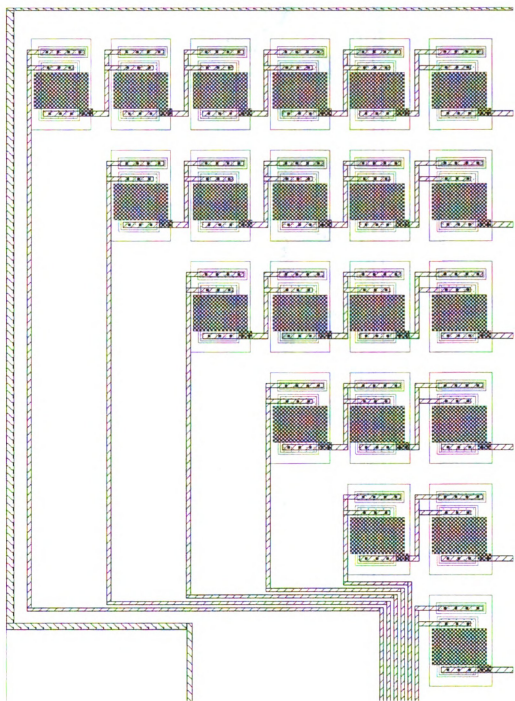


Figure A.4 Layout of the diodes array

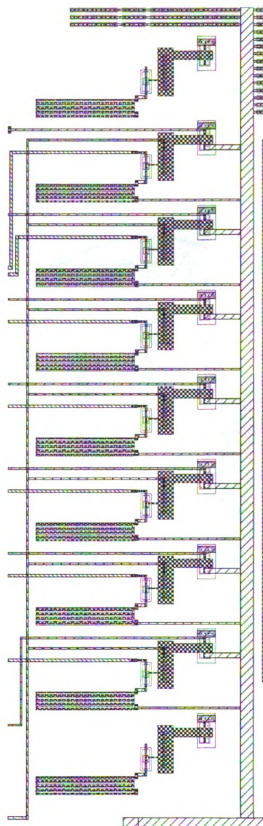


Figure A.5 Layout of the floating-gate injectors array

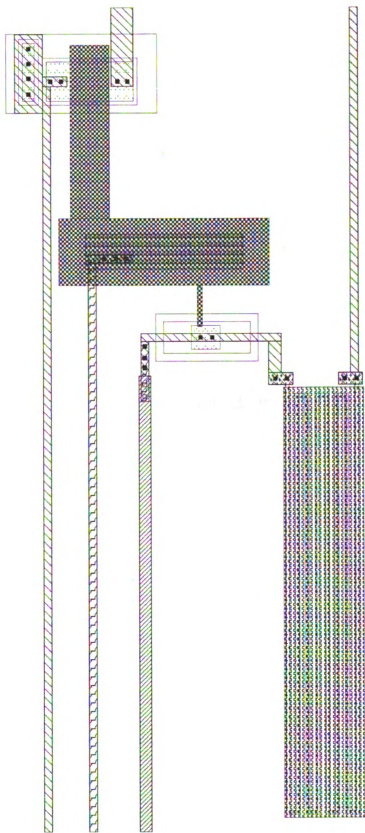


Figure A.6 Layout of a single floating-gate injector

BIBLIOGRAPHY

BIBLIOGRAPHY

1. Air Force Research Laboratory, "Engine Rotor Life Extension", Materials and Manufacturing Directorate, <http://www.ml.afrl.af.mil/ml/p_erle.html>, Accessed July 2008
2. Kamoi A, Okamoto Y, Vavilov V, 'Study On Detection Limit of Buried Defects in Concrete Structures by Using Infrared Thermography', *Key Engineering Materials*. Vol. 270-273, Part 2, pp. 1549-1555. 2004
3. Huston D. Hu JQ.; Maser K, Weedon W, Adam C., 'GIMA Ground Penetrating Radar System for Monitoring Concrete Bridge Decks', *Journal of Applied Geophysics*, Volume 43, Number 2, March pp. 139-146(8), 2000
4. Wang X., Chang C-C., Fan L., 'Nondestructive Damage Detection of Bridges: a Status Review', *Advances in Structural Engineering*, Volume 4, Number 2, 75-91, 2001
5. Zhao Z, Haldar A, Breen, FL, 'Fatigue-Reliability Updating Through Inspections of Steel Bridges', *Journal of Structural Engineering*., Vol. 120, no. 5, pp. 1624-1643. 1994
6. Akyildiz IF, Su W, Sankarasubramaniam Y, Cayirci E, 'Wireless Sensor Networks: a Survey', *Computer Networks*, 38 (2002) 393–422, 2002
7. Lynch JP, Sundararajan A, Law KH, Kiremidjian AS, 'Embedding Damage Detection Algorithms in a Wireless Sensing Unit for Operational Power Efficiency ', *Smart Mater. Struct.*, 13 800-810, 2004
8. Tanner NA, Farrar CR, Sohn H, 'Structural Health Monitoring Using Wireless Sensing Systems With Embedded Processing', *Proceedings of SPIE*, Vol. 4704, p. 215-224, 2002
9. Sazonov E, K Janoyan, R Jha, 'Wireless Intelligent Sensor Network for Autonomous Structural Health Monitoring', *Proceedings of SPIE: Smart Structures and Materials*, San Diego 5384 304-14, 2004
10. Chee-Yee Chong; Kumar SP, 'Sensor Networks: Evolution, Opportunities, and Challenges', *Proceedings of the IEEE*, Volume 91, Issue 8, Aug. Page(s): 1247 – 1256, 2003
11. Rajendran V, Obraczka K, Garcia-Luna-Aceves J, 'Energy efficient, Collision-Free Medium Access Control for Wireless Sensor Networks', *Proc. 1st international conf. an embedded networked sensor systems*, pp. 181-192, 2003

12. Hunt SR, Hebden IG, 'Validation of the Eurofighter Typhoon Structural Health and Usage Monitoring System', *Smart Material and Structures*, v.10 497–503, 2001
13. Haas DJ, Baker T, Spracklen D, Schaefer CG, 'Joint Advanced Health and Usage Monitoring System (Jahums) Advanced Concept Technology Demonstration (actd)', AHS International, Annual Forum, 56th, Virginia Beach, Proceedings. Vol. 2; 935-945, 2000
14. Chang FK, 'Structural Health Monitoring', CRC Press, 1999
15. Poncelet JV, 'Introduction à la Mécanique Industrielle, Physique et Expérimentale', pp. 317-8, Deuxième édition, Imprimerie de Gauthier-Villars, Paris, 1839
16. Basquin OH, 'The Exponential Law Of Endurance Tests', Proceedings of the American Society for Testing and Materials 10, 625-30, 1910
17. Coffin LF, 'A Study of the Effects of Cyclic Thermal Stresses on a Ductile Metal', Transactions of the American Society of Mechanical Engineers 76, 931-50, 1954
18. Mason SS, 'Fatigue—A Complex Subject', *Experimental Mechanics*, Vol. 5, No. 7, pp. 193–226, 1965
19. Suresh S, 'Fatigue of Materials', 2nd edition, Cambridge University Press, 1998.
20. Matsuiski M, Endo T, 'Fatigue of Metals Subjected to Varying Stress', *Japan Society of Mechanical Engineering*, 1969
21. Dowling NE, 'Fatigue Failure Predictions for Complicated Stress-Strain Histories', *Journal of Materials*, Vol. 7, No. 1, pp. 71-87, March 1972
22. ASTM E 1049-85, Standard Practices for Cycle Counting in Fatigue Analysis, *ASTM International*, 2005
23. Straser EG, and Kiremidjian AS, 'A Modular Visual Approach to Damage Monitoring for Civil Structures', Proceedings of SPIE v2719, Smart Structures and Materials. 112–122, 1996
24. Straser EG., Kiremidjian AS, Meng TH., Redlefsen L, 'A Modular, Wireless Network Platform for Monitoring Structures', Proceedings SPIE 3243:1:450–456, 1998
25. Kiremidjian AS, Straser EG, Meng TH., Law K, Soon H, 'Structural Damage Monitoring for Civil Structures', International Workshop Structural Health Monitoring. 371–382, 1997
26. Maser K, Egri R, Lichtenstein A., Chase S, 'Development of a Wireless Global Bridge Evaluation and Monitoring System (WGBEMS)', Proceedings of the

- Specialty Conference on Infrastructure Condition Assessment: Art, Science, Practice. 91–100, 1997
27. Mitchell K, Sana S, Balakrishnan VS, Rao V, Pottinger HJ, 'Micro Sensors for Health Monitoring of Smart Structures', SPIE Conference on Smart Electronics and MEMS. 3673:351–358, 1999
 28. Agre JR, Clare LP, Pottie GJ, Romanov NP, 'Development Platform for Self-Organizing Wireless Sensor Networks', Proceedings of SPIE 3713:257–267, 1999
 29. Liu RC, Zhou L, Chen X, Mau ST, 'Wireless Sensors for Structural Monitoring', *Strong Motion Instrumentation for Civil Engineering Structures*, pp. 253–266, 2001
 30. Sirohi J, Chopra I, 'Fundamental Understanding of Piezoelectric Strain Sensors', *Journal of Intelligent Material Systems and Structures*, Vol. 11, April, pp. 246 – 257, 2001
 31. Rahimi M, Shah H, Sukhatme GS, Heideman J, Estrin D, 'Studying the Feasibility of Energy Harvesting in a Mobile Sensor Network' Proceedings of the 2003 IEEE International Conference on Robotics & Automation, Taipei. Taiwan, September 14-19, pp. 19-24, 2003
 32. Sodano HA, Inman DJ, Park G, 'A Review of Power Harvesting from Vibration Using Piezoelectric Materials', *The Shock and Vibration Digest*, Vol. 36, No. 3, May, pp. 197-205, 2004
 33. Sodano HA, Park G, Inman DJ, 'Estimation of Electric Charge Output for Piezoelectric Energy Harvesting', *Strain*, Vol. 40, pp. 49-58, 2004
 34. Roundy S, Wright PK, Rabaey J, 'A Study of Low Level Vibrations as a Power Source for Wireless Sensor Nodes', *Computer Communications*, Vol. 26, pp. 1131-1144, 2002
 35. Roundy S, 'On the Effectiveness of Vibration-based Energy Harvesting', *Journal of Intelligent Material Systems and Structures*, Vol. 16, pp. 809 – 823, 2006
 36. Warneke BA, Pister KSJ, 'Exploring the Limits of system Integration With Smart Dust', Proceedings of IMECE'02, New Orleans, Louisiana, 2002
 37. Issa MA, Islam MS, Chudnovsky A, 'Size Effects in Concrete Fracture: Part I, Experimental Setup and Observations', *Int. J. Fracture*. 102 1–24, 2000
 38. Otis B, Chee YH, Lu R, Pletcher NM, Rabaey JM, 'An Ultra-Low Power MEMS-Based Two-Channel Transceiver for Wireless Sensor Networks,' IEEE Symp. VLSI Circuits, June 2004

39. EmbedSense™ Wireless Sensor, Wireless Sensor and Data Acquisition System, MicroStrain®, 2007
40. Arms SW, Townsend CP, Churchill DL, Phan N, 'Energy Harvesting, Wireless, Strain Sensor for Damage Tracking of Helicopter Components,' 3rd European Workshop on Structural Health Monitoring, 2006
41. Elvin NG, Elvin AA, Spector M, 'A Self-Powered Mechanical Strain Energy Sensor', *Smart Materials and Structures*, No.10, pp 293-299, 2001
42. Elvin NG, Elvin AA and Choi DH, 'A Self-Powered Damage Detection Sensor', *The Journal of Strain Analysis for Engineering Design*, v.38,n2, pp115-125, 2003
43. Dorio C, Hasler P, Minch B, Mead CA, 'A Single-Transistor Silicon Synapse', *IEEE Trans. Electron Devices*, vol. 43 (11), Nov. 1996
44. Sodano HA Inman DJ, Park G, 'Comparison of Piezoelectric Energy Harvesting Devices for Recharging Batteries', *J Intel Mater Syst Str* 16 799-807, 2005
45. Nakano K, Elliott SJ, and Rustighi E, 'A Unified Approach to Optimal Conditions of Power Harvesting Using Electromagnetic and Piezoelectric Transducers', *Smart Mater. Struct.* 16 948-958, 2007
46. Cho YS, Pak YE, Han CS, Ha SK, 'Five-Port Equivalent Electric Circuit of Piezoelectric Bimorph Beam', *Sensors and Actuators* 84 140-148, 2000
47. Lesieutre GA, Davis CL, 'Can a Coupling Coefficient of a Piezoelectric Actuator be Higher Than Those of its Active Material?', *J. Intell. Mater. Syst. Struct.* 8 859-67, 1997
48. Ottman GK, Hofmann HF, Bhatt AC, Lesieutre GA, 'Adaptive Piezoelectric Energy Harvesting Circuit for Wireless Remote Power Supply', *IEEE Trans. Power Electron.* 17 669-76, 2002
49. Roundy SJ, Wright PK, 'A Piezoelectric Vibration Based Generator for Wireless Electronics', *Smart Mater Struct* 13 1131-1142, 2004
50. Ajitsaria J, Choe SY, Shen D, Kim DJ, 'Modeling and Analysis of a Bimorph Piezoelectric Cantilever Beam for Voltage Generation', *Smart Mater. Struct.* 16 447-454, 2007
51. Van Noortwijk JM, Klatter HE, 'The Use of Lifetime Distributions in Bridge Replacement Modeling', 1st Int. Conf. on Bridge Maintenance, Safety and Management, 2002

52. Roundy SJ, 'Energy Scavenging for Wireless Sensor Nodes with a Focus on Vibration to Electricity Conversion', PhD Thesis University of California, Berkeley, 2003
53. Starner, T, 'Human-Powered Wearable Computing', IBM Systems Journal, 35: 618–629, 1996
54. Shenck N, Paradiso J, 2001, 'Energy Scavenging with Shoe-Mounted Piezoelectrics', IEEE Micro, 21(3): 30–42, 2001
55. Mehra A, 'Development of a High Power Density Combustion System for a Silicon Micro Gas Turbine Engine', Ph.D. Thesis, Massachusetts Institute of Technology, 2000
56. Stan MR, Franzon PD, Goldstein SC, Lach JC, Ziegler M, 'Molecular Electronics: From Devices and Interconnect to Circuits and Architecture', Proc. IEEE 91 1940–57, 2003
57. Amirtharajah R, Chandrakasan AP, 'Self-powered Signal Processing Using Vibration-Based Power Generation', *IEEE J.Solid-State Circuits* 3 687–95, 1998
58. Amirtharajah R, Chandrakasan AP, 'A Micropower Programmable DSP Using Approximate Signal Processing Based on Distributed Arithmetic,' *IEEE Journal of Solid-State Circuits*, vol. 39, pp. 337–347, Feb 2004
59. PicoRadio: University of California, Berkeley Project.
60. X-bow: X-Bow Technologies Mica2Dot Wireless sensor Mote.
61. Micron:-Micron Technology NOR Flash Memory.
62. Texas Instrument: MSP430 microprocessor.
63. Cavendish:-Cavendish Kinetics Corp, MEMS memory.
64. LSI: - LSI Logic Corp—LSI403LC Digital Signal Processor.
65. Telos:- Moteiv Corporation.
66. Kao J, 'Sub-threshold Leakage Control Techniques for Low Power Digital Circuits', PhD Thesis Massachusetts Institute of Technology, 2001
67. El-Borgi S, Choura S, Ventura C, Baccouch M, Cherif F, 'Modal Identification and Model Updating of a Reinforced Concrete Bridge', *Int. J. Smart Struct. Syst.* 1 83–101, 2005

68. Watters DG, Jayaweera P, Bahr AJ, Huestis DL, Priyantha N, Meline R, Reis R, Parks D, 'Smart Pebble: Wireless Sensors for Structural Health Monitoring of Bridge Decks', *Proceedings of SPIE* 5057 20–8, 2003
69. Giaccio G, Zerbino R, 'Failure Mechanism of Concrete-Combined Effects of Coarse Aggregates and Strength Level', *Adv. Cement Based Mater.* 7 41–8, 1998
70. Brownjohn JWM, personal communication, Data measured for the rooftop of the 280 meter tall, 66 story, Republic Plaza building, Singapore, 2005
71. Celebi M, 'GPS in Dynamic Monitoring of Long-Period', structures Soil Dyn. Earthq. Eng. 20 477–83 COSMOS: Consortium of Organizations, 2000
72. Li QS, Fang JQ, Jeary AP, Wong CK, Liu DK, 'Evaluation of Wind Effects on a Supertall Building Based on Full-Scale Measurements', *Earthquake Eng. Struct. Dyn.* 29 1845–62, 2002
73. Lovse JW, Teskey WF, Lachapelle G, Cannon ME, 'Dynamic Deformation Monitoring of tall Structures Using GPS Technology', *J. Surveying Eng* 121 35–40, 1995
74. ISO-2631 Mechanical vibration and shock -- Evaluation of Human Exposure to Whole-Body Vibration -- Part 2: Vibration in Buildings (1 Hz to 80 Hz), International Organization for Standards
75. AISC Design guide 11, Floor Vibrations Due To Human Activity, American Institute of Steel Construction, 1997
76. Bachmann H, 'Vibration Problems in Structures', Birkhauser, Germany 1994
77. Polastre J, Szewczyk R, Sharp C, Culler D, 'The Mote Revolution: Low Power Wireless Sensor Network Devices', *Proc. Hot Chips* 16, 2004
78. Elvin NG, Lajnef N, and Elvin AA, 'Feasibility Of Structural Monitoring With Vibration Powered Sensors', *Smart Mater Struct* 15 977-986, 2006
79. Shibata T, Ohmi T, 'A functional MOS Transistor Featuring Gate-Level Weighted Sum and Threshold Operations', *IEEE Transactions on Electron Devices*, vol. 39 (6), pp.1444–1455, June 1992
80. Srinivasan V, Serrano GJ, Gray J, Hasler P, 'A Precision CMOS Amplifier Using Floating-Gate Transistors for Offset Cancellation', *IEEE Journal of Solid State Circuits*, vol. 42, no. 2, February 2007

81. Machado Gerson AS, Enz CC, Bucher M, 'Estimating Key Parameters in the EKV MOST Model for Analogue Design and Simulation', Proc. IEEE Int. Symp. Circuits Syst., pp. 1588-1591, Seattle, Washington 1995
82. Hasler P, 'Foundations of Learning in Analog VLSI', Ph.D. Thesis, California Institute of Technology, Pasadena, California, 1997
83. Lajnef N, Chakrabartty S, Elvin N, Elvin A, 'Piezo-Powered Floating Gate Injector for Self-Powered Fatigue Monitoring in Biomechanical Implants', IEEE Symposium on Circuits and Systems (ISCAS'2007), New Orleans, 2007
84. Rincon-Mora GA, 'Voltage References: From Diodes to Precision High-Order Bandgap Circuits', New York: John Wiley, 2001
85. Sansen WM, Op't Eynde F, Steyaert M, 'A CMOS Temperature-Compensated Current Reference', *IEEE Journal of Solid-State Circuits*, vol. 23, no. 3, pp. 821-824, June 1988
86. Gray PR, Hurst PJ, Lewis SH, Meyer RG, 'Analysis and Design of Analog Integrated Circuits', 4th Edition: John Wiley, 2001
87. Widlar RJ, 'Design Techniques for Monolithic Operational Amplifiers', *IEEE Journal of Solid-State Circuits*, vol. SC-4, pp. 184-191, 1969
88. Vittoz E, Fellrath J, 'CMOS Analog Integrated Circuits Based on Weak Inversion Operation', *IEEE Journal of Solid-State Circuits*, vol. 12, pp. 224-231, 1977
89. the EECS Department of the University of California at Berkeley, The SPICE page, <http://bwrc.eecs.berkeley.edu/Classes/icbook/SPICE/>, Accessed July 2008